A Viable Isolated Tissue System: A Tool for Detailed MR Measurements and Controlled Perturbations in Physiologically Stable Tissue.

Simon Richardson

A dissertation submitted in partial fulfilment
of the requirements for the degree of
Doctor of Philosophy

Medical and Biomedical Imaging

Department of Medical Physics and Bioengineering
University College London.

I, Simon Richardson confirm that the work presented in this thesis is my own. Where information has been derived from other sources, I confirm that this has been indicated in the thesis. This work is based on research which has been conducted by me during the time period of October 2010 to December 2013 at University College London, U.K.

Simon Richardson, December 2013.

Abstract

The research presented here revolves around the development, testing and applications of a tool for maintaining a sample of viable isolated tissue (VIT) in a stable state. A stable viable tissue sample has the potential to provide a test bed which is more relevant to *in vivo* tissue than the more commonly used artificial phantoms or fixed tissue samples.

The VIT maintenance chamber was designed to maintain a section of rat optic nerve. The objective was to keep the tissue as close to *in vivo* conditions as possible, while removing all of the confounding problems of in vivo imaging. The chamber was designed for a high field MRI scanner and to enable extended periods of experimentation. A series of validation experiments was conducted to demonstrate the performance of the chamber and the stability of optic nerves maintained within it.

Fixed samples have been used extensively in diffusion MRI (dMRI) studies. However, fixation causes significant structural changes in tissue. The chamber was used to evaluate fixed white matter as a surrogate for viable white matter during development and validation of dMRI methods. Diffusion tensors and multi-compartment white matter signal models were fitted to the data. The data demonstrated that fixed tissue, while maintaining the broad water environment of viable tissue, differs significantly in water diffusion parameters.

The chamber was further developed to enable in MRI electrophysiological stimulation and recording from the rat optic nerve. The objective was to investigate the existence of a dMRI measurable structural change in the tissue upon electrical activation. A functional diffusion MRI (dfMRI) signal could be more specific to *in vivo* functional activation than the current gold-standard fMRI method. VIT removes the confounders of blood flow allowing direct investigation of the dfMRI effect. Preliminary data suggests that a purely structural dfMRI effect, though marginal, was measured.

Acknowledgements

I would like to thank my supervisors; Dr Bernard Siow, Professor Mark Lythgoe and Professor Daniel Alexander for making this project happen. It has been interesting at every stage, I couldn’t ask for more from a project.

I started this PhD as a climate biologist and ecologist, a lot has changed and I have learnt more than I ever anticipated. I could not have done this without the following people.

Unlimited advice, guidance, help and mentoring were given to me during the course of this work by Dr Bernard Siow and Dr Andrew Batchelor. Payment even with fine whiskey seems hardly enough.

Dr Torben Schneider and Dr Eleftheria Panagiotaki from the micro-structure imaging group (MIG) gave invaluable help, advice and troubleshooting support, and words in the pub which can’t be overvalued.

Professor John Garthwaite kindly allowed me the use of his lab and equipment. Both he and Professor Giti Garthwaite provided valuable guiding thoughts and support here and there during my time at UCL.

All of the students and staff at the centre for advanced biomedical imaging (CABI) gave advice or support at one stage or another of this work. I would particularly like to thank Ben Duffy for being the principal representation of the ‘red queen effect’ during the course of this PhD. Dr Jack Wells, Dr Adam Badar and Isabel Christie also deserve special mentions for keeping the comedy and enthusiasm alive at difficult moments.

“Invention, it must be humbly admitted, does not consist in creating out of void but out of chaos”

Mary Shelley, ‘Frankenstein or the Modern Prometheus’ (1818).

Table of Contents

List of Tables

List of Figures

1.0 Introduction

The human brain is a highly complex biological machine; its functional mechanisms and microscopic structure are still not fully understood despite centuries of scientific investigation. As with any complex machine, understanding the functional behaviour requires a detailed understanding of the structure. Classically histology has been used to investigate the structure of the brain and its cellular components. While histological methods have provided a great depth of information on the ex vivo brain, understanding how this information may apply to the working *in vivo* brain is a non-trivial problem.

Magnetic resonance imaging (MRI) has emerged as a powerful tool for medical imaging and is the preferred imaging modality for *in vivo* soft tissue imaging e.g. [1]. Magnetic resonance (MR) can be sensitized to the self-diffusion of water [2–4]. Water populations in biological tissue are not free to diffuse: a highly complex arrangement of membranes and organelles restrict and hinder free water diffusion [5]. Diffusion weighted magnetic resonance imaging (dMRI) methods, which can be made sensitive to these patterns of water diffusion, can thus potentially be used to infer microstructural parameters of the *in vivo* tissue under examination e.g. [6] & [7].

dMRI is an advancing field: a range of methods has been developed focussed on elucidating the microstructural features of biological tissue non-invasively. dMRI measurements from neuronal tissue *in vivo* are complicated by movement, surrounding tissue structure, vascular and susceptibility effects, and restricted scan duration [8]. These factors limit the data acquisition and in turn, the accuracy and stability of quantitative *in vivo* dMRI data.

In order to validate and develop methods which aim to infer microstructural parameters with dMRI, a stable and reliable test bed is desirable. A model system for testing and development of such methods should ideally represent as many features of an *in vivo* system as possible while mitigating as far as possible the complications described above.

1.1 Problem Statement

The core problem that motivated this work was that stable samples or phantoms that accurately represent *in vivo* tissue are not easily available for development and testing of new MRI techniques.

This problem is of particular relevance to dMRI development where long scan durations and sample stability are required. As mentioned, scanning animals directly is of limited value to early development of dMRI methods as scan durations are limited and physiological movement is an ever present confounder. Because of this, artificial phantoms and fixed tissue are commonly used but the relevance of these to an *in vivo* system is uncertain. Isolated tissue maintained in a viable state is the logical solution given these constraints; however a proven, stable and validated system to maintain isolated tissue at physiologically relevant temperatures has not previously been demonstrated. A viable isolated tissue (VIT) system is of limited value unless it can be shown to maintain tissue in a stable manner for the duration of experiments. A reliable VIT system could be applied to answer a range of current open questions within the dMRI community and would be of wider use for other MRI methods and investigation and assessment of tissue perturbations and drug delivery efficacy.

1.2 Project Aims

The aims of this project were then as follows:

1. Design and construct a device which can maintain a sample of viable isolated white matter in a stable state for extended MRI experiments within a small diameter coil in a preclinical scanner.
2. Validate the stability of tissue maintained within this device at physiologically relevant temperatures.
3. Use the device to examine dMRI detectable differences between fixed and viable white matter in identical conditions at physiological temperatures.
4. Apply a detailed taxonomy of microstructural models to both viable and fixed samples to determine the most suitable model for the tissues.

5. Adapt the device to enable stimulation and recording of action potentials within the MRI scanner.
6. Investigate the potential of diffusion MRI to directly detect neuronal activation in isolated nervous tissue.

1.3 Summary of Contributions

The key contributions of this work are as follows:

- An MRI compatible viable isolated tissue maintenance chamber design which can be produced using digital manufacturing methods. The chamber enables imaging of isolated viable tissue at physiological temperatures in small bore high field MRI scanners – project aim 1.
- Detailed testing and validation of the chamber's ability to maintain isolated white matter in a structurally, functionally and dMRI stable state for up to ten hours at physiological temperatures– project aim 2. This work was published as a journal paper [9] and has been displayed at international scientific meetings (see Sections 7.7.1 & 7.7.3).
- As mentioned above, dMRI is of particular use in probing white matter within the living body. It is uncertain how fixed white matter, which is commonly used as the mainstay in development projects, differs from viable in terms of its dMRI parameters. The chamber was used to investigate the effects of fixation in white matter: dMRI properties and differences of VIT and fixed tissues at physiological temperatures were demonstrated. This work included the application of an extensive set of white matter dMRI signal models which provide parameters relevant to the underlying tissue microstructure – project aims 3 and 4. This work was published as a journal paper [10] and has been displayed at international scientific meetings (see Sections 7.7.1 & 7.7.3).
- A further development of the chamber, to produce a version which enables the stimulation and recording of action potentials – project aim 5.
- There is great interest in the existence of dMRI detectable neuronal activation; this is a controversial topic with influential proponents on both

sides of the argument. Viable isolated tissue is the ideal system for investigating this exciting question as the confounding factors of blood-flow and movement can potentially be removed. The chamber capable of stimulation and recording of action potentials in the MRI scanner enabled a preliminary experimental investigation of the potential to detect neuronal activation using dMRI – project aim 6.

1.4 Thesis Structure

This report describes the development, validation and applications of a system to maintain viable isolated tissue (VIT) in a stable state for extended MRI experiments. The system was used to conduct a detailed dMRI comparison of VIT and fixed white matter and to investigate the potential for detecting neuronal activation in white matter using dMRI.

Section 2.0 contains background information related to the methods and theory used in later sections. Section 2.0 comprises a description of nervous tissue and an introduction to MRI, the basics of dMRI and modelling of the dMRI signal, a description of nervous tissue structure and how it may affect the patterns of water diffusion, a brief review of dMRI validation methods and a discussion of functional dMRI and additive layer manufacturing.

Section 3.0 describes the development, production and initial testing of a viable isolated tissue chamber.

Section 4.0 covers the validation of the chamber and testing of its capacity to maintain isolated optic nerves in a structurally, functionally and dMRI stable state for up to ten hours at physiologically relevant temperatures.

Section 5.0 details the application of the stable chamber to investigate differences between viable and fixed white matter at physiological temperatures.

Section 6.0 describes the testing of the dMRI detectability of structural changes in the optic nerve and the development of an adapted chamber which enables neuronal stimulation and recording in the MRI scanner. Preliminary application of this device to investigating dMRI detection of neuronal activation is also described.

Section 7.0 summarises conclusions for each section and discusses future directions for this work. Section 7.0 also includes an itemised list of work conducted during this thesis, a list of publications, a list of abbreviations used in this document and an appendix section for extra data. Finally a bibliography covering references from all sections is included.

2.0 Background

This section covers the background relevant to the contents of this work. A brief description of mammalian nervous tissue is given followed by sections covering MRI and diffusion MRI. Tying the previous sections together, water diffusion in nervous tissue is then covered. Next, methods for modelling the diffusion MRI signal in biological tissues are described. Following this is a discussion of the various validation methods used for diffusion MRI methods. The process behind electrophysiological recording in nervous tissue is then described followed by a discussion of MRI and neural activation and functional diffusion MRI methods. Finally additive layer manufacturing which was used extensively in this work is described.

2.1 Nervous Tissue

This section draws on several standard texts: [11–13]

The mammalian nervous system is a biological machine which receives processes and responds to, a huge volume of information delivered by the sensory organs. While the individual components of a brain can be examined and measured, it is the complex arrangement and interplay of millions of cellular units which leads to emergent features such as the mind. This thesis is focused on the structural components themselves and the continuing effort to examine them in situ and *in vivo*.

Mammalian nervous tissue is a complex and non-uniform structure. Broadly, the central nervous system can be separated into grey and white matter. White matter consists mainly of glial cells and myelinated axons while grey matter consists of neuronal cell bodies, glial cells and neuropil (dendrites and unmyelinated axonal processes). Both tissues are interwoven with capillary networks which are denser in grey matter than white. Grey and white matters are so named because of their relative appearance in gross anatomy; white matter appears pinkish white in fresh brain sections due to its high lipid content (myelin sheaths) and its capillary network. Grey matter is actually grey-brown and its colour is mainly due to its blood vessels and neuronal cell bodies (Figure 2.1.1b). Grey and white matter boundaries are distinguishable on standard MR images (e.g. Figure 2.1.1a).

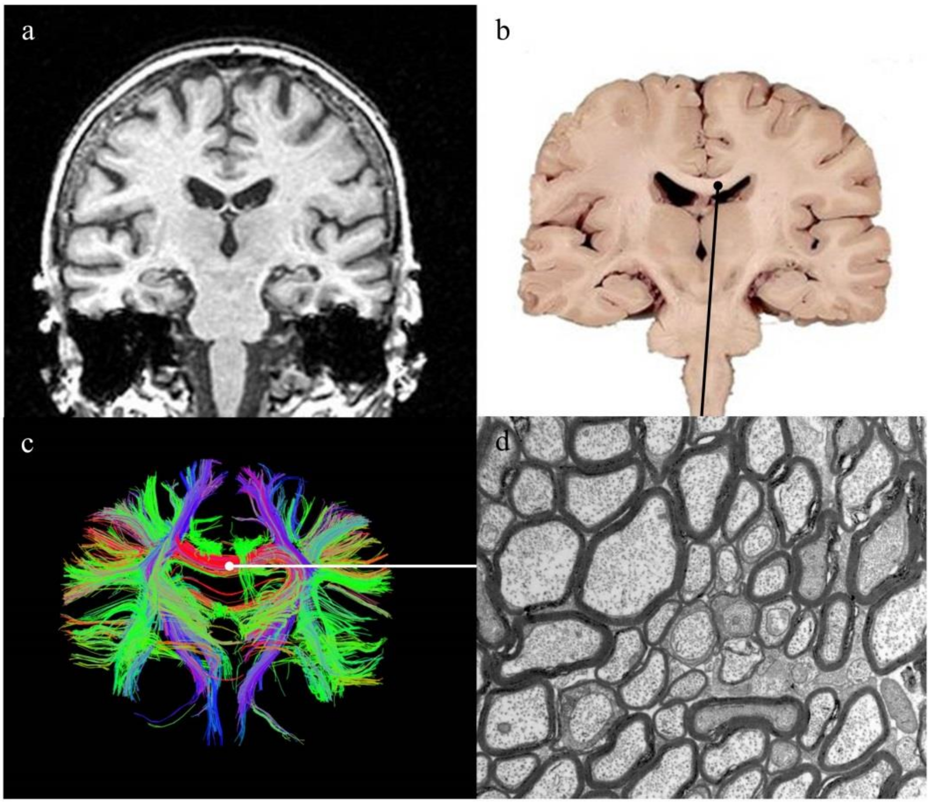

Figure 2.1.1: The Brain, a Range of Images.

Showing (a): relaxation time, T_1 weighted MRI image of the human brain, (b): a gross slice at a similar position, (c): tractography from diffusion tensor MRI and (d) an electron micrograph showing the microscopic detail of a cross section of axons within a white matter tract. Black and white lines indicate the corpus callosum white matter tract which appears similar to (d) under electron microscopy. Image sources: (a&c); data from Human Connectome Project (HCP) database (https://ida.loni.ucla.edu). (b); image from Utah medical library (http://library.med.utah.edu). (c); image from [14]. (d); image from [9].

White matter is the focus of this thesis (see Figure 2.1.2); it consists of tightly packed bundles of essentially cylindrical axonal processes, each surrounded by a myelin sheath. Glial cells pack between the axons and fill almost all the remaining space. Small capillary vessels weave through this matrix providing oxygen, nutrients and removing the by-products of cellular metabolism.

The myelin sheath of each axon consists of multiple layers of lipids wrapped in a spiral fashion around the axon. Myelinated cells conduct by salutatory conduction; the action potential hops down the nerve to each successive node of

Ranvier (gaps in the myelin sheath) and is thus faster than the continuous wave impulses in un-myelinated fibres.

The glial cell population in a normal white matter tract consists of oligodendrocytes, astrocytes and microglia.

Oligodendrocytes are the most common glial cell in white matter whose primary function is to extrude and maintain the myelin sheath which surrounds each axonal process. A single oligodendrocyte extends processes to multiple axons forming a section of the myelin sheath at each intersection; in the rat optic nerve a single oligodendrocyte may extend processes to 40 separate axons [15]. On the same axon adjacent myelin segments belong to different oligodendrocytes.

Astrocytes in white matter extend 50-80 processes which weave around axons and other glial cells and intersect with axons at the nodes of Ranvier. Astrocytes have been thought to primarily perform a supportive role, maintaining homeostasis of the surrounding tissue. Astrocytes cannot generate electrical action potentials. However, work over the past decade suggests that the astrocyte network plays a role in the regulation and stimulation of the neurons with which they interact via chemical signalling [16]. The astrocyte network could prove to be just as important to the processing of information and the function of the brain as neurons themselves [17].

Microglia are the resident macrophages of white matter. Smaller than astrocytes and oligodendrocytes, microglia do not extend processes but instead move rapidly to sites of damage and stress [18]. Microglial cells scavenge the white matter for plaques, damaged neurons and infectious agents and provide the immune privileged central nervous system with a ‘one-stop-shop’ for immune response.

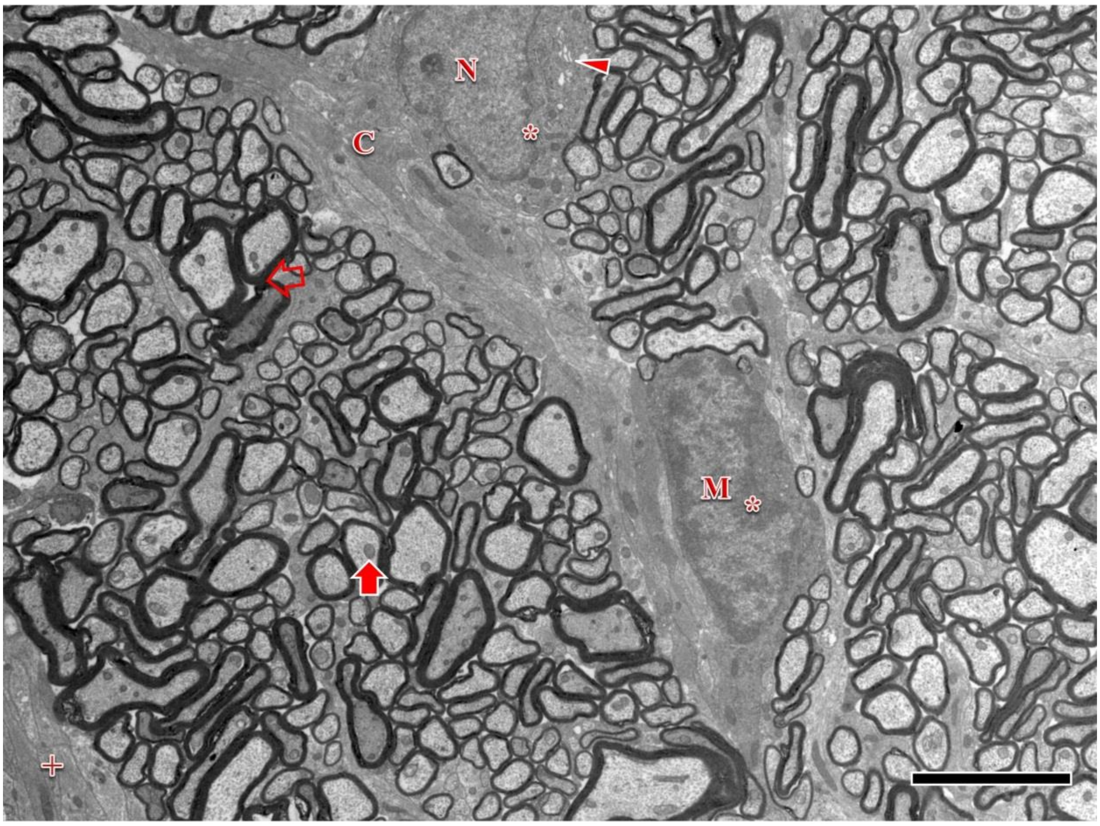

Figure 2.1.2: Electron micrograph from a Healthy Rat Optic Nerve.

An electron micrograph taken from a healthy rat optic nerve. (N): the nucleus of an oligodendrocyte, (C): cytoplasm of the same oligodendrocyte, (M): a typical microglial cell at rest, (+): an astrocyte process and (*): heterochromatin, clearly more dense in the microglia. The arrow head highlights a Golgi apparatus of the oligodendrocyte, the open arrow indicates compact myelin layers surrounding an axon while the solid arrow shows a mitochondrion within an axons cytoplasm. The Scale bar represents 5 µm.

2.2 Magnetic Resonance Imaging

MRI is a powerful tool for medical imaging and its continuing development by pre-clinical and clinical groups pushes the boundaries of current knowledge. MRI uses non-ionising radiation to extract information from the tissue under examination. This is in contrast to ionising radiation imaging methods such as x-ray computed tomography (CT) and positron emission tomography (PET). MRI is an excellent tool for soft tissue imaging and therefore a powerful tool for diagnosing and monitoring disease progression in the brain, heart, liver and other organs of the human body.

2.2.1 A Brief History of the Development of MRI

A brief history of the development of modern MRI and notable discoveries along the way is of interest and is set out below.

The unit strength of a magnetic field is named after Nikola Tesla (1856–1943), the Serbian born discoverer of the rotating magnetic field [19]. 1 Tesla (T) = 1 Newton/Ampere-metre and the Earth's magnetic field has a strength of 0.5×10^{-4} T, which is equal to 0.5 Gauss (1 Gauss = 1.0×10^{-4} Tesla).

Sir Joseph Larmor (1857-1942) developed the Larmor equation showing that the angular frequency ω of precession of the nuclear spins in a magnetic field is directly proportional to the product of the strength of the main magnetic field B_0 and the gyromagnetic ratio γ,

$$\omega = \gamma B_0. \qquad [2.2.1]$$

Isidor Rabi (1898-1988), first observed the quantum phenomenon of nuclear magnetic resonance (NMR) in experimenting with molecular beam methods to measure the magnetic moments of nuclei. Rabi demonstrated that atomic nuclei absorb electromagnetic energy at the Larmor frequency when exposed to strong magnetic fields. The first NMR curve, of Lithium 7 was published by Rabi in 1939 [20].

Felix Bloch (1905–1983) and Edward Purcell (1912–1997), working independently, found that when certain nuclei were placed in a magnetic field they absorbed energy from radio frequency electromagnetic waves, and re-emitted this energy when the nuclei 'relaxed' to their original state. They measured the signals from bulk processing nuclei in liquids and solids (water and paraffin) [21,22]. This work was the birth NMR spectroscopy which soon became a crucial method for analysing the composition of chemical compounds.

NMR spectroscopy became a widely used technique for the non-destructive investigation of various materials including biological samples. In 1971 Raymond Damadian demonstrated a difference in the spin–lattice relaxation time T_1 and the spin-spin relaxation time T_2 (see section 2.2.2 below) in healthy and cancerous tissues [23]. Damadian thought he had discovered the ultimate cancer diagnosis technology and filed a patent covering this discovery in 1972. However, the patent did not include any information on how to use the method in the human body.

Until this point, all the NMR experiments had acquired signals in one dimension and had no way of describing from where within a sample the signal originated. In 1973 Paul Lauterbur (1929 – 2007) and Sir Peter Mansfield, again working independently, demonstrated methods to use magnetic field gradients in NMR experiments to acquire spatial information from the sample [24,25]. These methods used a back projection method, similar to that used in computer assisted tomography (CT) x-ray methods, to reconstruct the image. The development of MRI was thus linked to the development of CT methods and in fact x-ray CT was first demonstrated in 1973 (the same year as Lauterbur and Mansfield's 2D NMR experiments) by Sir Godfrey Hounsfield (1919 – 2004) [26,27].

Inspired by a talk given by Lauterbur in 1974, Richard Ernst realised that, instead of the back projection methods of Lauterbur and Mansfield, switched magnetic gradients could be applied to spatially encode the signal using frequency and phase. The Fourier transform could then be used to reconstruct 2D images from the signal [28]. This method is more efficient and has become the mainstay of modern MRI.

Work on applying MRI to humans (still called NMR imaging at this point) progressed through the early 1970's. The first *in vivo* scan of human anatomy, a cross section through a finger (that of Andrew Maudsley working with Mansfield), was produced in 1977 [29]. The image took about 23 minutes to acquire and used a line scan technique. In 1980 the group lead by William Edelstein produced an image of the human body using Ernst's technique, managing to acquire a single image in around 5 minutes [30]. Echo planar imaging (EPI) was proposed by the Mansfield group in 1977 [31] and early results in humans using this method were published in 1978 [32]. EPI allowed the acquisition of a whole image using a single echo (hence the name), and reduced imaging times from minutes to seconds allowing 'real time' MRI methods.

Through the 1970's and 1980's various technical developments by several groups improved upon the hardware, acquisition methods and processing required to take MRI from an experimental technology to the major medical imaging technique it is today. The first commercial MRI scanner in Europe (made by Picker Ltd, Cleveland, U.S.A.) was installed in 1983 for the Department of Diagnostic Radiology at the University of Manchester's Medical School.

2.2.2 Basic MRI Physics

This section contains a description of the key concepts of magnetic resonance imaging. Firstly, the property of atomic spin in individual nuclei is described, then the behaviour of the bulk of nuclei and their spins and the effect of an external magnetic field on them. This is followed by a description of magnetic resonance absorption of energy and how the emission of this energy is recorded. The generation of echoes, spatial encoding of the signal and generation of an MR image are then described. Finally the factors affecting the spatial resolution of MRI are described. Information in this section, unless stated, is informed by standard texts, [33] & [14].

2.2.2.1 Nuclear Spin and the Magnetic Moment

Any nucleus with an uneven atomic number has a non-zero angular momentum or atomic spin. Protons (H^1) are one such nucleus and are of interest in MRI as they are very common in the body in water and other molecules. Nuclear spin is a phenomenon governed by quantum physics but it can be described using the vector model of classical physics: The proton can be represented as a spinning charge which generates its own small magnetic field and therefore has a magnetic moment. The magnetic moment μ is directly proportional to the proton's angular momentum l and its gyromagnetic ratio so that,

$$\mu = \gamma l. \qquad [2.2.2]$$

If the proton is exposed to an external magnetic field, it will experience a turning force or torque, due to its spin and magnetic moment, which causes it to attempt to align with the applied magnetic field. The individual proton cannot align completely with the magnetic field as it is constrained by the laws of quantum mechanics; it therefore still experiences a torque which causes it to precess around the principal direction of the applied field. The frequency of this precession is given by the Larmor equation [2.2.1] and is proportional to the strength of the magnetic field.

In quantum mechanics the proton's spin is said to be quantised - that is, in one of two states: either aligned with the B_0 direction (parallel) or aligned against B_0 (anti-parallel), see Figure 2.2.1b. The anti-parallel orientation is a slightly higher energy state and because of this, the number of protons aligned in the parallel state is slightly higher than those in the anti-parallel state. When ensembles of protons experience an external magnetic field they therefore produce a non-zero net magnetic moment. The magnetic moments of all the protons precessing around the applied magnetic field produce a net magnetization vector $\underline{M}$ which, unlike the individual magnetic moment of the protons, is aligned exactly with the principal direction of B_0 (Figure 2.2.1a). The net magnetization vector quantity can be represented by a longitudinal component M_z and a second component perpendicular to the first, the transverse magnetization M_{xy}. It is convenient to describe a group of protons with the same precession frequency as a spin, this phrase will be used from here on.

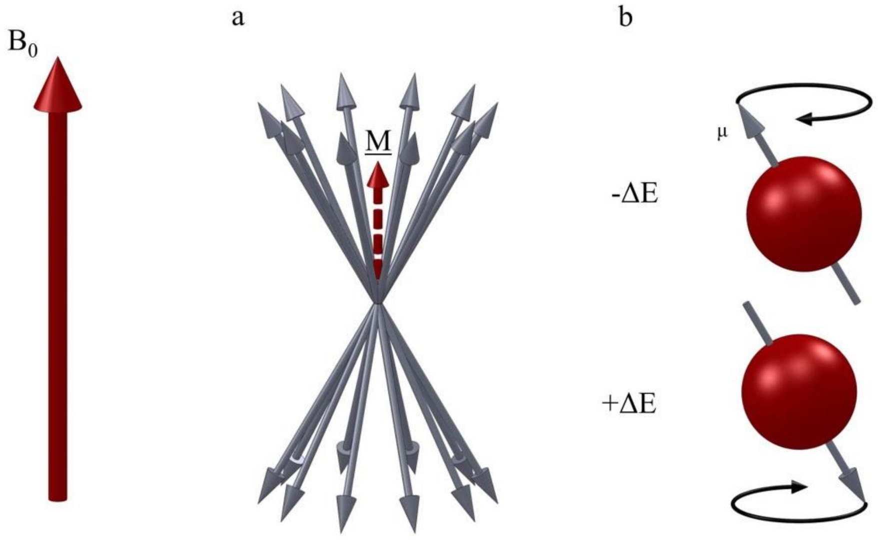

Figure 2.2.1: Magnetic Moment Vectors and Energy Levels.

Showing (a), the magnetic moment vectors of groups of protons (spins) and the net magnetization vector $\underline{M}$ and in (b), the energy states of protons with magnetic moment vectors orientated parallel and anti-parallel to the main magnetic field B_0. Black paths show the precession of the magnetic moment vectors around B_0.

2.2.2.2 Excitation and Relaxation

Because of the difference in energy between the parallel and antiparallel states, spins may absorb or emit energy and transition between states. In MRI, an oscillating magnetic field B_1 orientated at 90º to the B_0 field is used to deliver energy; this is called excitation. The condition for this resonant absorption to occur is that the oscillations must be at the correct frequency, the Larmor frequency. The B_1 field is generated by passing a radio frequency (RF) current through a transmitter coil; this is an RF pulse. Application of an RF pulse changes the distribution of the parallel and anti-parallel states and brings the spins' magnetic moments into phase coherence. This induces a rotation of $\underline{M}$ into the transverse plane. The amount of rotation can be selected by the strength and duration of the RF pulse; e.g., a 90º RF pulse rotates $\underline{M}$ by 90º. The precession of $\underline{M}$ produces an oscillating magnetic field which can induce a small current in an RF receiver coil (tuned to detect M_{xy}) and this is the signal recorded in MRI.

Excited spins must relax: After RF excitation, 'spin-spin' interactions cause the spins to de-phase with one another and the transverse magnetization decays away. The time constant for this relaxation is T_2. Inhomogeneity in the main magnetic field, susceptibility effects and proton diffusion lead to faster de-phasing than that attributable to pure T_2. The combination of T_2 and these extra effects are described with the time constant T_2*. The decaying signal is known as free induction decay (FID). As the spins de-phase due to spin-spin interactions, M_z is also recovering with the time constant T_1. T_1 relaxation is due to spins losing the energy they acquired during the RF pulse to the surrounding lattice and returning to the equilibrium distribution of parallel and anti-parallel states. The rate of T_1 relaxation is (generally) greatly reduced compared to T_2. In biological tissue T_2 is much less than T_1. T_1 and T_2 differ in different materials and tissues in the body; regions of differing T_2 are one source of contrast in MR images.

2.2.2.3 Echo Generation

In MRI the FID created by the 90º RF pulse is not immediately measured. Instead, two main methods are used to generate an echo, which can be recorded; either a gradient echo or a spin echo. The time between the first RF pulse and the peak of the generated echo is the echo time (TE). Figure 2.2.2 shows a pulse sequence diagram of a gradient echo sequence. Figure 2.2.3 shows a pulse sequence diagram of a spin echo sequence. The pulse sequences are repeated after a certain time, known as the repetition time (TR).

In the gradient echo method (Figure 2.2.2): after application of a 90º RF pulse a small spatially varying magnetic field (a magnetic gradient) is created in addition to the main B_0 field. This gradient causes rapid de-phasing as spins in different positions experience different magnetic field strengths and precess faster or slower, just as the rate of precession of a gyroscope is dependent on the strength of the gravitational field imposed upon it. After this de-phasing lobe, an equal and opposite gradient lobe is switched on and this rephrasing lobe brings spins back into phase with one another and a gradient echo is generated in the receiver coil.

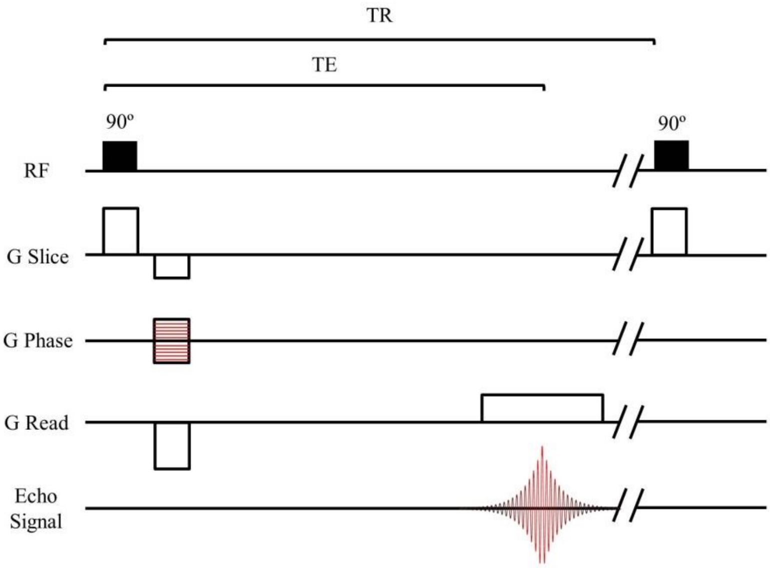

Figure 2.2.2: Gradient Echo Pulse Sequence Diagram.

Showing the TE and TR, RF pulses, slice, phase and read magnetic field gradients and the generated echo signal. The next repetition of the sequence to collect data from the next phase encoding step is shown starting after TR.

The spin echo method (Figure 2.2.3) uses an extra 180º RF pulse at time TE/2, to generate the echo. Immediately after the 90º RF pulse, M is in the transverse plane, the spins then de-phase according to T_2*. At time TE/2 the 180º RF pulse is applied, which rotates the magnetisation through 180º, meaning that direction of phase evolution of the spins is reversed relative to one another (they continue to precess in the same direction). The spins therefore return to phase coherence at TE and a signal can be detected in the receiver coil.

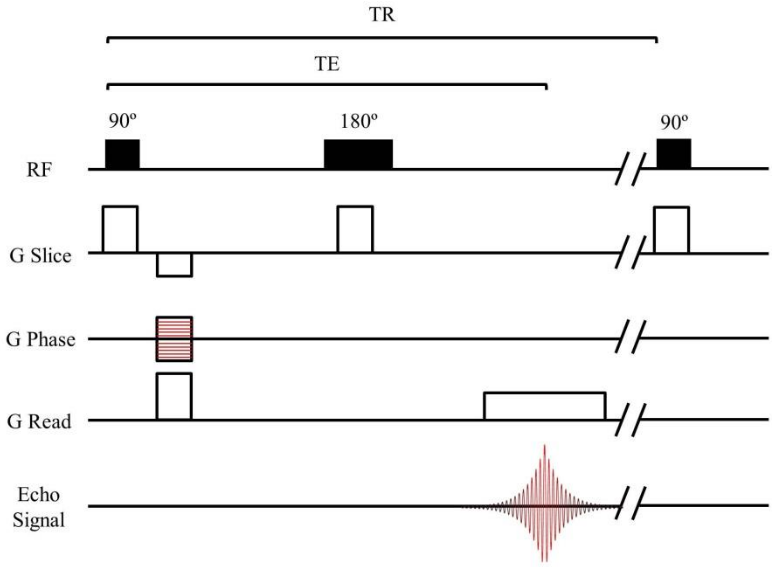

Figure 2.2.3: Spin Echo Pulse Sequence Diagram.

Showing the echo time TE, repetition time TR, RF pulses, slice, phase and read magnetic field gradients and the generated echo signal. The next repetition of the sequence to collect data from the next phase encoding step is shown starting after TR.

The 'runners on a track' analogy can be useful in understanding the advantages of the spin echo: each runner is a spin experiencing a different track condition (local magnetic field). Once the race starts (90º RF pulse), they begin to move (de-phase) at a speed dictated by the condition of the track. At the 180 pulse they turn around and run back, but those on smoother 'tracks' have moved further so have a greater distance to travel back. Those on rough 'tracks' have not moved as far, so have less distance to travel back.. The result is that the runners all return to the start line at the same time (in phase) to break the finish line ribbon (produce an echo). As a result of the spin echo method, local magnetic field inhomogeneity de-phasing effects are effectively cancelled out. In the gradient echo sequence the spins are forced to speed up or slow down their precession by application of the extra gradients, so that when the gradient is reversed the effects of underlying B_0

inhomogeneity are not cancelled out. The spin echo is therefore sensitive to T_2 contrast while the gradient echo is sensitive to T_2*. Figure 2.2.4 show a vector representation of the generation of a spin echo.

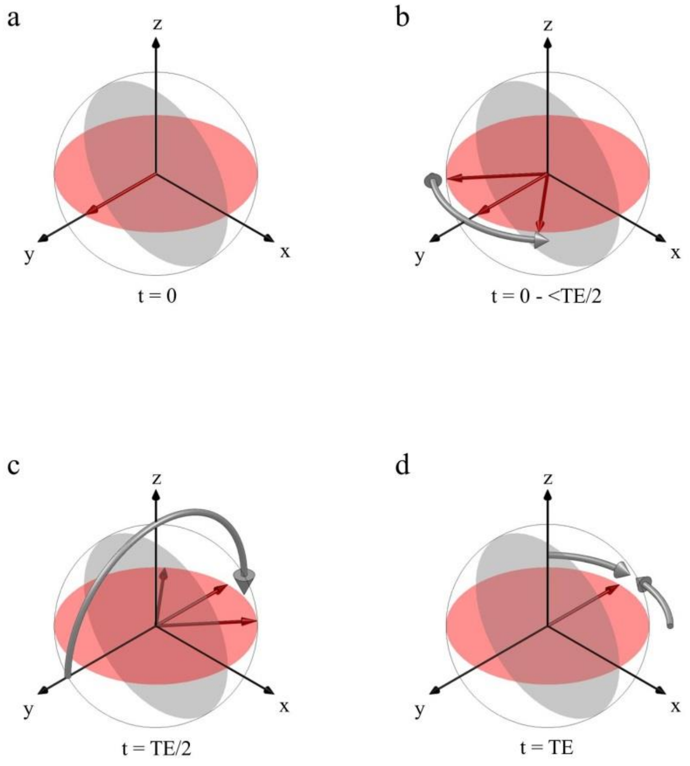

Figure 2.2.4: Vector Representation of a Spin Echo Sequence

Showing a vector representation of the process of spin echo generation in the rotating reference frame. The red arrow is a vector representing the net magnetisation $\underline{M}$ of the spins in the sample. (a) Immediately after the application of the 90º RF pulse (t = 0), $\underline{M}$ has been tipped into the transverse plane and is precessing about B_0. (b) After the RF pulse the spins de-phase due to relaxation; in the rotating frame the spins vectors advance or retard around the z axis. (c) The 180º RF pulse applied at t = TE/2 flips the vectors over so that the direction of phase evolution of the spins is reversed relative to one another. (d) At t = TE, the spins are fully in phase and the maximum spin echo is generated.

2.2.2.4 Spatial Encoding

Adaptations to the spin echo sequence allow acquisition of MR signal from specific regions of the sample and the spatial encoding of the signal; this is how an MR image is generated. This basic description of spatial encoding uses the spin echo sequence shown in Figure 2.2.3 as an example but similar methods are used with other MRI pulse sequences to generate images.

Spatial localisation of the signal is achieved by the timely application of magnetic gradients along various directions (G_x, G_y & G_z) which correspond to the scanner bore orientations (x and y across the bore and z parallel to it). Firstly, a slice selective gradient is applied in the z direction G_z) across the sample at the same time as the excitation RF pulse. This slice selective gradient causes spins at different points along the bore to precess at different frequencies (see Larmor equation 2.2.1). Setting the 90º RF transmit pulse to a narrow band of frequencies allows the selective excitation of a 'slice' of protons in the sample. The slice position can then be moved by varying the gradient and the RF frequency. In practice the offset of the RF pulse is varied while the gradient is maintained. During recording of the echo, a gradient perpendicular to the slice direction G_x is applied. This method results in a range of frequencies being recorded which corresponds to spatial locations across the bore; this is frequency encoding. To obtain spatial information in the y direction, an extra gradient in the y-direction G_y is briefly applied just before the echo is generated. This gradient slows or speeds up the precession frequency of spins corresponding to their position along the gradient. As described above, this causes the spins' phases to change relative to each other. When the gradient is switched off the spins return to their original precession frequency but with an acquired phase difference. This phase evolution means that the recorded signal is the combination of signals from a certain spatial frequency. Repeating the pulse sequence with different phase encoding gradients allows the full range of spatial frequencies to be acquired; this is phase encoding. The time between repeats of the sequence TR allows the magnetisation to recover to its starting state. Any applied gradients cause an alteration in phase. In practise the other encoding gradients (G_x and G_z) have de-phasing lobes which compensate for the phase changes they induce.

Several methods are available to acquire spatial information at an increased rate. In one method used in this work, the spin echo sequence is effectively speeded up to acquire MR information in a shorter time by using a fast spin echo (fSE) pulse sequence. In an fSE sequence, a train of 180° RF pulses is applied after the first 180° pulse to refocus the signal repeatedly. In between each 180° pulse the phase encoding gradient is stepped. In this way multiple spatial frequencies in the phase encoding direction can be acquired from a single 90° RF excitation, in a single TR.

The amplitude of the received signal decays away with T_2, so this process cannot be continued indefinitely.

Each successive phase encoding step acquires data from a single spatial frequency. Once all of the spatial frequencies have been acquired a 2D Fourier transform converts this information from the time domain into the frequency domain. This data is the MR image, since the relationship between frequency and position is defined by the Larmor equation (see [34]).

2.2.2.5 Spatial Resolution

MRI spatial resolution is limited by signal to noise ratio (SNR). SNR increases in proportion to voxel volume (larger voxels give a higher SNR but lower image resolution), the number of measurements and decreasing receiver bandwidth. This relationship is summarised as,

$$SNR = k(voxel\ volume).\sqrt{\frac{number\ of\ measurements}{bandwidth}}, \quad [2.2.3]$$

the constant k, includes hardware dependent factors, field strength dependent factors, pulse sequence type and parameters and tissue dependent parameters (e.g. T_1 & T_2).

With sensitive RF coils appropriate imaging gradients and high enough SNR, MRI can identify structures on the micrometre scale [7]. However the functional unit of the brain is the neuron and structural MRI *in vivo* cannot directly image structures on these scales (0.1-10μm diameter in the mammalian nervous tissue) [35]. Another technique is required.

2.3 Diffusion Weighted Magnetic Resonance Imaging

By providing information on the mobility of particles within a sample, diffusion weighted MRI can provide information at the sub voxel level, beyond the reach of traditional MRI.

Diffusion MRI relies on a basic property of water: molecular diffusion. Molecules in a pool are randomly displaced by collisions with other molecules [36]. The distance travelled by a freely diffusing molecule is proportional to time and the diffusion coefficient D. Root mean square displacement (x_{rms}) is then described by

$$x_{rms} = \sqrt{2nDt}, \qquad [2.3.1]$$

where n is the number of dimensions and t is the diffusion time. D is dependent upon the diffusing molecules in question, the viscosity of the solvent they encounter and the temperature of the system. A probabilistic framework can be used to describe the motion of an ensemble of molecules undergoing diffusion. A displacement distribution then quantifies the fraction of molecules that will be displaced a certain distance in a set time, or the likelihood that a single molecule will move a certain distance in that time.

Diffusion weighting can be applied to a variety MR imaging pulse sequences including gradient echo and spin echo sequences. In diffusion weighted spin echo sequences an extra gradient pair is applied in a set direction. This extra gradient pair encodes for diffusion. The first extra gradient causes the phase of the spins to diverge and they become out of phase with each other. After the 180° RF pulse the diffusion encoding gradient is repeated, this causes the spins to re-phase and the signal produced is once again at a maximum. If however between the application of the two diffusion encoding gradients the spins change position in the direction of the diffusion encoding gradient, their phases will not evolve enough to return them to phase coherence and the signal received will be less than maximum.

Diffusion can cause this displacement of spins between the two diffusion encoding gradients. The displacement caused by water diffusion is therefore detectable as a reduction in received signal. This method was first described by Stejskal and Tanner for use with NMR [4]. Signal loss due to gradient application and water diffusion obeys the equation,

$$\frac{S}{S_0} = e^{-\gamma^2 \mathrm{G}^2 \delta^2 \left(\Delta - \frac{\delta}{3}\right) D}, \qquad [2.3.2]$$

where S_0 is the signal intensity without diffusion weighting, S is the signal with weighting, D is the diffusion coefficient, γ is the gyromagnetic ratio, G is the gradient strength, δ is the length of the diffusion sensitizing gradient pulses and Δ is their separation time. The factors describing the amount of diffusion weighting are summarised as b, called the b-value;

$$b = -\gamma^2 G^2 \delta^2 \left(\Delta - \frac{\delta}{3}\right) \qquad [2.3.3]$$

and so the signal loss due to diffusion weighting can be written,

$$\frac{S}{S_0} = e^{-bD}. \quad [2.3.4]$$

Figure 2.3.1 shows a schematic example of a standard pulsed gradient spin echo (PGSE) sequence used to impart diffusion weighting [4] to an MR signal. The PGSE sequence is a standard spin echo sequence (see section 2.2.2.3) with two extra trapezoidal diffusion gradients applied before and after the 180 degree RF pulse. Altering the separation time of the pulses (Δ) and their duration (δ) sensitizes the sequence to differing water diffusion ranges. The amplitude of the diffusion weighting gradient pulses can be increased to compensate for shorter δ (imparting the same diffusion weighting) which allows for shorter echo times.

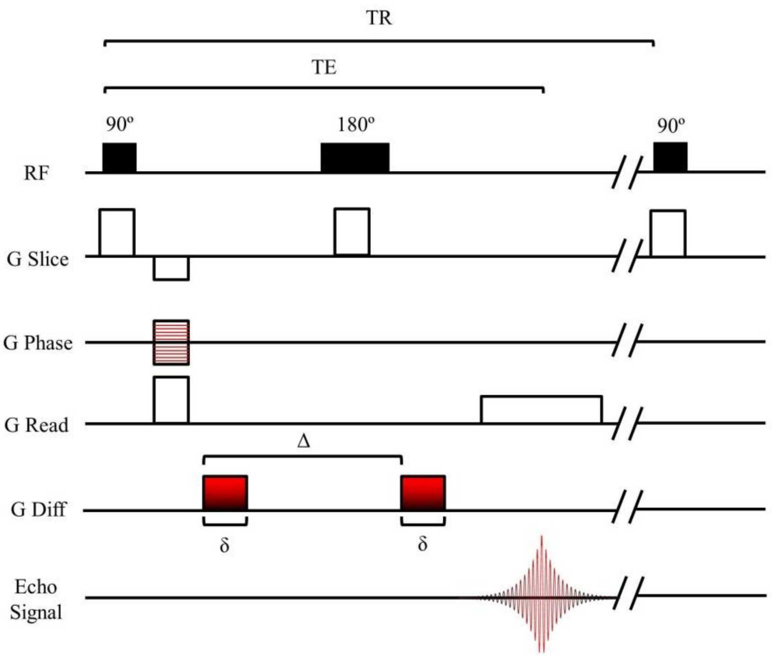

Figure 2.3.1: Pulsed Gradient Spin Echo Sequence Diagram.

A pulsed gradient spin echo (PGSE) sequence, showing the radio frequency (RF) pulses and gradients (G Slice, G Phase and G Read) required for a standard spin echo MR acquisition with the addition of two diffusion encoding gradient pulses (G Diff) of duration δ and separation Δ. The acquired echo signal is also shown along with the next iteration of the sequence which starts after TR.

Equation [2.3.5] demonstrates that the D in any one direction can be estimated by acquiring two differently weighted signals, one with the diffusion gradients set to zero (S_0) and one to non-zero (S). Both gradient sets are orientated in the required direction, so by rearranging equation [2.3.4], we obtain

$$D = -ln\left(\frac{S_0}{S}\right).b^{-1}. \quad [2.3.5]$$

Water diffusion occurs in various modes: in ‘free diffusion’ e.g. in pure water, root mean square displacement is described by equation [2.3.1] and the displacement distribution is Gaussian. Similarly in ‘hindered diffusion’ e.g. a matrix which causes the path of the water molecules to be tortuous, x_{rms} is reduced but still linearly related to t. The displacement distribution is still Gaussian. In this situation diffusivity will appear to be lower and an apparent diffusion coefficient (ADC) is measured, rather than D itself. A third mode of water diffusion is ‘restricted diffusion’. A barrier which restricts movement on the measured time scale will cause the calculated displacement to plateau. In restricted diffusion, the relationship between x_{rms} and t will not be linear. Restricted diffusion will thus be detectable as a non-linear signal decay and the displacement distribution will be non-Gaussian [37].

2.4 Nervous Tissue Structure and Diffusion

The structure of nervous tissue has significant and measurable effects on diffusion which can be measured with dMRI.

As previously mentioned, mammalian nervous tissue can be broadly divided into grey and white matter. A major difference between these two tissue types, of great interest to the diffusion MRI community, is the marked directionality of white matter in contrast to the relatively isotropic nature of grey matter. In general, water diffusion in white matter is anisotropic; the probability of displacement parallel to the fibre is greater than the probability of perpendicular displacement. Consider a glass cylinder immersed in a container filled with water: molecules can freely diffuse inside and outside the cylinder unless they come into contact with its wall. Water molecules which happen to move along the direction of the cylinder will, on average, travel further than those moving toward the walls. The directionality of this example system reflects that of white matter fibre bundles within the brain which can be considered to be collections of semi-permeable cylinders with a clear directionality (see Figure 2.4.1). If this pattern of water diffusion in 3D were known, the directionality and dimensions of the cylinder could be inferred.

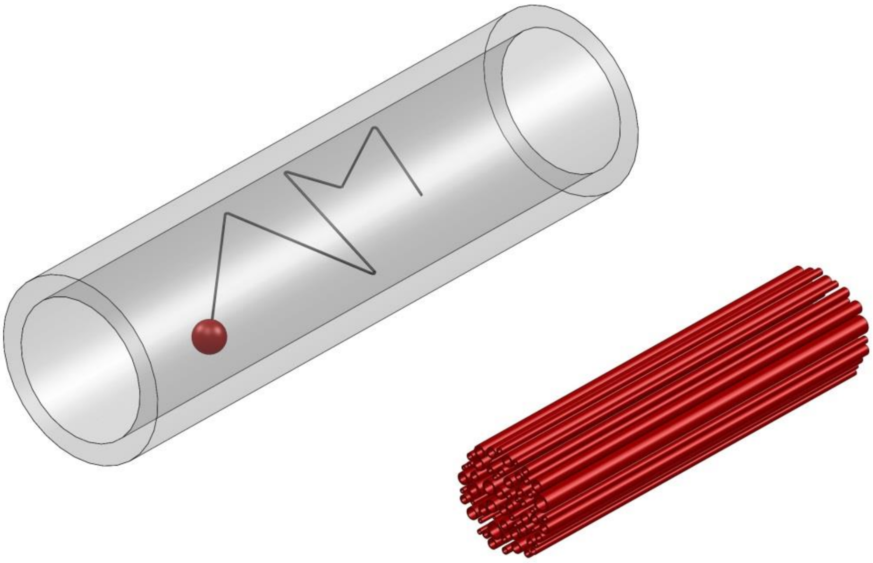

Figure 2.4.1: Diffusion in a Cylinder.

Showing the semipermeable multi-cylinder representation of a nerve bundle in red and the path of a diffusing water molecule in a cylinder.

When considering extracting information on the microstructure of white matter with dMRI methods, a more detailed picture of water diffusion within the tissue is desirable. There are various potential barriers and hindrances within white matter which contribute to the diffusion pattern of the bulk water population to a lesser or greater extent. Some of these features are illustrated in Figure 2.4.2.

The myelin sheath of white matter neurons represents a significant barrier to water diffusion perpendicular to the axons and its breakdown in disease can be detected with dMRI e.g. [38]. The myelin sheath is essentially a greatly extended and modified plasma membrane which extrudes from oligodendrocyte glial cells in white matter and wraps around the axons in a spiralling manner [39]. The myelin layers around nerve axons are a major contributor to the directionality of water diffusion measured in white matter bundles. The cytoplasm of the axons is packed with the machinery of cellular function and maintenance, all of which can potentially be a hindrance to water diffusion. For example in the axons of the rat optic nerve, mitochondria, cytoskeletal elements (microfilaments, neurofilaments and microtubules) and endosomes are found in abundance [40] and all have the potential to hider the free movement of water molecules. Glial cells are more typically isotropic cells; a single lipid bi-layer surrounds each cell and its processes. The cytoplasm within glial cells contains a different (less linear) arrangement of cytoskeletal components, the nucleus and Golgi apparatus and a range of other organelles. The cytosol itself, which surrounds the cytoplasmic organelles and structures, consists of a complex chemical cocktail dissolved in water. The composition of cytosol varies; around 70% is water with the remaining portion consisting of ions, small molecules and large water soluble molecules such as proteins [41]. The viscosity of the cytosol is similar to that of pure water but due to the presence of macromolecules diffusivity is around four fold less than in pure water [42].

In between the glial cells and axons in a white matter bundle is the extra cellular space (ECS) tissue. The ECS is occupied by interstitial fluid (ISF) (which in the brain is in contact with the cerebrospinal fluid (CSF)) and the extra cellular matrix (ECM). The ECM anchors cells to itself and to one another and serves as a supportive network providing much of the structural strength of nerve bundles. The ECM is composed of a variety of proteins and polysaccharides that are secreted locally and assembled into an organized meshwork which is closely associated with the surface of the cell that produced them [43]. The ECS thus has a significant effect on water diffusion leading to tortuosity of movement and hindrances [44].

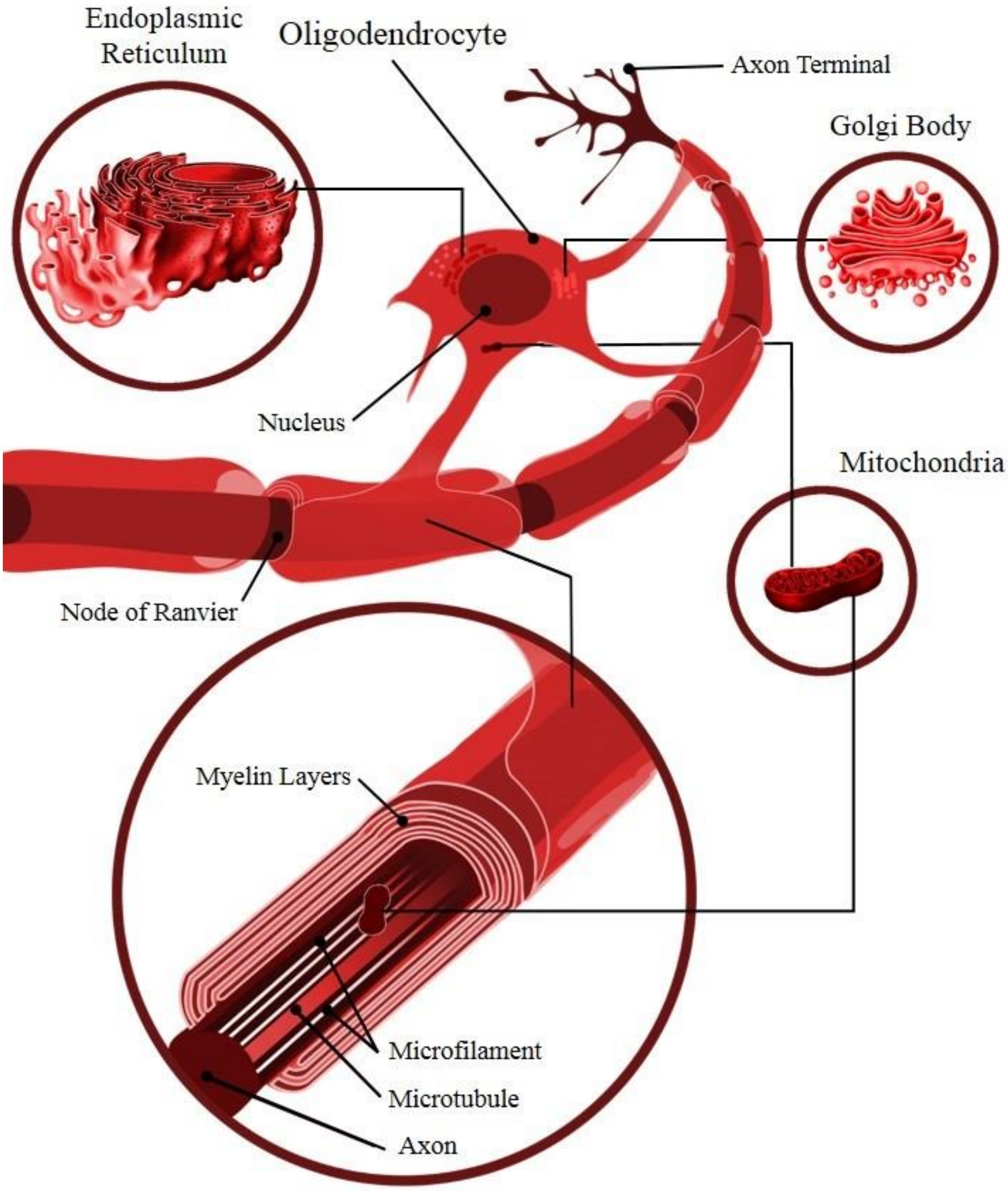

Figure 2.4.2: The Axon and Oligdendrocyte: Major Structures.

Showing an oligodendrocyte and its extruded myelin sheath wrapped around a nearby axon in a white matter bundle such as the rat optic nerve. Some major features of these cells that restrict and hinder water molecules within and around them are illustrated. The axon terminal which in the rat optic nerve is at the first synapse in the lateral geniculate body, is also shown for illustrative purposes. Adapted from Wikipedia Commons: ‘Complete neuron cell diagram’.

In the mid 1990’s various studies reported a non-monoexponential decay of the water diffusion weighted signal in neural tissue e.g. [45] & [46]. These discoveries lead to the conclusion that several water populations which diffused at different rates combined to produce this pattern. Two diffusing components were described as fast and slow diffusing. The slow diffusing component has been found to exhibit restricted water diffusion while the fast consists of free or hindered water diffusion [47]. The magnitude of the slow diffusing component greatly increases when measured perpendicular to fibres [47,48] and in white matter compared with grey matter [47]. This suggests that a large proportion of the slow component comes from intra axonal water and that the remaining structures (ECS and glial cells) are responsible for the fast component. However the components are not exclusive to intra and extra axonal water; both fast and slow water diffusion have been demonstrated in the cytoplasm of the frog oocyte [49]. It is clear that a complex microenvironment of water population exists in mammalian nervous tissue and dMRI methods are only just beginning to disentangle these effects to produce more detailed descriptions of the water diffusion patterns.

2.5 Modelling the Diffusion MRI Signal in Biological Tissue

The simplest method to measure water diffusion in biological tissue is to measure the ADC (see equation [2.3.5]). Quantitative ADC maps have been extensively tested for various clinical roles e.g. [50]. Measured ADC in the brain is strongly dependent on the applied gradient direction; this is due to anisotropic obstructions to water diffusion (e.g. cylinder-like axons). To overcome this dependence and characterise the displacement distribution in three dimensions, a modelling system can be used, one of the simplest and most commonly used is the diffusion tensor [6].

2.5.1 The Diffusion Tensor

The diffusion tensor (DT) is a 3 by 3 matrix of diffusivities [2.5.1] which characterises the displacement distribution in three dimensions. At least six measures taken along non-collinear directions are needed to estimate the tensor. The diffusion tensor model assumes that the displacement distribution is a trivariate Gaussian with a zero mean

$$DT = \begin{bmatrix} D_{xx} & D_{xy} & D_{xz} \\ D_{yx} & D_{yy} & D_{yz} \\ D_{zz} & D_{zy} & D_{zz} \end{bmatrix} \qquad [2.5.1]$$

Where the diagonal elements of the matrix e.g. D_{xx} correspond to orthogonal (i.e. x, y and z in the laboratory reference frame) diffusivities, the off diagonal elements describe the correlation between the diagonal elements. The diffusion tensor can be thought of an ellipsoid, with its outer surface representing the distance a particle will diffuse from the origin with equal probability. In an isotropic sample the tensor will be represented by a sphere and in a strongly anisotropic sample by a prolate ellipsoid. The principal axes of the ellipsoid are defined by eigenvectors (e_1, e_2 & e_3) with eigenvalues (λ_1, λ_2 & λ_3) which correspond to the three directional diffusivities along the principal axes of the tensor ($d_{\parallel}$, $d_{\perp 1}$ & $d_{\perp 2}$). The eigenvalues are sorted according to their magnitudes i.e. $\lambda_1 \geq \lambda_2 \geq \lambda_3$. Figure 2.5.1 shows a graphical illustration of the diffusion tensor ellipsoid measured from a range or sub voxel structures.

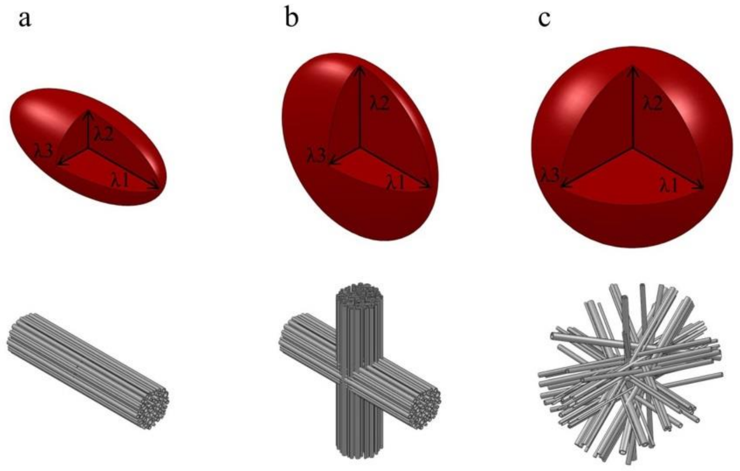

Figure 2.5.1: Diffusion Tensor Shapes Defined by Microstructure.

Showing a range of possible diffusion tensor ellipsoid shapes (top) produced from differing sub voxel microstructure arrangements (bottom). Three microstructure arrangements are shown (a): linear fibres, (b): crossing fibres and (c) isotropic fibres.

From the tensor, the sample's fractional anisotropy (FA) as the degree of directionality of the tensor, its mean diffusivity (MD) (average of the $d_{\parallel}$, $d_{\perp 1}$ & $d_{\perp 2}$) and radial diffusivity (RD) (average of $d_{\perp 1}$ & $d_{\perp 2}$) can be calculated (equations [2.5.2], [2.5.3] and [2.5.4] respectively). When using diffusion tensors, $d_{\parallel}$ from the tensor is often referred to as the axial diffusivity (AD). Both FA, and MD from the tensor are commonly used biomarkers in white matter and grey matter studies e.g. [51]. FA is used a biomarker defining the degree of directionality of the sample, this could change if white matter bundles become less anisotropic e.g. in damaged regions. MD can indicate the average degree of diffusion in the sample. MD therefore increases if there is less hindrance to water diffusion and so measures of MD can indicate structural integrity of tissue in a voxel. Diffusion tensor imaging (DTI) can be used to measure the directionality of tissue within voxels. It is the basis for basic MRI tractography methods which can provide information on the interconnectivity of brain regions. The FA is defined as

$$FA = \sqrt{\frac{3}{2}}\,\frac{\sqrt{(\lambda_1 - \lambda)^2 + (\lambda_2 - \lambda)^2 + (\lambda_3 - \lambda)^2}}{\sqrt{\lambda_1^2 + \lambda_2^2 + \lambda_3^2}}. \quad [2.5.2]$$

The MD is defined as

$$MD = \frac{\lambda_1 + \lambda_2 + \lambda_3}{3}. \quad [2.5.3]$$

The RD is defined as

$$RD = \frac{(\lambda_2 + \lambda_3)}{2}. \quad [2.5.4]$$

2.5.2 Compartment Modelling

The diffusion tensor is a single compartment model which is fit to the bulk water diffusion profile and so cannot extract information about water pools within the tissue which behave differently. For example, water in the intra axonal space and water in glial cells and in the extra cellular space. The DT assumption of Gaussian water diffusion is also a major limitation [52], as restriction in biological tissue means that the signal rapidly departs from the model (see Figure 2.5.1c). In an attempt to overcome the limitations of DTI and extract more detailed microstructural information from within the voxel, multi-compartment models of the water diffusion signal have been developed, see [53] for overview.

Compartmentalisation of the signal allows modelling of Gaussian and non-Gaussian displacement distribution patterns simultaneously. For example, if the signal is modelled to extract the contribution from hindered and restricted compartments, more specific information can be obtained on both. Models vary in complexity from simple two compartment models without exchange, e.g. a ball representing extra axonal space (hindered) and a stick for the axons (restricted) [54], to three compartment models which include exchange between compartments e.g. [55] & [56]. All these models aim to fit the dMRI signal and extract relevant microstructural parameters. Correlating the modelled compartments to ground truth microstructural information is a non-trivial challenge [57]. It is worth noting that compartment models are predictions of biological tissue water population behaviour from data measured over a voxel much larger than the structural unit of the tissue. Thus compartment modelling of the dMRI signal can only aim to capture and interrogate broad patterns in the dMRI signal; these methods are not directly observing and measuring the tissue microstructure as in electron microscopy for example.

2.5.2.1 Multi Compartment Models in this Work

In section 5.0 of this work, a range of multi-compartment tissue models were applied to rich multi-b-value dMRI datasets. For a full mathematical description and details on the origins of these compartment models see [53]. Each model is a combination of compartments. There are three types of compartments: [1] intra-axonal (restricted models of water diffusion), [2] extra axonal, (isotropic and anisotropic non-restricted water diffusion models) and [3] isotropic restriction. Briefly, intra axonal compartments options are: [a] “Sticks”, which have direction and diffusivity as parameters and describe water diffusion in a zero radius cylinder and [b] “Cylinders”, which factor in non-zero cylinder radii and so have an extra parameter for the ‘axon’ radius. Extra axonal compartments options are: [a] “Balls”, an isotropic compartment with only diffusivity d as a parameter, [b] “Zeppelins”, which are anisotropic but cylindrically symmetric with parallel and perpendicular diffusivities ($d_{\parallel}$ & $d_{\perp}$) along with direction parameters and [c] the full “Tensor” with an extra perpendicular diffusivity parameter where $d_{\perp 1} \neq d_{\perp 2}$. Finally, isotropic restriction compartment options are: [a] “Astrosticks”, which are isotropically distributed zero radius cylinders with a common origin and only diffusivity as a parameter, [b] “Astrocylinders”, a non-zero radius version of “Astrosticks” with the required extra parameter, [c] “Sphere”, which describes water diffusion within a sphere of non-zero radius with impermeable boundaries and has diffusivity and radius as parameters and [d] "dot", which is a special case of sphere with zero radius and so has no fitted parameters (the signal remains un-attenuated).

2.6 Validation of Diffusion MRI methods

In vivo dMRI assessment of neuronal tissue is confounded by movement, surrounding tissue structure, vascular and susceptibility effects, and restricted scan duration [8]. These factors limit the data acquisition and in turn, the accuracy and stability of quantitative dMRI data. Attempts to mitigate these issues using i) artificial phantoms, ii) chemically-fixed tissue and iii) VIT have been made in pre-clinical studies:

Artificial phantoms representing some features of white matter have been produced using rayon textile filament fibres [58], collections of (water-filled) plastic capillaries [59] and glass micro capillaries [60] & [61]. However, artificial phantoms are limited as they do not replicate the structural complexity of biological tissue nor its biochemical activity.

Chemically fixed tissue does provide this structural complexity and overcomes several issues of imaging *in vivo* [62], but water populations differ in distribution and behaviour [63] & [64] and fixed tissue also lacks *in vivo* electrophysiological and biochemical activity.

VIT potentially fills the gap between *in vivo* and fixed tissue. Movement and other artefacts associated with *in vivo* imaging are removed while maintaining the structural complexity and chemical properties of living tissue [65]. In addition VIT can maintain electrophysiological activity, and thus allows measurement of physiological responses following tissue perturbation [66]. Importantly VIT allows extended acquisitions periods which are not feasible *in vivo*, and therefore allows in-depth exploration of tissue characteristics. VIT models have been scanned over long sustained durations [7,67–69]. Tissue structure is often explored to provide comparative control data for MR microstructure imaging techniques e.g. [55] & [70]. However, tissue integrity and viability at physiological temperature over time have not been explored in an MRI compatible VIT system. For isolated tissue to be useful and reliable as an MR model system, the tissue must remain stable over the time periods required for MR acquisitions.

Differences in dMRI behaviour between VIT and *in vivo* and fixed tissue have previously been reported. As discussed by Shepherd et al [63], the bulk of previous works are confounded by two major issues. Firstly post mortem interval which has a marked effect on fixed tissue dMRI [71], is variable in previous work (immediate fixation being ideal). Secondly, studies of fixative effects have compared *in vivo* samples (at 37°C) with ex vivo fixed tissues at room temperature [72,73]. This comparison is questionable as water diffusion is highly sensitive to temperature differences [74]. Recently VIT and aldehyde fixed brain slice preparations have been compared at room temperature [63]. While this comparison is valuable, water diffusion in biological tissue does not vary linearly as in free water [75] so behaviour may differ at higher temperatures. Comparing samples at physiological temperature is more representative of *in vivo* conditions.

2.7 Electrophysiology in Nervous Tissue

Electrophysiology (EP) is the recording of electrical potentials from biological tissues. Electrophysiology is a wide field; signals can be recorded from the intracellular space or surface of individual cells or externally from individual or groups of cells. In this work, extra cellular electrophysiology of neurons in the rat optic nerve is used.

2.7.1 The Neuron from an Electrical Perspective

Information in this section is taken from [35] & [76].

The axon of a neuron can be roughly thought of as a conductive cylinder surrounded by an insulating membrane. The membrane has an appreciable electrical capacitance. The membrane of the neuron is a lipid bi-layer; lipid bi-layers have a relatively high electrical resistance in isolation. The membrane in the neuron however is not purely a lipid bi-layer and not a perfect insulator: it has some leak conductance, which gives it a membrane resistance. The membrane is not electrically passive: it contains ion pumps that maintain a difference between the concentrations of potassium and sodium ions inside and outside the cell. This concentration difference causes the resting potential of the cell’s cytoplasm to be negative relative to the extracellular medium (about -70 mV [77]). There are other voltage-gated ion channels in the membrane that enable the cell to produce rapid de-polarizations of the membrane potential which can propagate along the axon (action potentials).

In its resting state the concentration of potassium ions inside the cell is greater than the external concentration while the reverse is true for sodium. During a nerve impulse the local ion conductivity of the membrane increases about 100 fold and sodium moves down its concentration gradient into the cell, reversing the charge distribution across the membrane so that the inside becomes temporarily positive. Potassium ions are then able to flow along their concentration gradient out of the cell, lowering the membrane potential again. The resting ion balance is then restored by active sodium-potassium exchange pumps (see [76] for details). Figure 2.7.1 shows a diagram of the changes in membrane potential driven by these ion exchanges.

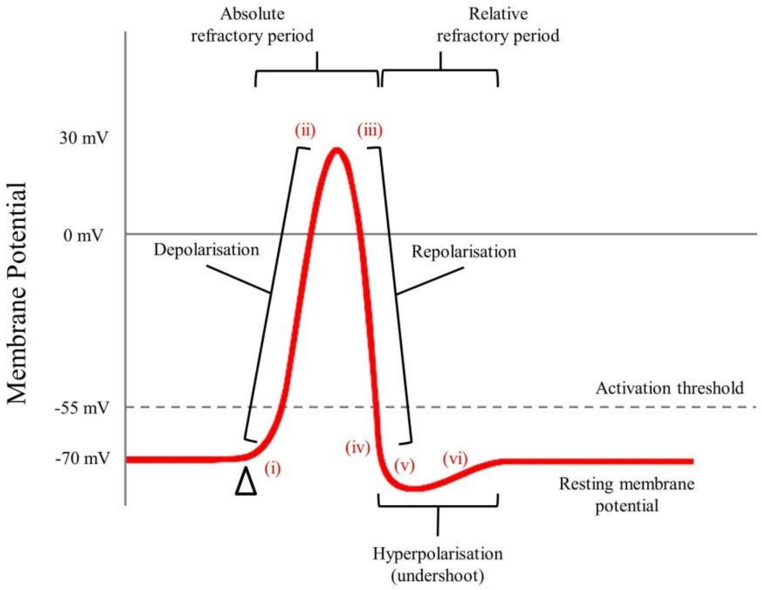

Figure 2.7.1: The Local Membrane Potential During an Action Potential.

Showing the membrane potential before, and after an applied stimulus above the threshold voltage (-55 mV) to induce an action potential in a neuron. The major flows of charge carrying ions are shown in red (i – vi): (i) Na^+ channels open: Na^+ in, (ii) Na^+ channels inactive (blocked), (iii) K^+ channels open: K^+ out, (iv) Na^+ channels close, (v) K^+ channels close, (vi) K^+ in and Na^+ out driven by active Na^+/K^+ pump.

Crucially, this process causes local changes in charge across the membrane. Electric current therefore flows between the active portion of the membrane and the resting portion just ahead. This current reduces the membrane potential in the resting portion and this activates the voltage gated sodium channels in this new section of membrane. Figure 2.7.2a shows a diagrammatic representation of this process in an un-myelinated axon. Myelin is an insulator and so in myelinated axons, the capacitance of the membrane is reduced and its resistance increased between the nodes of Ranvier (portions of the membrane exposed to the extracellular space). In myelinated axons the current therefore flows between these excitable portions of the membrane in a process known as salutatory conduction (Figure 2.7.2b). Myelination thus greatly increases the velocity of impulse conduction along the nerve.

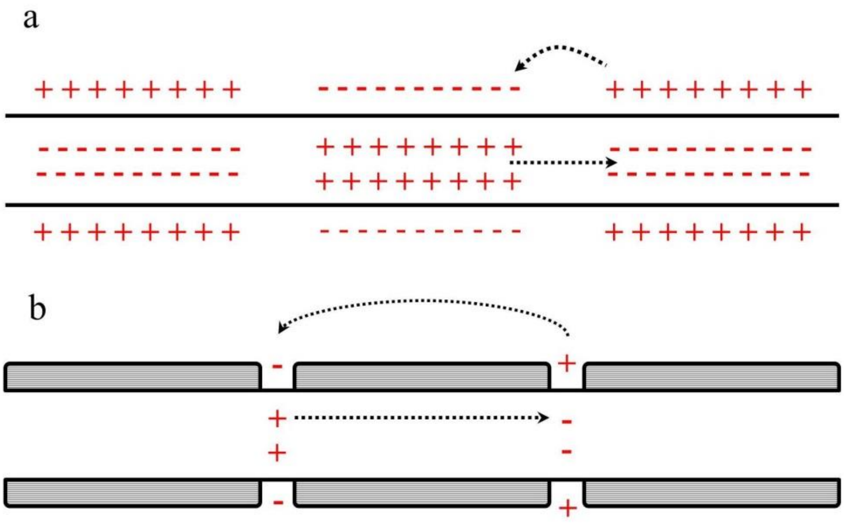

Figure 2.7.2: Local Circuit Generation During an Action Potential.

Showing a schematic diagram illustrating the local circuit theory in both an un-myelinated (a) and a myelinated neuron (b). Dotted lines represent the flow of current.

2.7.2 Recording the Action Potential

An electrode placed in proximity to a nerve cell which is undergoing electrical activity can be used to pick up and record local changes in current. An electrode can also be used to deliver current to the cell in order to induce an action potential. Extracellular action potential recording of single nerve cells can be achieved with a variety of methods [78]. In this work action potentials are recorded from a large number of simultaneously firing axons within the rat optic nerve. The recorded voltage change is known as a compound action potential (CAP) and is usually on the order of 3 - 6 mV. The CAP is the combination of signals from multiple axons which produce action potentials of differing velocities and amplitudes dependant on their diameter [79], the temperature of the system and whether or not the fibre is myelinated. Because the CAP is formed by the combination of many fibres its shape is different from that of a single action potential as shown in Figure 2.7.1. Figure 4.2.1c shows a characteristic CAP recorded from an isolated rat optic nerve using the grease gap method.

Two different CAP recording and stimulation methods are used in this work; grease gap and suction electrode electrophysiology. Details on the setup of these methods are covered in sections 4.1.5 and 6.1.2.1 respectively.

2.8 MRI and Neural Activation

Detecting neuronal activation using magnetic resonance imaging is an attractive prospect. An accurate and reproducible functional MRI (fMRI) method enables investigation function of the brain in its native state.

The most successful fMRI method to date uses blood oxygen level dependent (BOLD) contrast in the brain [80]. BOLD fMRI relies on T_2*-weighted imaging of the brain before during and after stimulation, which often takes the form of a motor exercise or a visual stimulus e.g. [81,82]. BOLD fMRI is sensitive to the haemodynamic response within the tissue as oxygenated haemoglobin has a different magnetic character from that of deoxygenated [80]. When nervous tissue is activated, a haemodynamic response is induced in the local area (see [83] for review), and the changes in levels of oxygenated haemoglobin caused by this response are then detectable as regional changes in T_2*. BOLD fMRI has been primarily used for detecting activation in grey matter regions within the brain e.g. [84]. BOLD fMRI in white matter has also been demonstrated [85–87] but is a newer and more controversial area [88].

2.8.1 Limitations of BOLD fMRI Experiments

As BOLD fMRI relies on detecting surrogate signal changes caused by oxygenation changes in the blood, it is not a direct marker of neuronal activation. The relationship between brain activity and these blood based signal changes has been speculated but has only recently been examined in detail using combined MRI and intra-cortical electrophysiological recordings [82]. Combined MRI and electrophysiology methods have demonstrated a firm link between regional neuronal activation and the corresponding regional T_2* changes. While there is a relationship between blood flow changes and regional activation, the temporal resolution of BOLD MRI is limited as paramagnetic haemoglobin must enter or leave the voxel for changes to be detected and the spatial localisation of activation detection with BOLD is governed by the regional blood vessel architecture (see [89]). BOLD fMRI is also a notoriously variable method [90]: repeated averaging, careful experimental design and detailed statistical analysis are required to draw a clear effect from the noise [91].

BOLD fMRI in white matter presents additional challenges. The reduced density of vasculature means that white matter has an inherently lower fraction of blood volume which leads to reduced amplitude of potential signal changes [92]. There is also evidence that white matter also has a more limited capacity for modulation of blood flow that grey matter [93]. These physiological features probably account at least in part for the difficulty of detecting a BOLD response in white matter.

2.8.2 Activity Induced Changes in Neuronal Tissue

Neuronal activation induces physical changes in nervous tissue. Changes in light scattering and transmittance induced by electrical stimulation in cortical slices have been demonstrated [94,95]. Activity dependent changes, specifically the shrinkage of the ECS has also been demonstrated in white matter [96]. These studies generally conclude that neuronal activity leads to cellular swelling which causes reductions in ECS volume. Ransom et al [96] discuss activity dependent ECS shrinkage in the rat optic nerve and demonstrate a correlation with the development and proliferation of glial cells in the nerve. This correlation holds even when controlling for the reduction in ECS caused by glial proliferation itself. In addition, an absence of ECS shrinkage in glial free, neo-natal nerves suggests that the impact of swelling of nervous processes themselves is negligible [97].

Cell volume regulation is highly dependent on anion transport systems [98], selective blocking of these systems reduces ECS shrinkage by up to 70% [99]. This reduction in ECS shrinkage indicates that anion transport systems play a strong role in activity induced changes in ECS volume.

During activation the membrane potential of neurons is reduced and intra cellular potassium ions are no longer held against their concentration gradient (see [100]). Because of this change, depolarisation leads to an increase in extra cellular potassium ions in mammalian white matter [101]. Glial cells appear to buffer local increases in potassium ions by taking them up in regions of high concentration and releasing them in areas of lower concentrations [102]. During this process the glial cells swell due to the osmotic changes caused by the ion influx. This swelling leads to reductions in the ECS volume. While applied increases in extracellular potassium ions lead to glial swelling in brain slices at concentrations of 10-20 mM and above [103], the small increases (<10 mM) induced by neural activation in adult rat white matter [101] are necessary for, but most likely do not directly cause, glial swelling [96]. Activity dependent events such as metabolic alterations in pH and local changes in partial pressure of O_2 and CO_2 [104,105] may be responsible for regulation of anion transport systems and therefore glial swelling.

2.9 Functional dMRI

dMRI has the potential to detect functional activation in neuronal tissue. If, during or after the propagation of electrical activation, tissue water populations are differently distributed, then accurate measurement of the dMRI signal could potentially detect this change. Indeed as discussed above, electrical stimulation has been shown to cause shrinkage of the ECS immediately after stimulation [96]. Functional diffusion MRI (dfMRI) has been investigated in human visual cortex grey matter. Work by Bihan et al [106] suggests that a significant changes to the water diffusion signal can be detected upon activation. However, a large proportion (if not all) of these detected changes have been shown, in a subsequent publication, to be caused by vascular effects [107]. The overriding impact of the haemodynamic effect on the fdMRI signal has been investigated in further detail by Rudrapatna *et al.*[108]. Work in white matter by Mandl *et al.* [109], using functional DTI as a metric for tract activation in humans, suggested that a detectable dMRI response is present upon activation. Here a two compartment model was used to attempt to remove the contributions of blood-flow, but it is unclear how successful this method is at eliminating vascular contributions. Osmotically driven ECS shrinkage (by application of excess potassium ions) is detectable with dMRI in white matter [67].

However, pure electrical stimulation in American bullfrogs (*Lithobates catesbeianus*) spinal cords and sciatic nerves has been shown to elicit no dMRI detectable effect at 22ºC [110]. Recent work in *in vivo* mouse optic nerve [111] attempted to separate vascular and functional contributions, the authors attempted to control for vascular effects and suggest they are able to detect a true, activation only effect. Despite this recent work the picture remains unclear. Vascular contributions cannot be ruled out *in vivo* and the precise nature and the magnitude of induced changes in physiologically real situations is unknown. Characterisation and demonstration of an effect which is truly independent of vascular effects is required before dfMRI can be developed for *in vivo* use and become an effective tool.

2.10 Additive Layer Manufacturing (3D Printing)

Additive layer manufacturing (ALM) or 3D printing, is the process of creating three dimensional objects in a large range of shapes, sizes and orientations from a digital model. 3D printing is an additive manufacturing method; layers of material are built up on one another, in iterations to create the final object (much like a stack of MR images). 3D printing is thus distinct from traditional manufacturing methods which are based on the removal of material from a starting block by cutting or drilling, a subtractive process. For example, in masonry and sculpture a block of stone is shaped into the final object by cutting away certain sections.

The first commercial 3D printer was developed in 1986 by “Chuck” Charles W. Hull, the co-founder of 3D Systems, (Rock Hill, South Carolina, U.S.A.). In his initial patent entitled “Apparatus for Production of Three-Dimensional Objects by Stereolithography” [112] Hull defined the term ‘sterolithography’ as a method and apparatus for making solid objects by successively printing down thin layers of the ultraviolet curable material one on top of the other.

A digital model of the desired object is produced in a suitable computer aided design (CAD) program which exports the model to the printer as a series of slices. The raw material for ALM is usually a powder, a resin or a photopolymer. There are two main methods of ALM which produce 3D models but differ in their basic methods. The first involves direct deposition of the build material into the required locations as defined by that particular slice of the digital model. The material may then be cured by simple cooling or by the application of light (typically ultra-violet) or chemicals. The second method is known as selective sintering; material is laid down evenly and then selectively solidified by application of light, heat or chemicals into the correct shape as defined by the digital model at that layer.

In this work a laser sintering ALM method is used; selective laser sintering (SLS) (Figure 2.10.1). The raw material is a fine powdered nylon. A smooth uniform layer of powdered nylon is laid down on the build area and a directed laser then heats the nylon in specific locations, sintering it into a solid in the required shape. The build area then moves down incrementally and a new layer of the powder is deposited on top. The second layer is then sintered, joining it to the first and the process continues until a full 3D model is produced. The finished model is embedded in a block of un-sintered powder which can then be blown away (usually with compressed air) to reveal the finished model. One of the side effects of this method is that the outer layers of the model are slightly porous due to the footprint of the laser (Figure 2.10.1 c); internal points receive more energy and are fully melted together while the outer fringes receive less and so are not fully melted in a smooth consistent form.

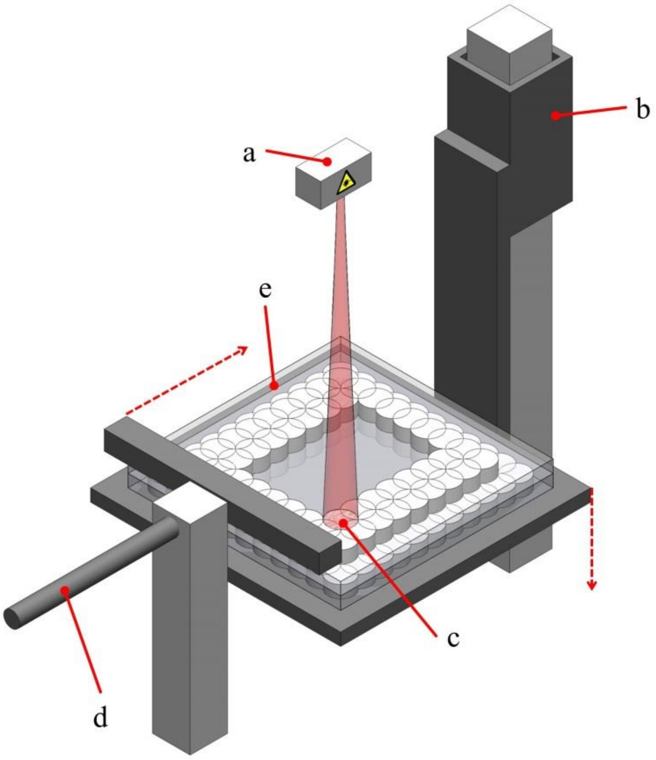

Figure 2.10.1: Selective Laser Sintering Diagram.

Showing a representation of the laser sintering mechanism; (a) the laser source with the laser beam in red, (b) the moving arm which shifts the build area down (dotted arrow) after each powder layer is added,(c) the laser sintering a point in the top powder layer, (d) the powder arm which moves across the build area and lays down a new layer of powder and (e) the powder layer (shown transparent). Continual layers and sintering in this example would produce a hollow pyramid shape.

The roughness of the outer layer is defined by the resolution of the printer (defined by the laser dot size and layer thickness), a finer resolution leading to smoother edges. Post print methods such as polishing can also be used to smooth rough edges but this becomes impractical on models with complex internal structures.

3.0 VIT Chamber: Design and Development

As discussed above, a stable and validated viable isolated tissue system would be of great use in the development and testing of pre-clinical dMRI methods.

This section describes the design and development of a viable isolated tissue maintenance chamber. The VIT chamber is the central subject and tool used in this thesis. The design brief, production and a description of technical hurdles encountered during the development of the original VIT chamber follow. The development of the chamber took up a large proportion of the time allocated to this PhD.

The initial design brief is described followed by the methods used in design and production of prototype chambers and the final design. This section concludes with a description of the major technical hurdles encountered and the initial performance testing experiments.

3.1 Initial Design Brief

Manufacture and develop a device capable of maintaining an isolated section of tissue at physiologically realistic temperatures. The device will be used with high field small horizontal bore MRI systems, specific requirements:

- The device will maintain a section of adult rat optic nerve (~10mm by 1mm cylindrical piece of tissue).
- The device must to be small enough to fit within a sensitive MRI volume coil, in this case a 26mm birdcage coil.
- The devices must enable in and out flow of perfusate and monitoring of the temperature of the perfusate.
- The device must prevent MRI distorting artefacts.
- The chamber must be compatible with grease gap electrophysiological recordings to monitor the stability of the optic nerve.

- The device must be able to maintain samples at physiological temperature, ~37ºC.

3.2 Design & Production

After considering all of the factors defined by the design brief, digital manufacturing was decided on as the method of choice. Additive layer manufacturing (see section 2.10) allows rapid prototyping of designs and iterative design optimisation. Initial designs for the device were created in the common computer aided design (CAD) software program (SolidWorks - Dassault Systèmes, Paris France). The chamber was manufactured from Fine Polyamide (PA-2200 nylon), using high-resolution selective laser sintering, on a P100 Formiga selective laser sintering system (EOS, Munich Germany).

The first design for the chamber was loosely based on a Perspex brain slice maintenance device for electrophysiology experiments [113], (Figure 3.2.1 a). Various developments and iterative design changes were made to this initial design to work around problems and improve the chamber until the finalised chamber was decided on. Figure 3.2.1 shows the progress of the design toward the finalised chamber, shown in Figure 3.2.2 and Figure 3.2.3.

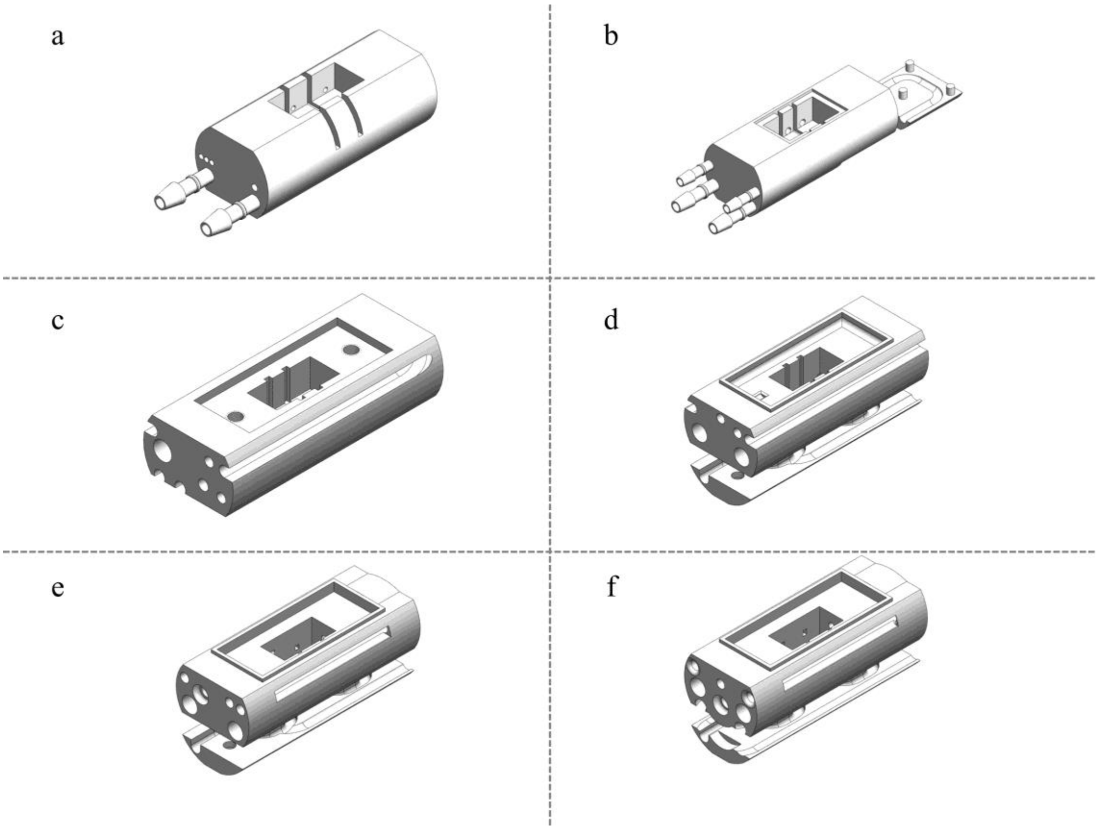

Figure 3.2.1: Chamber Design Progression.

Showing in panels a-f 3D CAD images of the progress of the chamber design. The first chamber design (a) is similar in design to the grease gap electrophysiology chamber in [113]. Iterative improvements for perfusate delivery and heating tubes can be seen in designs b – f. The rough dimensions of the chamber stayed the same (26mm diameter and ~65mm in length). Tubing and the temperature probe are not shown for clarity.

The final chamber consists of a central bath to hold the tissue sample and various in/out flow ports for perfuate.

Perfusate delivery was achieved by placing a powerful Reglo analogue peristaltic pump (Ismatec, Wertheim, Germany) outside of the scanner room (to mitigate RF noise produced by the pump and for magnet safety). The distance of the pump from the scanner bore meant that a heating system had to be built into the chamber itself as the perfusate would cool during its long transit time. Pre-heating was achieved by pumping hot water from a separate high velocity Haake B3 DC30 heating pump (ThermoFisher Scientific, Waltham, Massachusetts, USA), which is usually used for maintaining small animal body temperature, around the body of the chamber. The perfusate was then pumped through a winding track (Figure 3.2.3 c) in the chamber allowing enough transit time for it to reach the required temperature (by conduction of heat from the chambers body) before arriving at the central bath.

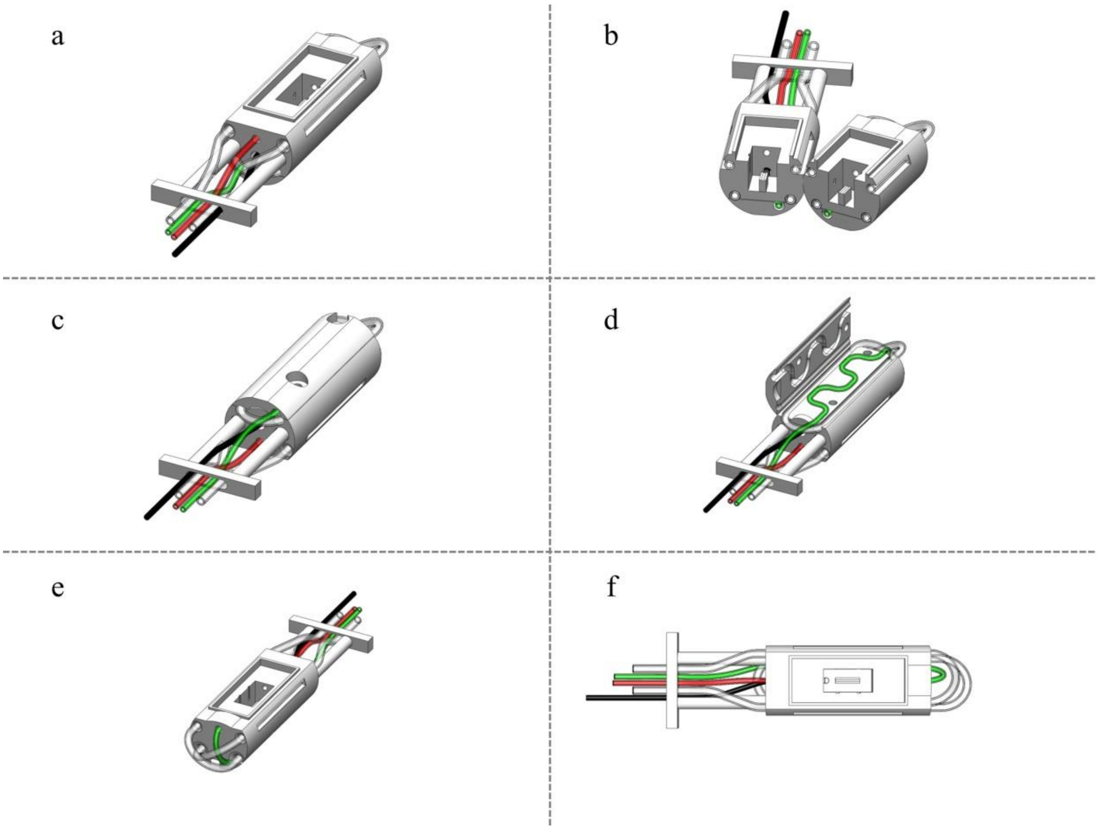

Figure 3.2.2: Final Chamber with Tubing.

Showing a range of views of the final chamber design with perfusate inflow, outflow, temperature probe and heating tubes shown in green, red, black and transparent respectively. Panel (a) shows the chamber from the front with the various tubes being held in place by the isocentre positioning bar. Panel (b) shows the chamber split in half at the sample bench position. The path of the heating tubes and inflow tube can be seen along with the end of the temperature probe. Panel (c) shows the underside of the chamber with the lower section in place, panel (d) shows the same view with the lower panel raised with the winding path of the inflow tube visible. Panels (e) and (f) show the layout of the heating tubes and the entry of the point at which the inflow tube pierces the main body of the chamber.

The P100 SLS system uses its un-sintered build material as a support for higher layers which means that the internal structure in the model is packed with nylon powder upon build completion. The complex winding track needed for the heating tubes and the perfusate inflow could not be easily cleared of un-sintered support material. Because of this the chamber was designed in two sections (Figure

3.2.3) so that the powder could be removed. PVC tubing was then inserted along the tracks and the sections connected around it with nylon screws.

Aside from these major design features, several smaller additions were made to enhance the device:

- A simple π shaped positioning bar was attached to the chamber, this ensured that the centre of the sample bench was always aligned with the isocentre of the magnet.
- A port through the chamber wall to the central bath was designed to accept a standard rat temperature probe (Small Animal Instruments Inc. New York, U.S.A.). A silicon o-ring was also built in to prevent leaks.
- The layout of heating and perfusate tubing around the central bath was arranged so that no MRI visible material was directly to the left or right of the sample; this enabled small FOV imaging of the sample with no wraparound water signal in the x direction (see Figure 3.2.2 b).
- Holes and flexible bars were designed to clamp the ends of the optic nerve to the central bench during MRI scans.
- Grease gap electrophysiology of the optic nerve (see section 4.1.5) requires the division of the central bath to create three electrically isolated chambers with the nerve piercing each one. To enable this, two inserts were designed (Figure 3.2.3 a) which locked into place.

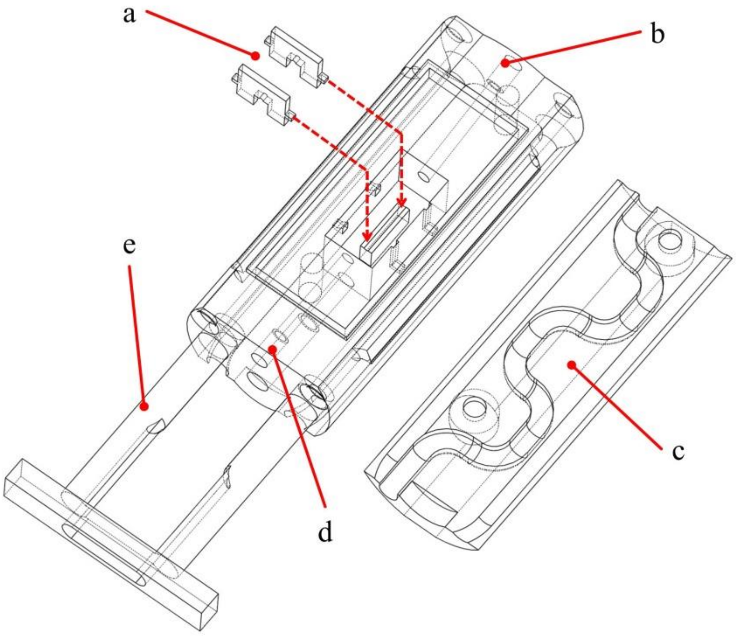

Figure 3.2.3: Final Chamber Wireframe Exploded.

Showing the MRI compatible incubation chamber (exploded), produced in nylon using 3D selective laser sintering. Circular diameter of the main chamber = 26mm. a) inserts for grease-gap electrophysiology which sit over the central bench to support the optic nerve, b) medium inflow, c) preheating system in lower section of chamber, d) medium outflow and e) tubing support and isocentre positioning bar.

3.3 Technical Hurdles and Initial Testing

As with all flowing liquid devices, the elimination of gas bubbles in the chamber was a crucial design hurdle. Gas bubbles can cause restrictions in flow and their sudden collapse can lead to regional increases in flow or turbulent behaviours, both of which can lead to temperature changes in the system described here. A bubble of air in a material of different magnetic susceptibility (e.g. water) also causes significant image artefacts in MRI [114]. Keeping the central bath bubble free was a high priority during the design process and informed many of the choices made.

The surface texture of PA-2200 nylon sintered in the P100 is rough and slightly porous. The surface finish is a product of the laser sintering method (see section 2.10). The internal structure of the model is non-porous and smooth. The rough surface and the hydrophobic nature of the nylon material means that any gas bubbles that encounter the inner surface of the bath tend to stay in place, resist movement and only grow in size over time. To overcome this problem the chambers inner surfaces were coated with an anionic, hydrophilic layer (in this case a commercial anti fog spray – 'Premium Anti-Fog Treatment', Muc-Off Ltd, Poole England). Surfactant was left on the chamber for 1 hour and any excess washed off with distilled water.

In a complex system such as the chamber it is very difficult to prevent bubble ingress entirely. Instead of attempting to create the perfect system features were designed to reduce the number and reduce the impact of any bubbles which did occur. One major source of bubbles was the de-gassing of perfusate as its solubility decreased during pre-heating. The perfusate was gassed (to provide the tissue with oxygen) prior to pumping it to the chamber, the cold perfusate then releasing its dissolved gas as it was heated to the required temperature in the chamber. A simple workaround for this issue was to gas the perfusate at a similar temperature to that produced by the chamber; a temperature controlled stirrer-hotplate was used for this purpose (C-MAG HS-7, IKA, Staufen, Baden-Württemberg, Germany). The liquid was thus heated and gassed, cooled while it was pumped through the tubes to the chamber and then 'pre-heated' by the chamber before encountering the tissue. This method drastically reduced the number of bubbles entering the chamber. A simple bubble trap was added to the inflow line external to the scanner, practically eliminating bubbles from the system. As a final safeguard for errant bubbles, the inflow aperture to the central bath was placed ~5mm from the sample bench, far enough to allow small bubbles entering here to rise to the surface without encroaching upon the imaging area. During bench testing of the chamber (Section 4.0), the same methods required for MRI stability were employed for consistency (surfactant, heating and cooling etc).

Temperature control and stability is a crucial design issue. Various designs and arrangements were tested until a suitable heating tube layout and inflow line path was selected. The flow rate of the perfusate was easily changed with the peristaltic pump and so iterative calibration of the heating water temperature and flow speed was made until the correct combinations were found. A feedback control system was initially considered but proved to be unnecessary as the chamber's temperature was found to be very stable over time (see Figure 3.3.1a). Because the perfusate constantly flowed in and out of the chamber, the temperature in the central chamber was found to be resistant to external temperature fluctuations (such as those caused by heavy duty-cycle MRI scans or cooling of the gradient coils), and to recover to a stable temperature rapidly after perturbation see Figure 3.3.1b.

Once a stable chamber was constructed the work could move on to a detailed validation of its performance maintaining rat optic nerves at physiological temperature.

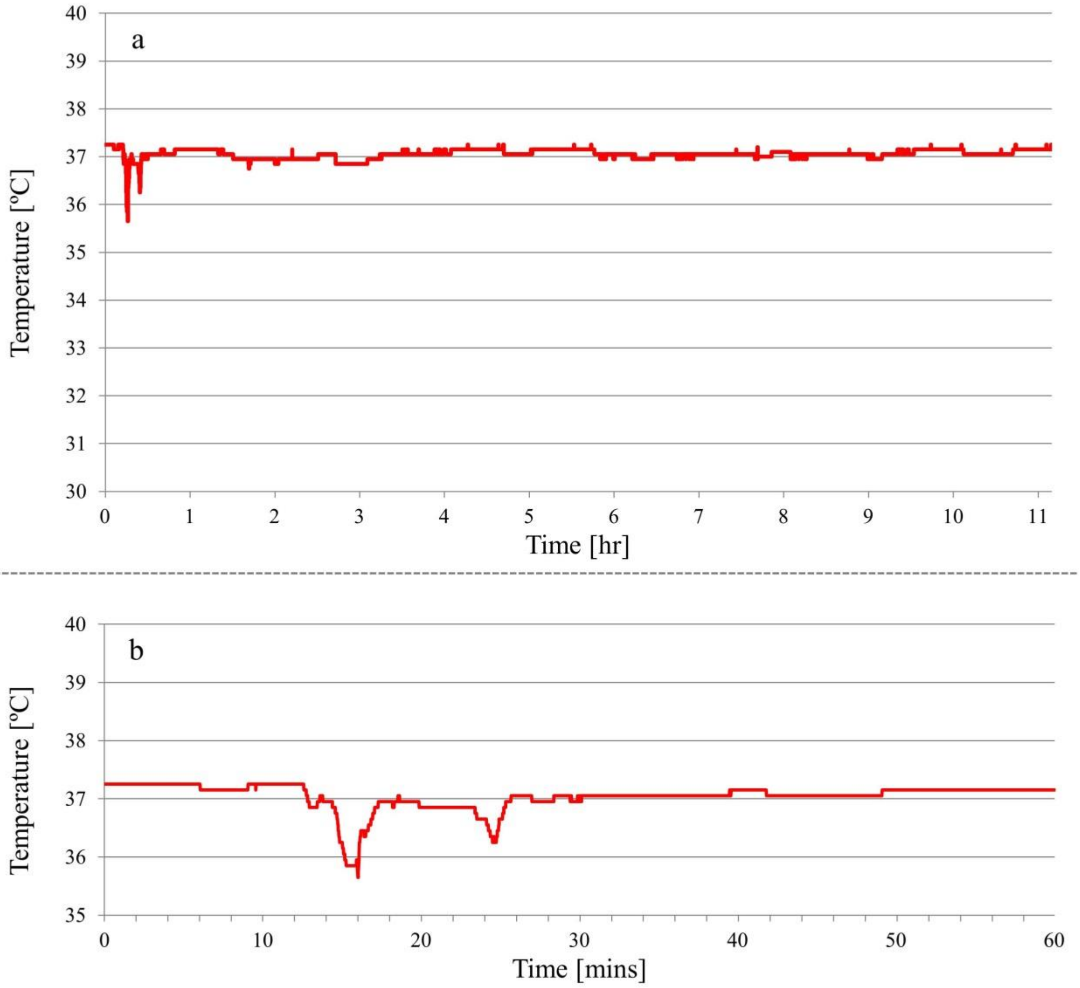

Figure 3.3.1: Temperature Recordings in the Chamber.

Showing a typical recording of the temperature in the central bath of the chamber during intense dMRI scanning. Panel (a) shows the entire trace over 11 hours, scanning began at hour 1. Panel (b) shows a zoomed in plot of the first hour of scanning. The hot water heating system was turned off at minutes 12, 14 and 23 for 30 seconds, 2 minutes and 1 minute respectively in order to demonstrate the stability of the system after perturbation. Average temperature over this time course was 37 ± 0.2 ºC

4.0 MRI Compatible VIT Chamber Validation

The previous section described the design and manufacture of the VIT chamber. Once constructed the VIT chamber needed to be validated to demonstrate its capabilities.

This section describes in depth testing and validation of the MRI compatible VIT maintenance chamber. The chamber was produced using additive layer manufacturing (see section 2.10). Rat optic nerve tissue maintained within the chamber was tested for stability using electron microscopy, electrophysiology and dMRI. The testing and validation of this chamber has been published in Magnetic Resonance in Medicine peer reviewed journal [9], additional data and information is included here. This testing and validation process was a crucial step, required before the VIT chamber could progress to applications, so a significant proportion of the thesis time was devoted to this work.

4.1 Methods

4.1.1 VIT Chamber

In depth details of the design and development of the VIT chamber are covered in section 3.0. Briefly, the chamber (Figure 3.2.3) was designed in the popular computer aided design suite SolidWorks, and exported as a high-resolution mesh file for production. The chamber was manufactured from Fine Polyamide, using high-resolution selective laser sintering, on a selective laser sintering (SLS) system. Fabricated chambers were fitted with heating tubes and in/out tubes allowing controlled tissue perfusion (see Figure 3.2.2).

Gassed artificial cerebrospinal fluid (aCSF), described in detail in the experiments section, provided the nerve with hydration, glucose, pH buffering, temperature control and oxygen. Temperature of the system was controlled by pumping heated water through a winding channel built into the body of the chamber.

4.1.2 Experiments

All MR measurements were conducted with a 20 cm diameter horizontal bore 9.4 T preclinical MRI scanner (Agilent Inc. Santa Clara, California, U.S.A) equipped with 1 T/m imaging gradients and a 26 mm diameter RF birdcage volume coil (RAPID Biomedical GmbH, Rimpar, Bavaria, Germany). The 26 coil was the smallest and most sensitive volume coil available at the time.

The aCSF used in this work contained (in mM): NaCl (120); KCl (2); $CaCl_2$ (2); $NaHCO_3$ (26); $MgSO_4$ (1.19); KH_2PO_4 (1.18); D-glucose (11); as in [40]. This mixture was gassed with carbogen (5% CO_2 & 95% O_2) to maintain a pH of 7.4.

4.1.3 Optic Nerves

Optic nerves were excised from adult Sprague Dawley rats (200-250g) after decapitation [40]. Sections of optic nerve running from immediately behind the eyeball to just in front of the optic chiasm (averaging 10 mm in length) were used for all experiments. After a series of practice extractions the average total extraction time reduced to was 3.5 minutes; average optic nerve diameter was 1.1 mm. Perfecting the extraction required 10-15 animals and these nerves were used for preliminary experiments with the VIT chamber.

4.1.4 Temperature, aCSF & Chamber Monitoring

During all experiments, the temperature of aCSF in the chamber was assessed using a temperature recording system (Small Animal Instruments Inc. Stony Brook, New York, U.S.A.). Temperature of aCSF within the chamber was maintained at 37.0 ± 0.2°C. Flow effects, liquid retention and air bubble formation within the chamber were assessed with multi slice gradient echo sequences: TR: 30 ms, TE: 5 ms, matrix: 128 x 128, flip angle: 20 degrees, 3 slices, 1 mm thick, FOV: 30 by 30 mm. These were also used to set-up dMRI and DTI acquisitions.

4.1.5 Electrophysiology

Grease-gap electrophysiology (similar to the method in [40]) was used to record CAPs from a viable rat optic nerve during maintenance within the chamber. Stimulus was delivered with a S48 stimulator (Grass instruments, Middleton, Wisconsin, U.S.A) and recorded with a HS-2A head-stage connected to an Axoclamp-2B microelectrode amplifier (Axon instruments Inc. – now Molecular Devices Sunnyvale, California, U.S.A). Recorded signals from the Axoclamp were fed through a low pass filter / amplifier (LPF-100, Warner Instruments, Hamden, Connecticut, U.S.A) and digitised with a Digidata 1322A (Axon instruments Inc.). A standard PC work station with pClamp software (Molecular Devices) was used to record the digital data trace. A Master-8 pulse stimulator (A.M.P.I, Jerusalem, Israel) was used for stimulus and recording timing (see Figure 4.1.1).

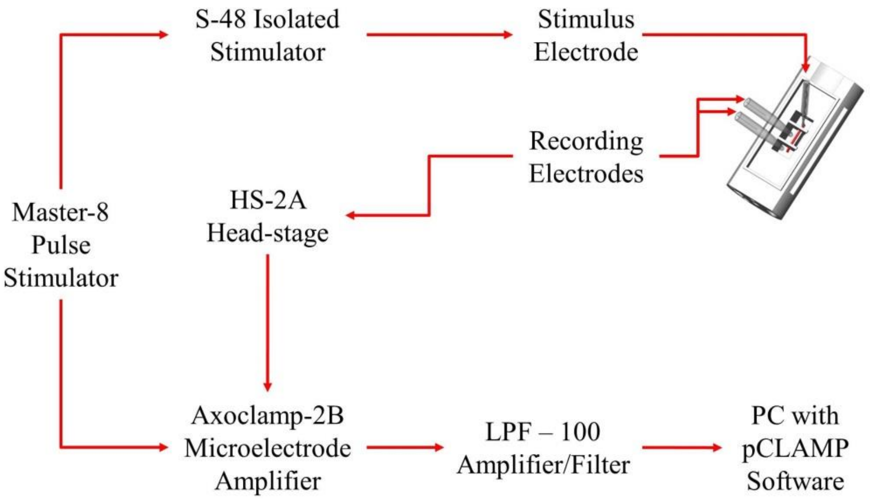

Figure 4.1.1: Grease-Gap Electrophysiology Equipment Set-up.

Showing a diagrammatic representation of the recording equipment used for grease-gap EP recordings from optic nerves in the chamber.

As shown in Figure 4.1.2, the chamber design included inserts to create three electrically isolated compartments; non-setting silicone grease was used around the edges of the inserts to create a water tight seal. Recording electrodes consisted of 1 ml syringes with a silver chloride (AgCl) coated silver wire embedded in agar. The stimulus electrode consisted of a pair of twisted silicon coated wires trimmed to expose the silver core at the contact end. Recording electrodes were placed into the aCSF of two adjacent compartments while the stimulus electrode was placed in contact with the end of nerve in the remaining compartment. This allowed stimulation of the nerve in the first and recording over the second and third compartments.

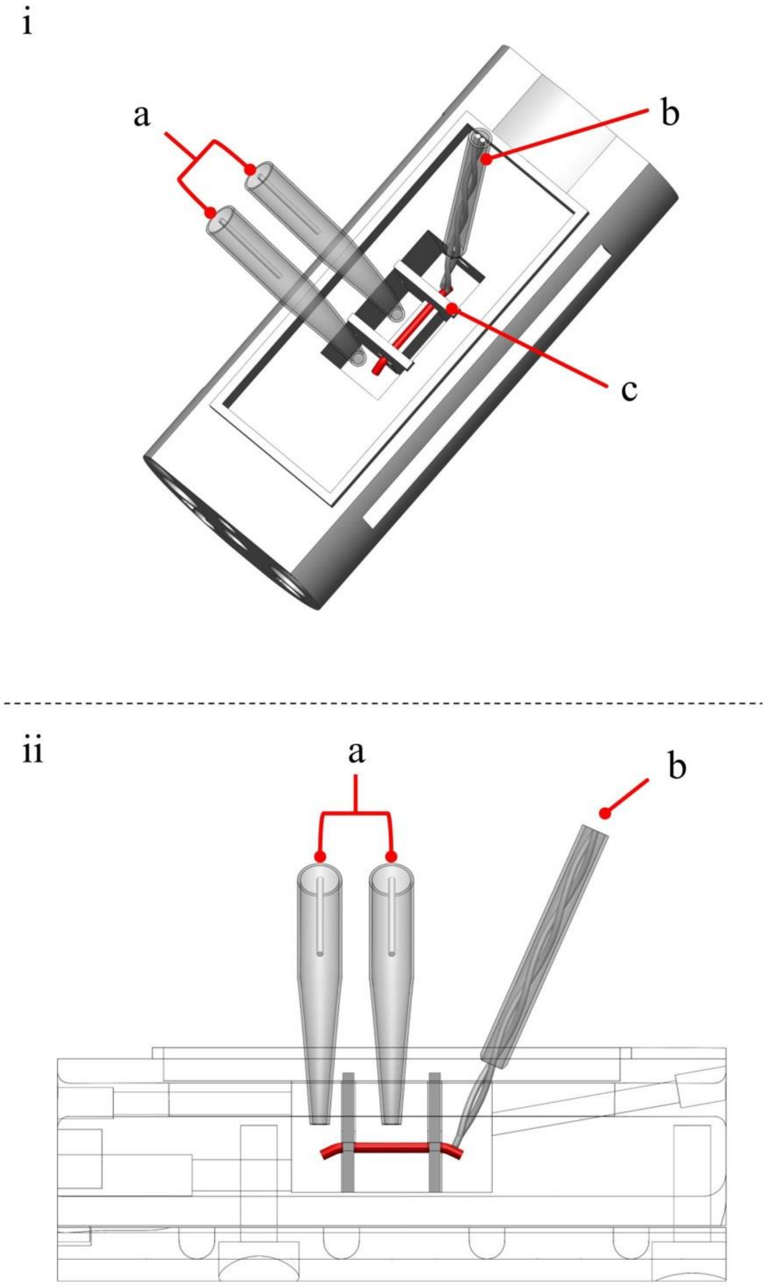

Figure 4.1.2: Grease Gap Electrophysiology Electrode and Chamber Setup.

Showing the recording (a) and stimulus (b) electrodes in the central bath. (i): An isometric view of the chamber with the isolation inserts (c) in place over the optic nerve in red and (ii): a side wireframe view of the same set-up.

Figure 4.1.3 shows a photograph of the grease gap recording equipment set-up with the chamber, the equipment was mounted on an earthed air table to reduce vibrations and electrical interference.

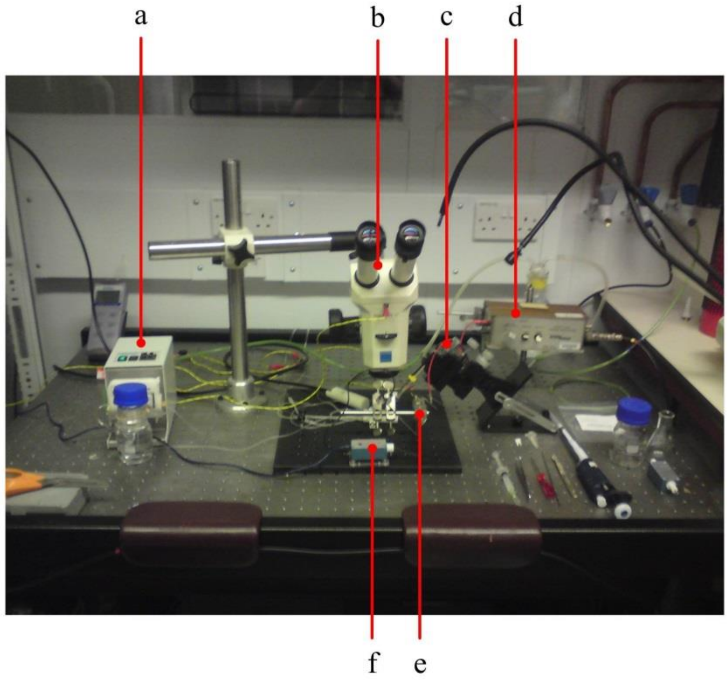

Figure 4.1.3: Photograph of the Grease Gap Recording Bench Set-up.

Showing an air table with the chamber bolted to it with the peristaltic pump (a), a Stemi Zeiss dissecting microscope (b) a custom stimulus electrode holder/manipulator (c), the isolated stimulator (d), recording electrode holder/manipulator (e) and the head-stage (f). Green and yellow wires are for earthing the equipment to reduce electrical noise in the recording.

The CAP was recorded following electrical stimulation of the nerve with rectangular voltage pulses: a stimulus rate of 0.01 Hz (70–110 V amplitude, 50 μs width) was maintained for 10 hours. To demonstrate the return to electrophysiological baseline of a compromised nerve, oxygen and glucose deprivation (OGD) was imposed for 2 hours by using aCSF containing no glucose and gassed with 5% CO_2 in N_2. OGD simulates an ischaemic insult to the nerve and induces irreversible loss of axonal function [115].

4.1.6 Electron Microscopic Histology

Transmission electron microscopy (TEM) was used to assess visible structural damage to axons within optic nerves over time. Rat optic nerves maintained in the chamber for 5 and 10 hours were compared to a freshly extracted and fixed control nerve (n = 1, 1 & 1 respectively). To demonstrate the structural effects of metabolic failure, a further nerve was subjected to OGD for 2 hours within the chamber. The freshly extracted, OGD and maintained nerves were fixed overnight in 4% formaldehyde and 2% glutaraldehyde solution and washed and stored in 0.1 M phosphate buffer (PB) (pH 7.4) prior to post-fixation in 2% osmium tetroxide (OsO_4) in PB for 1 hour. After dehydration, nerves were mounted in Durcupan resin and ultrathin sections (0.7 μm) were taken. Four 1000 μm^2 fields were taken from the centre of each of the four nerves, using a JEM-1010 (JEOL (Nippon Denshi), Tokyo, Japan) transmission electron microscope (5000 x magnification). Fibres of various diameters are homogeneously distributed across the rat optic nerve [116]. Therefore, sampling axons from the centre of the optic nerve (relative to both cut ends and the outer surface of the nerve) provides a representative sample of fibres throughout the nerve. The total internal areas of axons were measured using the image analysis software ImageJ (NIH, Bethesda, Maryland, U.S.A.) and its region of interest (ROI) analysis toolbox. The aspect ratio of each axon was also measured to assess circularity. Glial cell bodies, glial processes and blood vessels were excluded from the analysis. ~1000 individual axons were measured in each treated nerve. Detailed 20000 x magnification images were also taken for visual inspection.

4.1.7 Diffusion MR Measurements

Repeated dMRI measurements were acquired, once per hour, over 10 hours to assess the MR stability of VIT in the chamber. The stability of the dMRI signal from a viable nerve was compared to that of a fixed nerve (n = 1 & 1). Fixed samples were immersed in 4% formaldehyde solution for 24 hours then washed in 100 ml 0.1 M phosphate buffered saline (PBS) (pH 7.4) for 10 hours at 4°C prior to MR experiments.

The dMRI protocol is based upon [63], which is able to detect differences between VIT and chemically-fixed tissue. The extensive dMRI protocol, designed to maximize sensitivity to possible microstructural changes, is described in detail in Table 4.1.1. Briefly, 44 dMRI measurements with a range of b-values (incremented by increasing G), and 4 measurements without diffusion weighting were acquired each hour for 10 consecutive hours. Diffusion gradients were oriented perpendicular to the nerve. The duration of the diffusion encoding gradients (δ) was 3 ms and TR was 3700 ms. TE was minimised separately for each Δ and a measurement without diffusion weighting was included for each TE. 12 averages were taken for each individual measurement.

Hourly Acquisition											
Set #	Measure	Δ (ms)	G (T/m)	b-value (s/mm^2)	TE (ms)	Set #	Measure	Δ (ms)	G (T/m)	b-value (s/mm^2)	TE (ms)
1	0	10	0.0	0	24	2	0	20	0.0	0	34
	1		0.035	7			1		0.035	8	
	2		0.012	81			2		0.012	146	
	3		0.20	234			3		0.20	457	
	4		0.29	471			4		0.29	941	
	5		0.37	785			5		0.37	1598	
	6		0.45	1179			6		0.45	2428	
	7		0.53	1653			7		0.53	3431	
	8		0.62	2206			8		0.62	4608	
	9		0.70	2840			9		0.70	5957	
	10		0.78	3526			10		0.78	7480	
	11		0.87	4347			11		0.87	9175	
	12		0.95	5231			12		0.95	11044	
3	0	35	0.0	0	49	4	0	50	0.0	0	64
	1		0.015	7			1		0.018	7	
	2		0.076	184			2		0.092	184	
	3		0.14	600			3		0.17	598	
	4		0.20	1255			4		0.24	1250	
	5		0.26	2149			5		0.31	2104	
	6		0.32	3281			6		0.39	3268	
	7		0.38	4652			7		0.46	4633	
	8		0.45	6261			8		0.53	6237	
	9		0.51	8110			9		0.61	8077	
	10		0.57	10196			10		0.68	10156	
	11		0.63	12522			11		0.76	12472	
	12		0.69	15086			12		0.83	15026	

Table 4.1.1: MR Scan Parameters for Hourly dMRI Experiments.

Showing the MR scan parameters used for each hourly dMRI experiment on both viable and fixed optic nerves. Measurements without diffusion weighting are denoted measure ‘0’ in each section.

In order to acquire this protocol once per hour, a spatially selective signal acquisition [117] with no phase encoding was used. The slice positioning and frequency encoding directions relative to the nerve are shown in Figure 4.1.4 a. This method acquires a single line of voxels; their signal is gathered only from a cuboid 1 x 1 x 10 mm encompassing the nerve. A matrix of 128 x 1 was acquired for each dMRI measurement. Voxel dimensions were thus: 1 x 1 x (10/128) = 0.078 mm^3. A ROI was used to select ~100 voxels from the central 8 mm of the nerve in order to avoid the cut ends. To remove T_2 relaxation effects, the average signal (S) of the 128 x 1 matrix was normalized using the average signal of the measurement without diffusion weighting (S_0) for that set: (S/S_0).

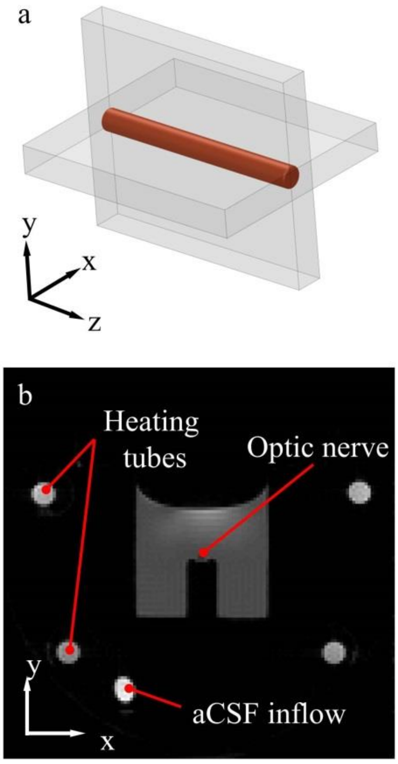

Figure 4.1.4: The Geometry of the Slice Selection Method and an MRI of the Chamber.

Showing in (a): The geometry of the two independently positioned slice selective, excitation and refocus pulses around the optic nerve (cylinder). Frequency encoding was in the z direction. And (b): Gradient echo MRI image of the system (x-y plane), showing the optic nerve on the central bench immersed in aCSF, the four surrounding heating tubes and the single aCSF inflow tube below.

4.1.8 Diffusion Tensor Imaging

In addition to the detailed dMRI measurements, a repeated 6 direction DTI dataset was acquired from separate VIT and fixed nerves (n = 1 & 1). A single axial imaging slice, 2 mm thick, FOV: 6 by 6 mm, matrix: 64 by 64, positioned in the centre of the nerve was acquired every hour for 10 consecutive hours. TR: 5000 ms, TE: 30 ms, G: 0.22 T/m Δ: 20 ms δ: 3 ms, 6 directions: [Gx,Gy,Gz] = [1,1,0], [1,0,1], [0,1,1], [-1,1,0], [0,-1,1] and [1, 0, -1]. A ROI covering the centre of the nerve was selected (10 voxels). Fractional anisotropy (FA) and diffusivities were calculated using the open source CAMINO software package [118] to fit a non-linear diffusion tensor model [119].

4.2 Results

4.2.1 Chamber Performance

The chamber (Figure 3.2.3) is suitable for MR measurements: The nylon construction material of the chamber shows no proton MR signal at the shortest achieved echo times (0.5 ms). The chamber is also suitable for grease-gap electrophysiology recordings: With the inserts (Figure 3.2.3a) three electrically isolated chambers can be created and maintained. From room temperature, the chamber requires 10 minutes to achieve a stable temperature of 37.0 ± 0.2°C which was maintained for the duration of experiments. The MRI bore temperature (17.5 ± 1°C) did not affect the temperature maintenance of the chamber (data not shown). Leaking of aCSF or heating water was not observed. The chamber has been found to be reliable, consistent and reusable.

4.2.2 Electrophysiological Recordings from Optic Nerves

Electrophysiological recordings demonstrated that optic nerves in the chamber maintained electrophysiological viability over 10 hours (Figure 4.2.1a). The peak amplitude of the primary peak of recorded CAPs remained above 4 mV for the duration of the experiment and showed no significant trend over time ($P > 0.05$, linear regression). The lack of a Faraday cage around the set-up, caused transient electrical interference (outliers in the data shown in Figure 4.2.1a) but these are non-systematic and so do not affect the conclusions. Optic nerves produced CAPs with amplitudes of 4.0 ± 0.25 mV, up to 15 hours post extraction (data not shown). The amplitude of the primary peak of the CAP degraded to baseline (0 mV) after 2 hours OGD (Figure 4.2.1b). This is consistent with previous findings in an ischaemic rat optic nerve model [120]. An example of a typical CAP recorded with this system is shown in Figure 4.2.1c.

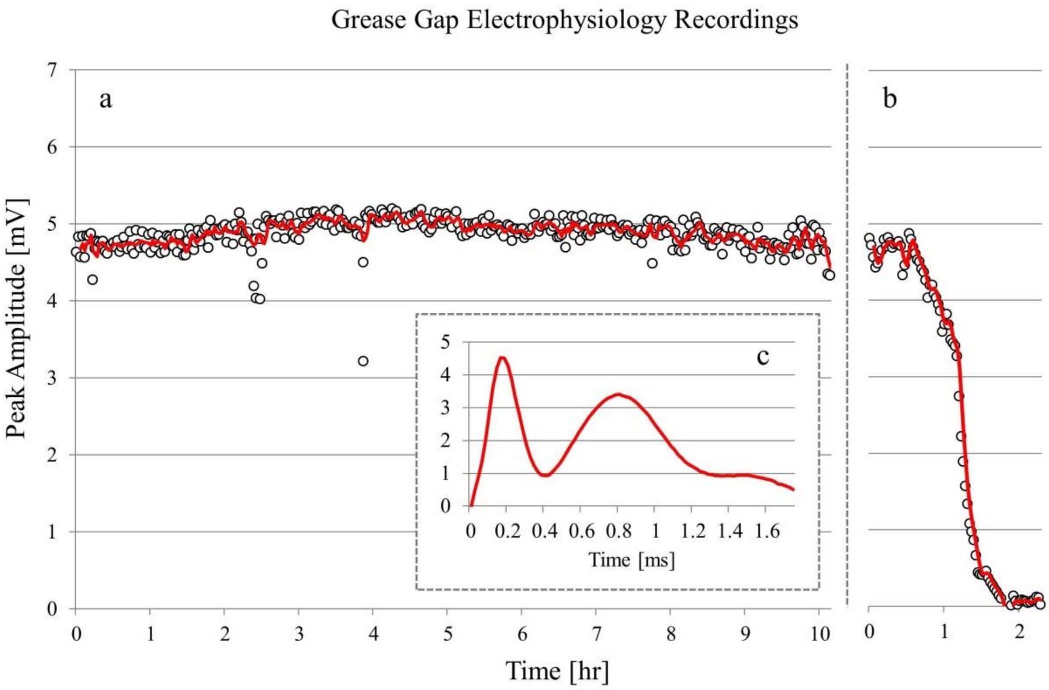

Figure 4.2.1: Grease Gap Electrophysiology Recordings.

Showing in (a): electrophysiological measurements of the average peak amplitude of the compound action potential produced by a single viable optic nerve over 10 hours maintenance within the chamber. (b): the same nerve treated with aCSF minus glucose and oxygen for 2.5 hours – oxygen and glucose deprivation (OGD). Outliers are due to electrical interference during the course of the scan. The red line represents the moving average (period 3) with outliers excluded (1.6% of data). (c): a typical recorded compound action potential.

4.2.3 Assessment of Tissue Structural Integrity

Transmission electron micrographs demonstrated the structural stability of optic nerves over 10 hours within the chamber (Figure 4.2.2). Visual inspection of electron micrographs indicated a comparable degree of neuronal survival and structural stability between the control (immediate fixation), and both 5 and 10 hour maintained samples (Figure 4.2.2a, b and c respectively). A nerve subjected to OGD for 2 hours (Figure 4.2.2d), demonstrated structural changes in the tissue due to metabolic failure.

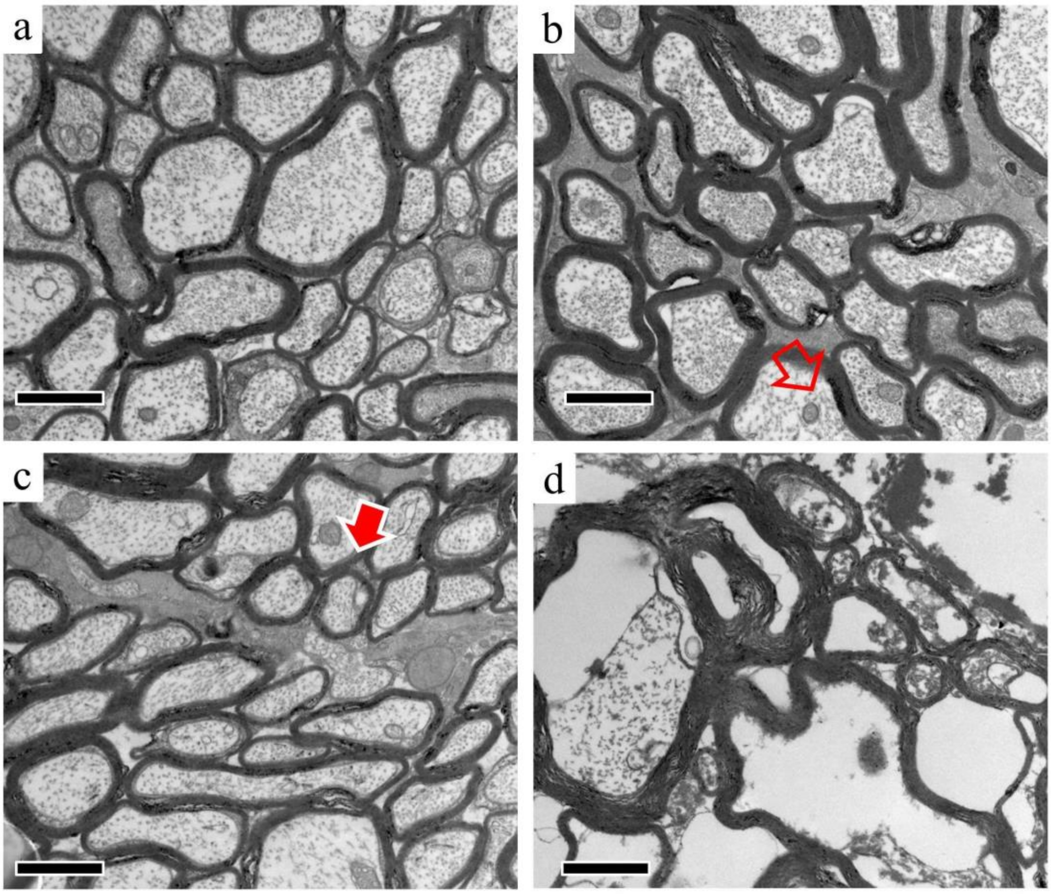

Figure 4.2.2: Electron Micrographs from Optic Nerves.

Showing sections of transmission electron micrographs at 20000 times magnification taken from four differently treated optic nerves: a) immediately fixed upon extraction, b) aCSF for 5 hours within the chamber, c) aCSF for 10 hours within the chamber and d) oxygen and glucose deprived for 2 hours. Open arrow shows a healthy mitochondrion, solid arrow shows compact myelin layers surrounding axons. Scale bars represent 1 µm.

The damaged sample shows reduced organisation of microtubules, severely damaged astrocytes, less dense myelin layers and separation of myelin from the cytoplasm in 100% of observed axons. Averaged areas and aspect ratios calculated from measurements of axons (at 5000 x magnification) within each treated nerve are shown in Table 4.2.1. Samples (a), (b) and (c) show a similar magnitude and variation in areas and aspect ratios ($P >> 0.05$, t-test). The OGD nerve (d), shows both a greater variation and a significant increase in axon areas in comparison to the immediate fixation control nerve ($P < 0.05$, t-test) and a significant reduction in aspect ratio (more rounded axons). The electron-micrographs used for data analysis in this section are shown in full in Appendix 1.

Treatment	Area (μm^2)	Aspect Ratio
(a) Immediate fixation	0.86 ± 1.0	2.5 ± 1.3
(b) aCSF 5 h	0.77± 0.9†	2.4 ± 1.1†
(c) aCSF 10 h	0.89 ± 1.0†	2.4 ± 1.2†
(d) Oxygen and Glucose Deprivation	1.2 ± 1.8*	1.8 ± 0.6*

Table 4.2.1: Structural Measurements from Electron Micrographs.

Showing average axon area and aspect ratio (± 1 standard deviation) taken from transmission electron micrographs of treated optic nerves. Axons were sampled over four 1000 μm^2 fields (5000 x magnification) positioned in the centre of each nerve, covering approximately 1000 axons per sample. *: significantly different to immediate fixation control ($P < 0.05$, t-test), †: not significantly different to immediate fixation control ($P >> 0.05$, t-test).

The expanded average axon area apparent from Table 4.2.1 in the OGD sample is somewhat misleading as to the actual changes. The average is affected by a few highly enlarged axons within the OGD sample which skew the average. A line histogram (Figure 4.2.3) demonstrates the pattern of change in the majority of smaller axons more clearly. The few greatly expanded axons overpower a general shift toward slightly smaller areas in the bulk of axons. The aspect ratio shows a different pattern (Figure 4.2.4): the difference in the OGD sample average is driven by the bulk of the axons increasing in circularity (lower aspect ratio).

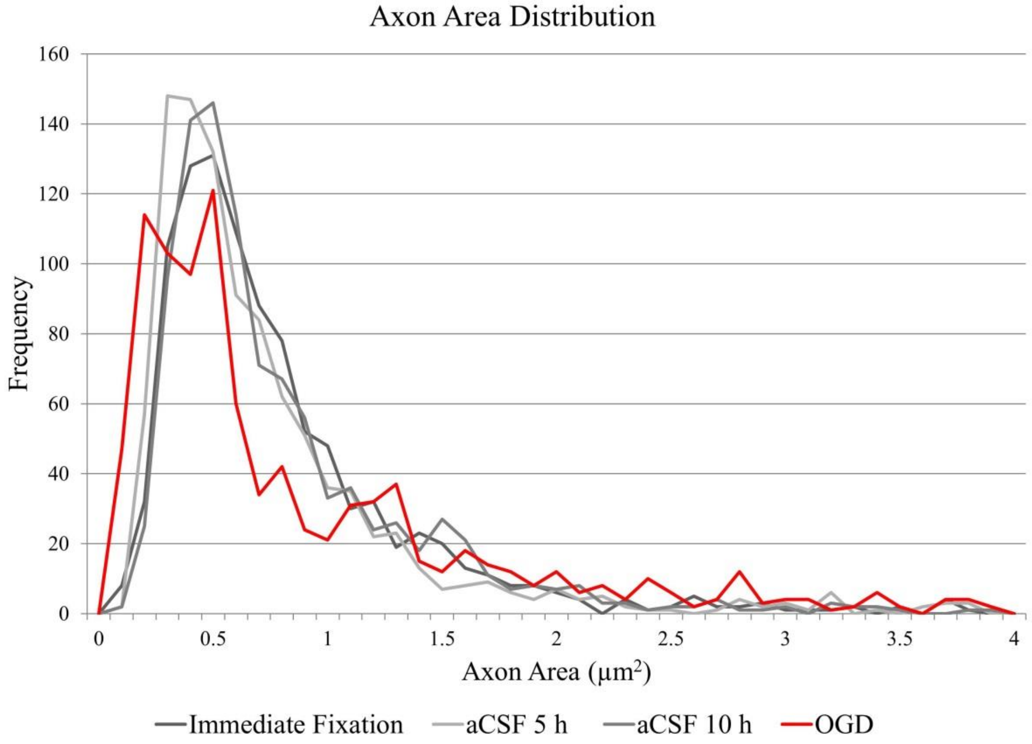

Figure 4.2.3: Line Histogram of Axon Areas.

Showing a line histogram of the frequency of axon areas in the 1 to 4 µm^2 range in the four samples, the greyscale lines represent maintained healthy nerves while the red shows the OGD nerve (see legend for details).

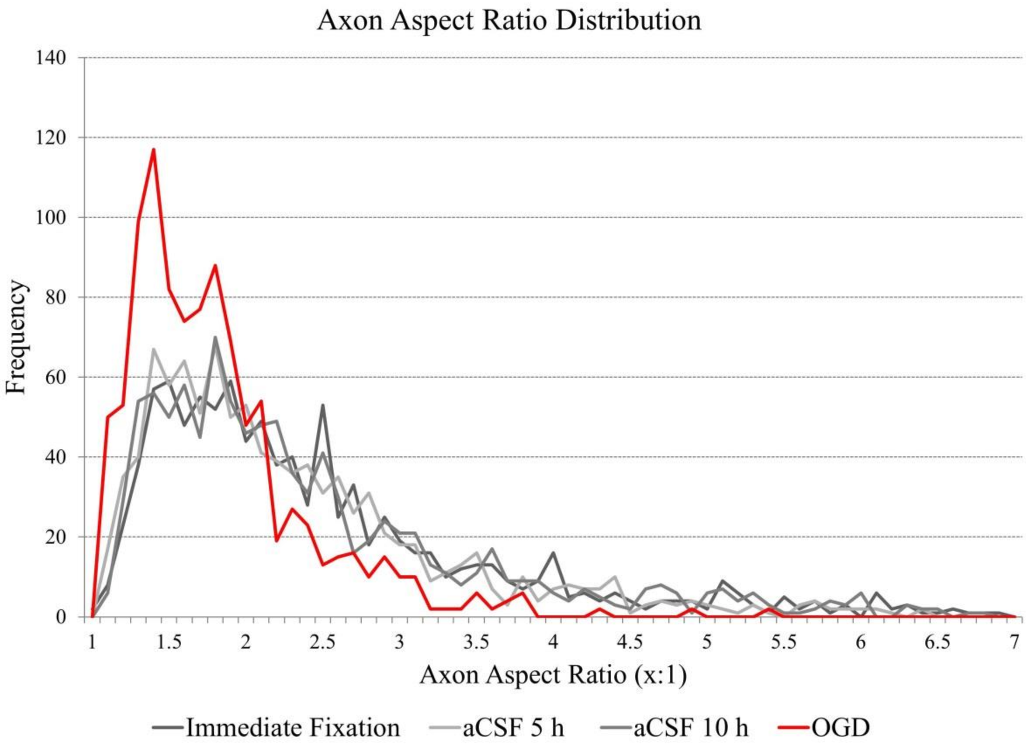

Figure 4.2.4: Line Histogram of Axon Aspect Ratio.

Showing a line histogram of the frequency of axon aspect ratios in the 1 to 7:1 range in the four samples, the greyscale lines represent maintained healthy nerves while the red shows the OGD nerve (see legend for details).

4.2.4 MR Measurements

dMRI measurements demonstrated the signal stability of optic nerve tissue maintained in the chamber over 10 hours in comparison with fixed tissue (Figure 4.2.5). Variability in averaged signals over time is comparable in both the fixed and live nerves at all b-values and diffusion times. For example, at a b-value of 9000 mm^{-2} s and Δ of 50 ms, the standard deviation of the averaged measured signals over 10 hours = 0.027 (fixed) and 0.035 (VIT). Signal attenuation at high b-values is markedly increased in the fixed nerve, indicating a higher diffusivity in the fixed sample. Gradient echo imaging throughout the 10 hour dMRI experiments demonstrated no air bubble formation, either on the surface of the tissue or on the inner surfaces of the chamber (e.g. Figure 4.1.4b.).

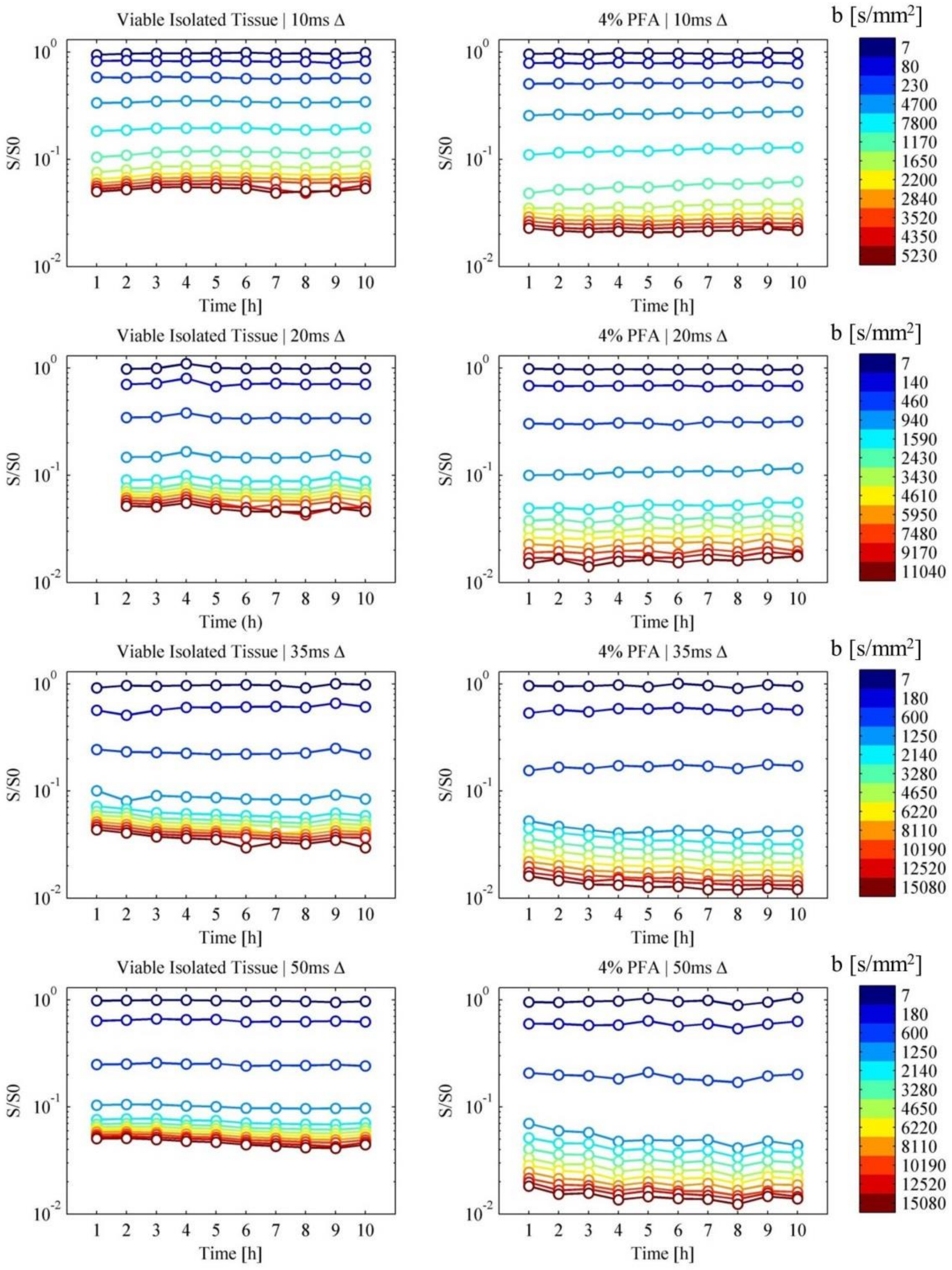

Figure 4.2.5: Diffusion Weighted Signal Attenuation Plots in Viable and Fixed Nerves.

Showing representative semi-log diffusion-weighted signal attenuation plots from MR experiments on a viable (left) and a fixed (right) optic nerve. Points represent the average signal along the length of the optic nerve. Both nerves were scanned once per hour at four diffusion gradient separations (Δ = 10, 20, 35 and 50 ms) and a range of b values (7 - 15086 s/mm^2) for 10 hours. The acquisition of VIT measurement 1 (20 ms) failed - this data point has thus been omitted.

DTI data further demonstrated the comparable stability of viable and fixed samples (Table 4.2.2). No trend in FA, MD or RD in either sample over the time course was apparent (P >0.05, linear regression) and variability between samples was comparable.

Time (h)	FA		RD ($\mu m^2/s$)		MD ($\mu m^2/s$)	
	VIT	Fixed	VIT	Fixed	VIT	Fixed
1	0.77	0.71	226.96	406.50	539.47	686.03
2	0.82	0.68	259.32	400.86	540.52	660.20
3	0.78	0.71	282.68	353.33	566.13	583.83
4	0.76	0.71	273.50	360.56	580.22	630.50
5	0.78	0.66	292.40	402.52	582.28	666.86
6	0.81	0.69	250.51	351.31	516.91	621.11
7	0.80	0.69	233.76	357.33	523.94	623.06
8	0.79	0.68	234.14	384.12	555.67	649.95
9	0.73	0.69	264.32	359.02	530.52	621.87
10	0.77	0.68	231.96	393.55	529.47	671.07
Mean	0.78	0.69	254.95	376.91	546.52	641.45
σ	0.03	0.01	21.99	21.49	22.14	29.17

Table 4.2.2: DTI Parameters from Viable and Fixed Optic Nerves.

Showing fractional anisotropy (FA), radial diffusivity (RD) and mean diffusivity (MD) calculated with non-linear diffusion tensor fitting, from hourly 6 direction DTI acquisitions in both viable and fixed rat optic nerves. RD and MD. Units are μm^2 per second.

4.3 Discussion

4.3.1 Validation Methods

Electrophysiological recordings of action potentials from optic nerves maintained within the chamber demonstrated their maintenance of electrophysiological viability over time. In contrast to this, compromised cellular metabolism is detectable as a reduced CAP amplitude [66], as demonstrated in the OGD experiment (Figure 4.2.1b).

Electron microscopic images of optic nerves demonstrated the structural stability of the tissue. In both maintained samples and in the fresh control, microtubules are present and evenly distributed throughout the axon and the mitochondria appear healthy. Previous studies on rat optic nerves deprived of oxygen and glucose have demonstrated a characteristic set of structural changes [40]. In the maintained samples, myelin layers surrounding some axons (≈ 1 in 100) also show a degree of separation from one another. This is seen to an equal degree in both the control and maintained samples and is therefore likely due to histological processing artefacts. Representative radii estimates are difficult to acquire as the axons vary greatly in size and shape (see Figure 4.2.2) and are not usually circular or ellipsoid. The aspect ratio of the axons can however be informative; the OGD treatment causes a significant negative change in the aspect ratio of the axons, probably due to cell swelling. Some variation in the healthy maintained nerves axon areas (Figure 4.2.3) is apparent. However, this variation is considerably smaller than that between the immediate fixation and the OGD nerves and is likely due to inter-animal variability. Total areas and aspect ratios were selected for stability metrics as these represented the greatest visible changes in the morphometric of ODG damaged nerves; these metrics are thus most likely to be sensitive to subtle changes in the tissue.

Detailed dMRI and six direction DTI acquisitions were used to test the microstructural stability of both viable and fixed optic nerve tissue. The attenuation of the dMRI signal was found to be significantly increased in the fixed nerve compared to that of the viable optic nerve. In addition MD and RD calculated from DTI were increased in fixed tissue ($p<0.05$, t-test). This is consistent with previous findings on VIT at room temperature using a similar dMRI protocol [63]. Previous studies comparing *in vivo* and fixed tissue, e.g. [72], show lower apparent water diffusion coefficients in fixed tissue than *in vivo* tissue. However unlike this study, the fixed tissue measurements in [72] were acquired at room temperature rather than physiological temperature.

In both the fixed and viable optic nerves, minor variations from the mean signal are seen; these are likely to be caused by scanner instability over the extended time periods used. These data demonstrate that the dMRI signal stability of viable nerves is comparable with that of fixed optic nerves, which are inherently structurally stable.

The spatially selective signal acquisition was chosen to allow repeated detailed dMRI measurements. Initially 0.5 mm slice thicknesses were chosen, but positioning these correctly proved difficult so the 1.0 mm slices described above were chosen. This meant that the MR volume sampled included an aCSF partial volume of ~5% which was the same in both samples as fixation did not lead to visible shrinkages in the nerve diameter. The aCSF signal was fully attenuated at low b-values and so while this partial volume lead to a greater attenuation than would be seen in pure tissue ROI's, it does not affect the assessment of comparative temporal stability from this data. DTI data included no aCSF partial volume.

4.3.2 Temperature & Bubble Formation

Temperature within the MRI VIT chamber is stable for ten hours. Temperature control within the chamber is an important consideration. Rat brain tissue oxygen consumption (an indication of metabolic activity), has been shown to increase by 20% with a temperature increase of 2.5°C [121]. Molecular motion is highly sensitive to changes in the environmental temperature and an increase in tissue temperature increases the self-diffusion of water [74]. In addition, a temperature difference of 17°C has been shown to produce marked changes in transmembrane water exchange rates in isolated tissue [75]. Without the use of a surfactant on the inner surfaces of the chamber gas bubbles were seen to form. A non-ionic surfactant readily absorbs into the chambers material and prevents bubble formation. No deleterious effects on the tissue due to surfactant application were found. Comparisons to preliminary electrophysiology work without surfactant supported the expected conclusion that the chamber's surfactant coating does not damage the tissue.

4.3.3 Time Limits

Previous studies suggest that isolated rat optic nerves maintain electrophysiological activity for longer periods post extraction [122]. However, removal of the cell bodies from the axons during tissue extraction rules out any further protein manufacture by the cell: progressive structural damage therefore accumulates over time. The stability of VIT in the chamber demonstrated here leads to the conclusion that, using this system, data can be acquired from a stable sample for up to 10 hours: this is a conservative upper limit for stable acquisitions using VIT and even longer acquisition times may well be possible. During preliminary EP experiments with the VIT chamber, extracted nerves produced strong CAPs 14 hours after extraction from the animal. Anecdotally, colleagues in UCL's electrophysiology lab have been able to record CAPs from optic nerves extracted the previous day and left at room temperature in aCSF on the bench.

4.3.4 Manufacturing, Costs and Design Considerations

The chamber manufacturing method ensures stability and reproducibility. The chamber consists of homogeneous nylon which is ideal for use with MRI: the magnetic susceptibility of nylon is less than 3 ppm different from that of water (30). Furthermore, identical chambers can be reproduced economically and rapidly using a modern SLS system (total production cost per unit as of 2012 ≈ 50 GBP).

While the chamber has been designed to fit into a small (26 mm) birdcage coil, the aggregate volume is significantly larger than the sample volume. High SNR data can be acquired with this set-up but the quality of MR data could potentially be improved by using a surface coil. The current design is compatible with surface coils; these can be positioned within 5 mm of the tissue sample. In addition, the design of the chamber is easily modified, enabling opportunities for investigation of specific properties of various VIT samples.

4.3.5 Conclusion

The chamber described here allows the use of MR protocols that can finely sample parameter space and produce artefact-free datasets from physiologically stable isolated rat optic nerve tissue. For example, this chamber is suitable for evaluating and comparing white matter models of water diffusion [53] or magnetisation transfer [123]. The chamber has been designed to allow access and controlled perturbation of VIT during MRI acquisitions. The chamber is therefore suitable for studies into a range of pathological conditions and could potentially be used to assess MR detectable effects of drug administration and tissue perturbation.

Based on the success of these validation experiments I was confident that the chamber would provide a stable platform for the planned research described below.

5.0 VIT and Fixed Tissue Comparison

The previous section described the testing and validation of the VIT chamber with a section of rat optic nerve tissue. The validated chamber provided a stable system to investigate dMRI properties of isolated tissue in detail.

This section describes a dMRI comparison of fixed and VIT rat optic nerves in identical conditions at physiological temperature using the chamber. Fixed tissue is commonly used in developing MRI and dMRI methods before moving to *in vivo* work. The primary motivation for this work was therefore to provide guidance for these studies by comparing indices calculated from dMRI measurements of fixed and viable tissue. A secondary motivation was to investigate how this comparison depends on the imaging parameters used to acquire dMRI data. Section 2.6 covers the current state of validation efforts in dMRI to which this work aimed to add. DTI data sets were acquired with a range of acquisition parameters and detailed dMRI datasets for microstructural model fitting. The chamber enables more detailed measurements such as those required for a complex model fitting comparison than could be achieved with *in vivo* white matter. Data in this section has been published in the Magnetic Resonance in Medicine peer reviewed journal [10].

5.1 Methods

The VIT maintenance chamber and optic nerve extraction procedure used in this work were as previously described above in sections 3.0 and 4.0. All MR measurements were conducted with the 9.4 T MRI scanner described in above (section 4.1.2) equipped with 1 T/m imaging gradients and a 26 mm diameter RF birdcage volume coil, again as previously described. The aCSF used in this work was as described in section 4.0.

Optic nerves, both viable and fixed, from male Sprague Dawley rats (250-300g) were extracted as described in section 4.1.3. During all the experiments below, nerves were secured in the chamber and perfused with oxygenated aCSF at 37ºC. Fixed samples were prepared by immersion in 4% buffered formaldehyde solution (4°C) for 24 hours immediately after extraction. Prior to MR experiments fixed nerves were washed in 100 ml 0.1 M phosphate buffered saline (PBS) (pH 7.4) for

10 hours at room temperature. This washing step is important as formaldehyde has been shown to cause significant reductions in T_2 [63].

5.1.1 DTI (Experiment A)

DTI experiments (numbers: A1, A2 and A3) were designed to compare DTI indices obtained from VIT and fixed tissue and to establish the dependence of these indices on acquisition parameters for both.

A range of pulsed-gradient spin-echo DTI experiments was conducted on VIT and fixed nerves (n= 3 & 3) with varying diffusion gradient separations (Δ: 10, 20 & 30ms), gradient durations (δ: 4, 6 & 8ms) and gradient amplitudes (G: 0.32 – 0.71 T /m) applied along 30 non-collinear diffusion directions. Three measurements without diffusion weighting were included in each experiment. Other acquisition parameters were: TR: 1500 ms, matrix: 48x48, FOV: 6 x 6 x 2 mm, slice orientation: axial. Total scan duration for each sample was 5 hours, 56 minutes. Table 5.1.1 shows the DTI acquisition parameters for experiments A1, A2 and A3. In experiment A1, Δ and δ were fixed while G was varied. In experiment A2, G was fixed while Δ and δ were increased. Finally, in experiment A3, G was fixed and the b-value was maintained over a range of Δ by altering δ. Experiments A1 and A2 were both designed to study the variation of DTI indices as a function of b-value. However, in experiment A1, b-values were varied by changing gradient strength, i.e. G, while in A2 b-values were varied by changing diffusion time, i.e. Δ. Experiment A3 aimed to probe the effects of increasing Δ at constant b-value. SNR of images at the longest echo time used (36 ms) was 11.9:1. Due to the highly anisotropic nature of the optic nerve samples, signal attenuation is greatly increased parallel to the nerve. The DTI protocol was designed so that the most attenuated signals from the optic nerve still have SNR >1.5.

		Parameters				
Experiment	Step #	b-value (s/mm^2)	δ (ms)	Δ (ms)	G (T /m)	TE (ms)
A1	1	1016	4	10	0.32	17
	2	2481	4	10	0.50	17
	3	5002	4	10	0.71	17
A2	1	935	4	8	0.35	23
	2	2525	6	10	0.35	23
	3	5236	8	12	0.35	23
A3	1	2525	6	10	0.35	36
	2	2618	4	20	0.35	36
	3	2288	3	30	0.35	36

Table 5.1.1: Acquisition Parameters for Experiment A.

Showing acquisition parameters for each step of the three DTI experiments in experiment A.

5.1.2 Multi Direction Multi b-value dMRI (Experiment B)

In order to compare fixed and VIT in an application that uses sophisticated white matter models, a highly detailed multi-direction-multi-b-value dMRI dataset (adapted from [53]) was acquired from VIT and fixed nerves. The 1D method used in section 4.0 was not used here as it leads to unacceptable partial volume effects which would have had an impact on the model fitting.

Two sets of dMRI images totalling 198 images, were acquired in the same session from each nerve (n=1 VIT and 1 fixed). Set 1 parameters: [Δ: 10, 20, 35, 50ms | δ: 3ms | G: 0.04 – 0.4 T/m in nine steps of 0.04 T/m]. Set 2 parameters: [Δ: 30 & 40ms | δ: 15ms | G: 0.04 – 0.15 T/m in four steps of 0.0275 Tm]. In the parallel direction the maximum gradient strength was limited for the longer (15ms) δ measures (set 2) to 0.1225 T/m to prevent acquisitions in the noise floor. This prevented acquisition of data points with an SNR < 2.0. Images without diffusion weighting, with echo times matched to the dMRI measures were taken for normalization; 6 in total. In the chamber the optic nerve is aligned parallel with the bore. One parallel & three perpendicular diffusion gradient direction measurements (see Figure 5.1.1) were taken for each δ, Δ and G combination. Other acquisition parameters were: TR: 2000 ms, TE: minimised for each diffusion time setting (18 – 60 ms), matrix: 48 x 48, FOV: 6 x 6 x 2 mm, axial slice. A full list of scan parameters for this experiment is shown in Appendix 2. An additional 42 direction (+ 6 images without diffusion weighting) DTI dataset was acquired for each nerve: Δ:

8 ms, δ: 3 ms, G: 0.6 T/m, b-value: 1600 s/mm^2. Other DTI acquisition parameters were: TR: 2000 ms, TE: 60 ms. The total scan duration for each sample was 6 hours, 48 minutes plus 1 hour 36 minutes for the DTI measures, total images acquired from each sample: 252. The SNR of images without diffusion weighting at the longest echo time used (60 ms) was 11.76:1.

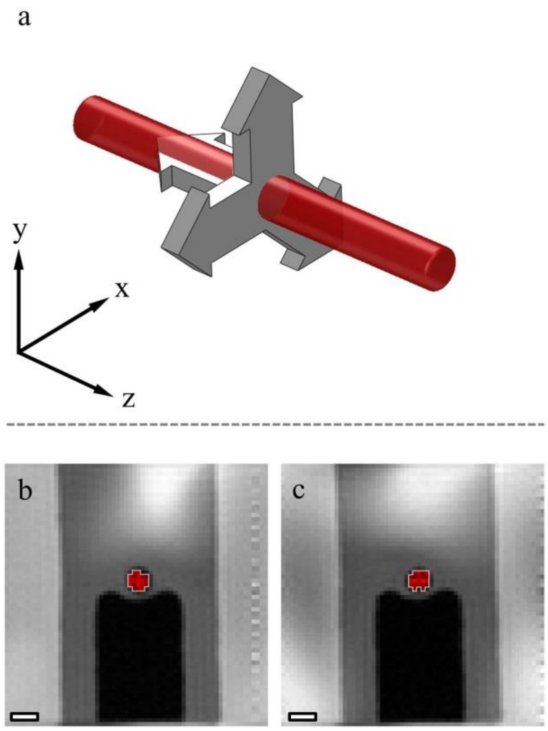

Figure 5.1.1: Experiment B Applied Gradient Directions and ROI Selections.

Showing, in panel a, the four gradient directions applied to each optic nerve (in red) during the multi-direction-multi-b-value dMRI dataset acquisitions (y: phase, x: read & z: slice). The lower panels show example images without diffusion weighting from fixed (b) and VIT (c) nerves with the regions of interest used overlaid in red with a white outline. Scale bars in panels b and c represent 1mm.

5.1.3 Signal Fitting

The open source Camino diffusion MRI tool kit [118] was used to fit diffusion tensors (A) and multi-compartment signal models (B) [53] to the dMRI data.

DTI data were fitted using a non-linear tensor model [124] & [119]. Diffusivity parallel to the nerve (AD), perpendicular to the nerve (RD) and fractional anisotropy (FA) were extracted from the fitted tensors. The significance of trends in AD, RD and FA in each experiment was calculated using linear regression. Statistical differences between the means of VIT and fixed experiments were calculated using the Student's t-test [125].

Figure 5.1.2 shows a graphical representation of the individual model fitting compartments used in experiment B. Table 5.1.2 shows a full list of the multi-compartment models fitted to the dMRI datasets; the naming conventions used in [53] were also used here. Each model is a combination of compartments of which there are three types: [1] intra-axonal (anisotropic restricted compartments), [2] extra axonal, (isotropic and anisotropic hindered compartments) and [3] other compartments of isotropic restriction. Volume fractions for these compartments are denoted f_1, f_2 and f_3 respectively in this work. A range of constraints is applied to parameters from the fitted model compartments. For a complete overview of parameter restrictions and detailed mathematical descriptions of the model compartments see [53].

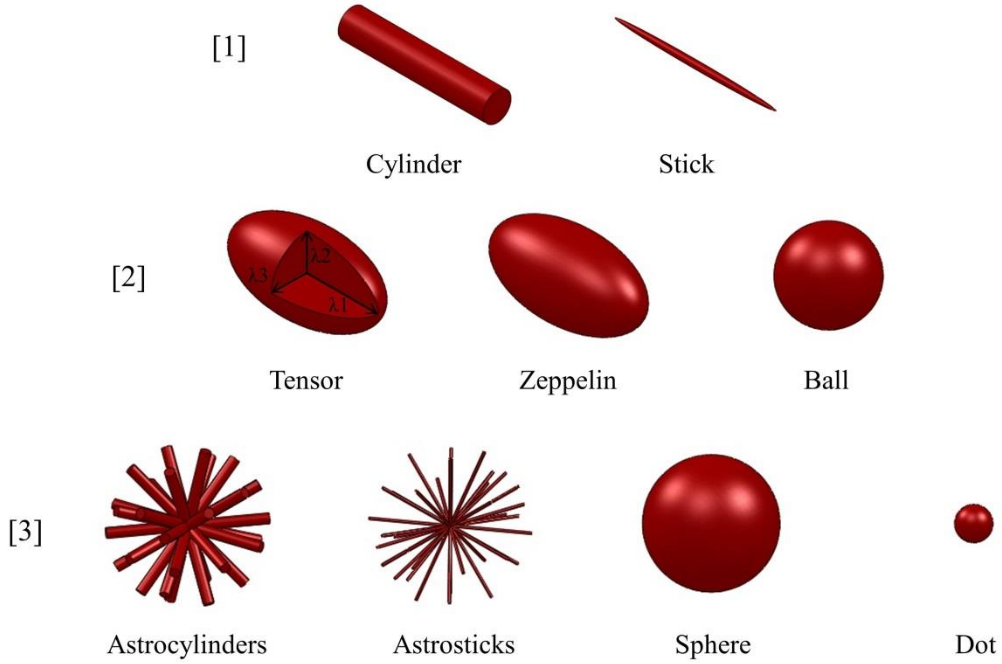

Figure 5.1.2: Graphical Representation of the Fitted Model Compartments.

Showing a graphical representation of the fitted model compartments. Each row is a different compartment type: Anisotropic restricted compartments [1], isotropic and anisotropic hindered compartments [2] and isotropic restricted compartments [3]. Volume fractions for each of the compartments [1], [2] and [3] are denoted f_1, f_2 and f_3 respectively in this work.

Multi-Compartment Models
TensorCylinderSphere (TCSP)
TensorCylinderAstrocylinders (TCAC)
TensorCylinderAstrosticks (TCAS)
TensorCylinderDot (TCD)
TensorStickAstrocylinders (TSAC)
TensorStickSphere (TSSP)
TensorStickAstrosticks (TSAS)
ZeppelinCylinderSphere (ZCSP)
TensorCylinder (TC)
TensorStickDot (TSD)
ZeppelinCylinderAstrosticks (ZCAS)
ZeppelinCylinderAstrocylinders (ZCAC)
ZeppelinStickAstrocylinders (ZSAC)
ZeppelinCylinderDot (ZCD)
ZeppelinStickSphere (ZSSP)
TensorStick (TS)
BallCylinderSphere (BCSP)
ZeppelinStickAstrosticks (ZSAS)
ZeppelinStickDot (ZSD)
ZeppelinCylinder (ZC)
BallCylinderAstrosticks (BCAS)
BallCylinderAstrocylinders (BCAC)
BiZeppelin (BZ)
BallStickAstrocylinders (BSAC)
BallStickSphere (BSSP)
BallCylinderDot (BCD)
Diffusion Tensor (DT)
BallStickAstrosticks (BSAS)
ZeppelinStick (ZS)
BallCylinder (BC)
BallStickDot (BSD)
BallStick (BS)

Table 5.1.2: List of the Multi-Compartment Signal Models.

Showing a list in order of most parameters to least, of the multi-compartment signal models fitted to the multi-direction-multi-b-value dMRI datasets from VIT and fixed optic nerves. Full names and acronyms are shown.

Camino fits each multi-compartment model to the data using a Levenberg–Marquardt algorithm [126] for minimising a chi-squared (χ^2) objective function. Various noise models are available, but here the offset Gaussian noise model [127] & [124] as employed by [53] was used. The fitting performance of complex models is highly sensitive to the given starting parameters. The multi-run procedure was used to select starting parameters as described in [53]. The parameter set that minimises the objective function from 1000 perturbations from the starting parameters was chosen for each model. Models were ranked using the Bayesian information criterion (BIC) [128], which rewards models that minimise the objective function while penalising those with more parameters;

$$BIC = -2\ln(L) + kln(n), \qquad [4.1.1]$$

where L is the likelihood of the estimated model, n is the number of measurements and k is the number of free model parameters to be estimated.

For all MR experiments, voxels were selected by thresholding a region of interest drawn on the nerve, voxels with FA > 0.4 and a principal eigenvector deviating no more than 2.5º from the scanner Z axis were selected (see Figure 5.1.1 for examples).

A significant learning process was needed to master the use of the multi-compartment models. A remote cluster-based 'super-computer' was used for the multi-run fitting.

5.2 Results

5.2.1 DTI (Experiment A)

Table 5.2.1 displays the average calculated FA, AD and RD from VIT and fixed samples (n = 3 & 3). FA in fixed samples was found to be significantly lower than that of VIT for all measurements. AD was observed to be higher in VIT compared with fixed nerves while RD was lower in VIT compared to fixed nerves. Dependencies of DTI indices (FA, AD and RD) on acquisition parameters were clear for both VIT and fixed tissue in experiments A1 and A2, i.e. a dependence on b-value whether varied by diffusion time or gradient strength. Moreover, the dependence was similar in both tissue types: FA increases with b-value, and both AD and RD decreased. Experiment A3 demonstrated no clear trends for fixed tissue or VIT.

Experiment A1

DTI indices		FA		AD		RD	
Tissue		VIT	Fixed	VIT	Fixed	VIT	Fixed
Step #	1	0.75	0.65	1395.94	1177.74	304.08	361.23
	2	0.78	0.69	1267.72	1050.93	243.37	283.61
	3	0.80	0.74	1036.43	862.24	180.07	195.05
Trend Statistics	slope	+	+	-	-	-	-
	P	<0.05	<0.05	<0.05	<0.05	<0.05	<0.05
	R^2	0.73	0.99	0.83	0.99	0.88	0.99

Experiment A2

DTI indices		FA		AD		RD	
Tissue		VIT	Fixed	VIT	Fixed	VIT	Fixed
Step #	1	0.77	0.65	1449.25	1171.65	307.28	356.34
	2	0.79	0.69	1307.32	1061.98	243.14	288.16
	3	0.82	0.73	1071.54	849.25	162.76	194.28
Trend Statistics	slope	+	+	-	-	-	-
	P	<0.05	<0.05	<0.05	<0.05	<0.05	<0.05
	R^2	0.81	0.97	0.74	0.98	0.61	0.90

Experiment A3

DTI indices		FA		AD		RD	
Tissue		VIT	Fixed	VIT	Fixed	VIT	Fixed
Step #	1	0.79	0.69	1307.32	1061.98	243.14	288.16
	2	0.80	0.69	1325.40	1037.24	237.50	293.26
	3	0.78	0.69	1256.92	1066.50	232.58	302.80
Average		0.79	0.69*	1296.55	1055.24*	237.74	294.74*
Trend Statistics	slope	N/A	N/A	N/A	N/A	N/A	N/A
	P	>0.05	>0.05	>0.05	>0.05	>0.05	>0.05
	R^2	0.09	0.32	0.03	0.05	0.22	0.05

Table 5.2.1: Data from Each Step of Experiments A1, A2 and A3.

Showing averaged calculated FA, AD and RD from DTI experiments on VIT and fixed samples (n = 3 & 3) and statistically significant trends across each experiment (linear regression: p-value (P) and coefficient of determination (R^2)). The direction of slop of any significant change is also indicated. AD and RD units are $\mu m^2/s$. *: Significant difference from mean of VIT ($P < 0.05$, Students t-test). Nb, The sample size here is only three; further samples would provide more statistical power to detect an effect. Nevertheless, with n = 3, clear trends are evident and thus this sample size is sufficient for the presented analysis. These statistics are presented, with these caveats borne in mind, for the reader's information.

5.2.2 Multi Direction Multi b-value dMRI (Experiment B)

Table 5.2.2 displays the BIC model ranking for both VIT and fixed nerves. In both VIT and fixed samples, BIC ranking of multi-compartment fitted models showed similar trends. To qualify, there is little to differentiate between the top ten ranking models (8 of the top 10 VIT models are in the top 10 fixed models) and similar models appear in similar positions throughout the ranking. Identical rankings are not expected but models should appear in similar positions if the water diffusion behaviours are comparable. Broadly, and in agreement with previous application of these models [53], three compartment models ranked highest. In both samples, models with a “Stick” compartment representing the intra axonal space outperformed their “Cylinder” counterparts. Although the fitting error is slightly lower for the “Cylinder” models, the BIC’s complexity term penalises them more because of the extra parameter. Similarly, “Zeppelin” models for the extra axonal hindered compartment outranked “Tensor”. Both also outrank “Ball” models, which do not have sufficient complexity to fit the data well. “Astrosticks” models ranked highest as descriptors of the isotropic restricted compartment. “Astrocylinders” and “Astrosticks” estimated higher volume fractions than both “Dot” and “Sphere” models and ranked higher. The diffusion tensor model ranks lowest.

Rank	VIT				Fixed			
	Model	BIC score	Objective function	Parameters	Model	BIC score	Objective function	Parameters
1	ZSAS	92.21	53.56	7	ZSAS	100.05	61.40	7
2	ZSD	92.69	54.04	7	TSAS	100.42	50.73	9
3	BZ	93.50	54.85	7	BSAS	100.83	67.70	6
4	ZCAS	97.65	53.47	8	ZSD	103.81	65.16	7
5	ZCAC	97.70	53.53	8	BZ	104.24	65.59	7
6	ZSAC	97.73	53.56	8	TSD	104.50	54.80	9
7	ZCD	97.99	53.82	8	ZCAS	104.76	60.59	8
8	ZS	98.04	59.39	6	ZCAC	104.98	60.81	8
9	ZSSP	98.21	54.04	8	ZS	105.09	71.96	6
10	TSAS	99.81	50.11	9	ZSAC	105.49	61.32	8
11	TSD	100.63	50.94	9	**TCAC**	**105.55**	**50.33**	**10**
12	TS	100.74	56.57	8	BCAS	105.59	66.94	7
13	BSAS	102.23	69.10	6	TS	105.59	61.42	8
14	ZC	103.03	58.86	7	BCAC	105.93	67.28	7
15	ZCSP	103.53	53.83	9	TSAC	105.93	50.72	10
16	**TCAC**	**104.94**	**49.73**	**10**	BSAC	106.34	67.69	7
17	TC	104.95	55.26	9	ZCD	107.58	63.40	8
18	TSAC	105.33	50.11	10	ZSSP	108.05	63.88	8
19	TCD	105.36	50.14	10	ZC	108.09	69.44	7
20	TSSP	106.04	50.82	10	TCD	108.25	53.03	10
21	TCAS	107.11	51.89	10	TC	108.57	58.88	9
22	BCAS	107.23	68.58	7	TSSP	108.83	53.62	10
23	BCAC	107.45	68.80	7	TCAS	111.75	56.54	10
24	BSAC	107.75	69.10	7	ZCSP	113.10	63.41	9
25	TCSP	110.89	50.16	11	TCSP	113.77	53.03	11
26	BSSP	117.56	78.91	7	BSSP	115.79	77.14	7
27	BS	118.04	90.44	5	BS	116.83	89.22	5
28	BC	121.41	88.28	6	BC	120.41	87.28	6
29	BSD	123.30	90.17	6	BSD	121.98	88.85	6
30	BCSP	124.04	79.87	8	BCSP	122.40	78.23	8
31	BCD	126.19	87.54	7	BCD	125.19	86.54	7
32	DT'	196.55	179.76	7	DT'	229.46	212.67	7

Table 5.2.2: BIC Ranked Multi-Compartment Models for VIT and Fixed Nerves.

Showing the BIC ranked multi-compartment models for VIT and fixed optic nerves and the number of parameters for each model. The model with the lowest objective function (“TensorCylinderAstrocylinders” - TCAC) is highlighted in bold.

Models with a “Tensor” for the extra axonal hindered compartment produced the lowest objective functions but were most heavily penalised by the BIC ranking. Parameter estimations from a selection of the best and worst fitting models are shown in Table 5.2.3. Volume fractions estimated by the best fitting models differed between VIT and fixed tissue. An increase in f_3 and a decrease in f_1 in the fixed sample can be observed in all of the top ten ranking models. Figure 5.2.1 shows the model fits to the data for both the best (“ZeppelinStickAstroSticks” - ZSAS) and worst fitting model (the Diffusion Tensor – DT).

Model	Rank	Tissue	Best Parameter Estimates										
			S_0	f_1	f_2	f_3	$d_{\|}$	$d_{\perp 1}$	$d_{\perp 2}$	θ	φ	R	α
ZSAS	1	VIT	0.99	0.60	0.22	0.18	2157	635	-	-0.04	0.11	-	-
	1	Fixed	0.98	0.51	0.20	0.29	1715	669	-	0.05	0.18	-	-
ZSD	2	VIT	0.99	0.57	0.35	0.07	2072	647	-	0.05	0.15	-	-
	4	Fixed	0.98	0.49	0.41	0.10	1496	663	-	-0.05	0.16	-	-
ZCAS	4	VIT	0.99	0.60	0.22	0.17	2143	602	-	0.05	0.12	1.29	-
	7	Fixed	0.98	0.52	0.20	0.28	1675	613	-	-0.05	0.18	1.75	-
TSAS	10	VIT	0.99	0.59	0.22	0.19	2200	771	347	0.04	0.12	-	-0.93
	2	Fixed	0.99	0.51	0.21	0.28	1681	1052	424	0.03	-0.06	-	0.07
BS	27	VIT	1.01	0.74	0.26	-	1699	-	-	0.12	0.19	-	-
	27	Fixed	0.99	0.67	0.33	-	1163	-	-	-0.12	0.49	-	-
DT	32	VIT	0.94	1.00	-	-	1606	67.2	61.9	0.02	0.23	-	2.58
	32	Fixed	0.91	1.00	-	-	1170	102	84.1	0.02	0.61	-	-1.04
TCAC	16	VIT	0.99	0.60	0.22	0.18	2167	750	305	0.04	-0.06	1.55	2.21
	11	Fixed	0.98	0.52	0.21	0.27	1637	966	397	0.03	0.16	1.49	3.14

Table 5.2.3: Fitted Parameters from a Selection of Models.

Showing the fitted parameters (compartment volume fractions, diffusivities, orientation parameters and radii estimates) from a selection of models: four of the highest and two of the lowest BIC ranked models from both VIT and fixed samples. Also shown are the parameter estimates from the model with the lowest objective function “TensorCylinderAstrocylinders” (TCAC) for comparison. The volume fractions for each compartment (1, 2 and 3) are denoted f_1, f_2 and f_3 respectively. The units for the diffusivities ($d_{|}$, $d_{\perp 1}$, $d_{\perp 2}$) are in $\mu m^2/s$, for the radii (R) μm and the angles (θ, φ, α) are in radians (see [53]).

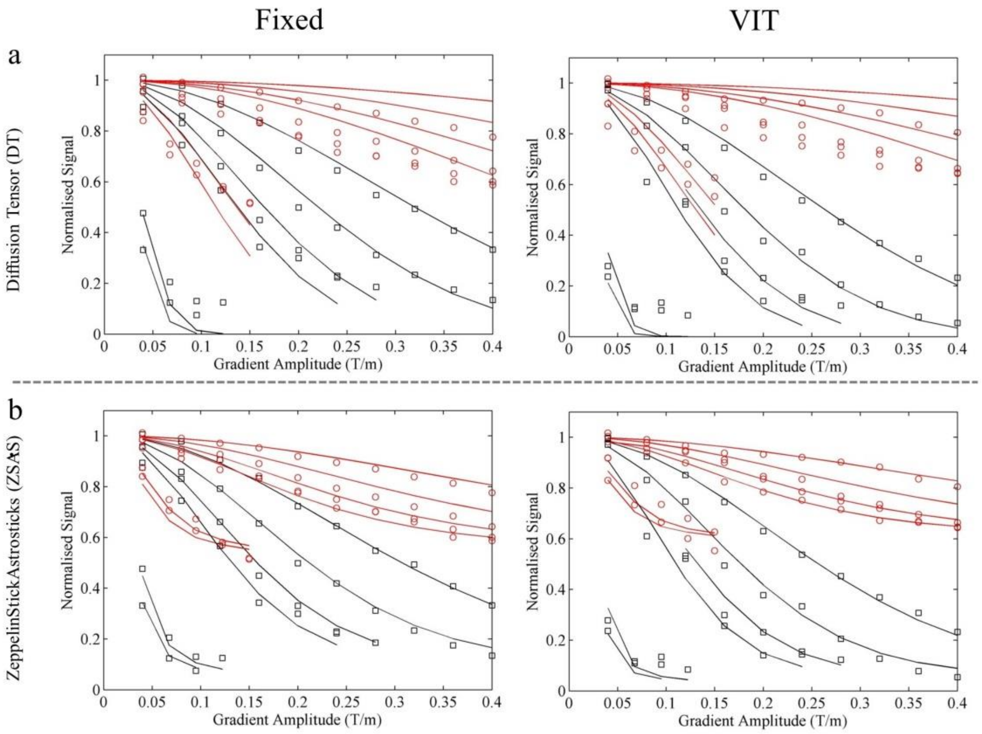

Figure 5.2.1: Model Fits to the Data from Experiment B.

Showing model fits to the data for the worst (Diffusion tensor – DT) and best (“ZeppelinStickAstrosticks” – ZSAS) BIC ranking models. Red circles represent the average of the 3 perpendicular measures while black squares represent the parallel measures. Red and black lines represent the model fits to the respective directions. Red lines indicate perpendicular diffusion gradient directions while black represent parallel. The degree of attenuation of each set (final line height) is dictated by the diffusion time (and thus the final b-value) for each set (see methods 5.1.2 and 7.10).

5.3 Discussion

5.3.1 DTI (Experiment A)

DTI data from experiment A allows the quantification and comparison of DTI indices and their dependencies on acquisition parameters. Similarities and differences between the tissues were revealed.

A negative AD and RD dependence on increasing G in both samples was shown in experiment A1 while FA increased. The dMRI signal is the sum of weighted signal from water pools within the tissue. As b-value increases, the faster diffusing pools attenuate more with respect to the slower i.e. the signal from the more hindered and restricted water becomes relatively prominent. The underlying tissue microstructure leads to anisotropic water diffusion patterns, so calculated FA therefore also showed dependence on changes to G. These effects have been previously reported for *in vivo* tissue [129,130].

Experiment A2 demonstrated a negative AD and RD dependence on increasing Δ & δ (and thus increasing diffusion weighting) in both tissues while FA showed a positive dependence. This effect is similar to that seen in Experiment A1, but the b-value in Experiment A2 is changed by increasing diffusion time rather than gradient strength. Increasing b-values using longer Δ, sensitized the experiment more to slower diffusing or restricted water components.

In contrast to experiments A1 and A2, experiment A3 demonstrated no FA, AD or RD dependence on Δ & δ at constant b-values in either tissue type. These data agree with previous work [131,132], which found that water diffusion coefficients calculated from data with constant b-values at these diffusion time scales, are not sensitive to the diffusion gradient durations and separations applied. Comparable values were observed when comparing DTI indices calculated from experiments A1 and A2 at similar b-values, which further demonstrates the conclusion of experiment A3.

Assuming water diffusion coefficient scaling with temperature as described by Holz et al [133], the water diffusion coefficients measured in experiment A are consistent with previous work on viable bovine optic nerves [56] and fixed rat white matter [53] at room temperature.

The average axon diameter within the optic nerve is considerably less than 7 μm [122]. The root mean square displacements in experiment A3, assuming diffusivity of ~3000 $\mu m^2\ s^{-1}$ [133,134] (i.e. that for free water diffusion in pure water at 37ºC) and using Einstein's equations [135], are 7, 10 and 13 μm (Δ = 10, 20 & 30 ms). With these DTI experiments we are therefore observing, at least partially, not free but restricted water diffusion, within the optic nerve tissue.

In summary, VIT and fixed optic nerve DTI indices showed similar trends in dependence on acquisition parameters. This similarity suggests that the multiple water populations with different diffusivities that were present in VIT are maintained post fixation.

Conversely, averaged absolute values of AD, RD and FA from VIT and fixed tissue differed significantly from one another in all three experiments despite conditions being as similar as possible (e.g. temperatures, orientations and sample sources). When compared with VIT, RD was higher in fixed tissue while AD and FA were lower. These DTI experiments suggest that while fixed tissue can be a useful model for *in vivo* tissue, insofar as the broad trends of indicies with acquisition parameters is similar in fixed and VIT, quantitative DTI measures will not translate directly from fixed tissue to VIT and beyond to *in vivo,* and should be viewed with caution.

5.3.2 Compartment Models

BIC rankings selected the same top model and similar top ten models in fixed tissue and VIT while parameter estimates differed; this implies that while the broad tissue structure is maintained after fixation, the water populations differ in behaviour.

BIC ranking placed "Zeppelin" models higher than lower objective function "Tensor" models as hindered compartment descriptors. The "Tensor" models' extra parameters ($d_{\perp 2}$ & α) are potentially sensitive to underlying water population features which the cylindrically symmetric "Zeppelin" models are less able to capture. However, these extra degrees of freedom did not increase the quality of fit to a point where this advantage outweighed BIC penalisation. The ranking of models shown here is similar to the Panagiotaki experiments [53] in some respects e.g. three compartment models rank highest and "Zeppelin" and "Tensor" models outperform "Ball". However there are marked differences, e.g. in contrast to here, their "Sphere" and "Dot" models outperform "AstroStick" and "AstroCylinder" and volume fraction patterns are significantly different. The rat corpus callosum has a similar but not identical structure to the rat optic nerve (see [55]) with a range of axon radii distributed in distinct functional regions. For example, the mid-body region of the corpus callosum contains larger and more loosely packed axons that those found in the optic nerve. These structural differences along with the differing temperatures could account for the differing ranking and volume fraction estimates.

The highest ranking models fitted the data from both samples closely (see Figure 5.2.1). These models, while only providing a gross description of the behaviour of water populations in biological tissue, captured broad trends in the data.

The models used in this work were designed to describe the behaviour of the bulk water population within the tissue. Neuronal tissue is highly complex, so the comparative simplicity of compartment models means that certain features and patterns of the bulk water diffusion in biological tissue cannot be characterised fully. Probing very short (e.g. using oscillating gradient spin-echo [136]) and long diffusion times (e.g. using stimulated echo acquisition mode [137]) or including more complex features such as exchange and further compartments may reveal differences and potentially greater departures between fixed and VIT which are obscured in this work. However, acquiring at short and long diffusion times presents practical obstacles (such as gradient rise time, eddy currents and SNR reduction) and more complex models can be difficult to fit [57].

The parameters of the best fitting models were sensitive to differences between fixed and viable tissue, e.g. differences in diffusivity both perpendicular and parallel to the nerve axis ($d_{\perp 1/2}$ & $d_{|}$). Diffusivity parameter estimates from the highest ranking models were analogous with DTI detected differences in RD and AD between fixed and viable tissue: $d_{\perp 1/2}$ is higher in fixed tissue while $d_{|}$ is lower.

Overall, diffusivity estimates differ from those estimated by DTI measures; the multi-b-value dMRI data used here probes parameter space in more detail with more numerous measurements than the 30 direction (single shell) acquisition used for the DTI experiments. In addition multi-compartment models have more degrees of freedom and are better able to fit dMRI data than the relatively limited and constrained DT model. The multi-compartment models may be better able to separate different effects in different populations. For example, some of the differences in signal could be explained by differences in volume fraction parameters, whereas the DT model has to explain the ensemble effects by changes in diffusivity parameters alone. This difference in ability to describe dMRI data can be seen clearly in the ranking of the DT model (last for both samples) in comparison with more complex models (see Table 4).

5.3.3 Tissue Structure and Compartment Models

While it appears that the best fitting models are sensitive to microstructural differences between fixed and white matter, the relationships between parameter estimates and specific structural features remains somewhat unclear. The water diffusion signal originates from the pool of diffusing spins throughout the tissue, disentangling the contributions from glial cells, neurons, myelin and the numerous cellular micro-machinery is a non-trivial problem. Because of this it is difficult to predict exactly how the models will react to different tissues. This does not preclude the use of such models to compare and contrast samples as they are still sensitive to microstructural changes. Artificial tissue constructs (e.g. [138]) could be used to make some headway in correlating model parameters directly to microstructure and selecting the best model to use for certain structures.

5.3.4 Signal to Noise Ratio

The effects of SNR on dMRI data are non-trivial and the literature contains detailed investigation of the effects of low SNR on DTI measurements [124,139,140]. Over-estimation of FA in highly isotropic samples (e.g. CSF) can occur, because of noise induced differences in the principal eigenvectors, which lead to the calculation of a falsely elevated FA. Conversely in highly anisotropic samples, low SNR can lead to underestimation of MD in the principal eigenvector direction as the signal cannot attenuate fully before reaching the noise floor, which has the effect of artificially reducing FA. In the DTI experiments described here, SNR is comparable in VIT and fixed samples, so the bias induced by low SNR measures (especially relevant in high b-value parallel direction measures) is similar in both samples and does not affect the comparison.

The effects of SNR on more complex models is not as clear cut, as both the fitting method and noise model can affect the fitting outcome. The fitting procedure used in this work accounts for the Rician noise bias by using an offset Gaussian noise model, which adds an expected signal offset to the measured signal [124,127]. Fitting to data in the noise floor was avoided by preventing acquisition of low SNR data points. Generally noisy data will obscure differences between similarly attenuating signals which can, for example, lead to crossover of compartmentalisation and/or less sensitivity to the size of the restricted compartment.

5.3.5 Compartment Relaxation

In this work, the effects of T_2 relaxation were avoided by normalising each measurement by a separate measurement without diffusion weighting with the same echo time. However, this step does not remove relaxation effects entirely, as distinct T_2 components may exist in white matter, see for example [141]. Very short T_2 components ~13ms, e.g. from myelin water [142] can reasonably be ignored at the longer echo times used in experiments A and B. However, this is not the case for some of the data points acquired with short echo times. In addition, T_2 in the intra and extra axonal spaces may differ and the tissue fixation process may alter them independently. The primary effect of differing T_2 is that estimated compartment volume fractions in our models become T_2-weighted, which may contribute to any differences observed. While the models in experiment B adapt naturally to include compartmental T_2 values [143], fitting the extra parameter becomes unstable because of the larger number of exponential components. T_2s calculated from the measurements without diffusion weighting taken in experiment B were similar in viable and fixed nerves (34.75 and 35.02 ms respectively) and appear mono exponential, so it can reasonably be assumed that the compartment T_2s are similar in the two samples. This similarity agrees with previous work comparing fixed and fresh brain slices at room temperature [63].

5.3.6 Fixation Effects in White Matter

In order to explain how formaldehyde fixation may lead to the observed differences in water diffusion behaviours (e.g. changes in RD and AD), a brief background on the chemical action of formaldehyde is required. Formaldehyde (IUPAC name; methanal, CH_2O) is a gas which when dissolved in water is hydrated (in a rapid equilibrium) to form methanediol (CH_4O_2) to more than 99.5% [144]. The two species, while chemically distinguishable, are in such rapid dynamic equilibrium that both molecules are considered to constitute ‘free formaldehyde’ [145].

Aqueous formaldehyde can polymerise and reacts with free amine groups (-NH_2) on proteins. Initially, highly reactive methylol intermediates are formed which can create methylene crosslinks between proteins, forming a gel-like matrix of proteins which can support and trap other molecules [146]. In lipids, formaldehyde can also react with the double bonds of unsaturated fatty acids causing their interconnection [147].

This cross-linking behaviour likely contributes to the changes in water diffusion patterns observed in this work. Cross-links between membrane proteins and nearby proteins in the cytosol as well as lipids may disrupt the structure of the membrane, increasing the potential for penetration of water molecules. In addition, fixation disrupts the electrochemical gradient across the cell membrane, because ATPases which catalyse the decomposition of adenosine triphosphate (ATP) to produce energy are disabled by formaldehyde. Without ATP hydrolysis (and an intact membrane) cells can no longer power the sodium-potassium transmembrane pump which maintains concentration and electrical gradients across the membrane [76]. Disruption of membrane ion pumps and exchangers will cause changes in ion fluxes which can lead to swelling of glia and neurones [148]. This swelling could contribute to the increased RD observed in fixed optic nerves in experiment A.

Experiment A demonstrates a reduction in AD caused by the fixation process. Axons are the most anisotropic structure in the nerve bundle, so an increase in restriction along their length could be causing this effect. For example, swollen glial cells could lead to the collapse or reduction in cross section of axons in certain areas thus reducing AD.

Differences in parameter estimates from experiment B (e.g. increases in f_3 and decreases in f_1 in the fixed sample), further suggest that fixation causes complex dMRI-detectable microstructural changes within the tissue which re-distribute and alter the behaviour of water populations. A reasonable explanation is that fixation increases the fraction of water in a restricted state (f_3) due to the chemical cross linking described above. The effects could be further disentangled in future work by application of more complex models perhaps including water exchange.

While formaldehyde fixation undoubtedly directly alters the structure of the tissue, the non-immediacy of fixation could itself lead to structural changes even before chemical fixation can occur [149]. Fixative must diffuse into the tissue, and even in such small samples as rat optic nerves there is a significant time during which the sample is essentially starved of oxygen and will begin to degrade. Quantification of any changes induced by chemical fixation is hindered by the necessity to fix and dehydrate samples before electron micrographs can be taken. A further complication is the difficulty of generating truly 3D EM images of the tissue. A recent technical development, 3D serial block face scanning electron microscopy (SEM) [150] deals with this issue, but this technology is relatively new and was not commonly available at the time of writing. Serial block face SEM cannot be performed on VIT samples anyway, so absolute microscopic quantification of fixation effects remains out of reach.

White matter generally performs a similar role between species and CNS regions, but there are significant variations in tract curvature, neuron density and myelin thickness e.g. [151]. There are also significant variations in white matter structure between the sexes and with age in humans [152,153]. Given the problems in assigning specific compartments to specific microstructure, it is difficult to predict how the multi-compartment models would react to these structural differences. The changes in FA and diffusivity detected between fixed and VIT white matter could also differ between tissue and fixation regimes, However, it is the opinion of the author that these results provide a sensible guideline for likely changes to mammalian white matter during fixation, particularly changes in FA and AD which are the most pronounced.

5.3.7 Conclusion

Fixed tissue is commonly used as a model for dMRI sequence development and testing. This is due, in part, to its apparent structural similarity to *in vivo* tissue: a complexity which is unavailable in manufactured phantoms. This work, for the first time, compares viable and fixed white matter in identical conditions at physiological temperature. These dMRI data demonstrate that while fixed tissue is broadly a reasonable analogue for VIT (similar models explain the data best and DTI indices have similar dependence on acquisition parameters), there are significant underlying differences (differing parameter estimates) which demonstrate that formaldehyde fixation induces changes in the microstructural water diffusion environment.

Fixed tissue is useful for broadly identifying which models are appropriate for future diagnostic techniques, but precise choice of optimal acquisition parameters depends on the values of tissue water diffusion parameters. Experiment design techniques such as [57] cannot be conducted entirely using fixed tissue so researchers need to consider the changes in parameter values. Further experiments on viable or *in vivo* tissue will therefore still be required.

It is the opinion of the author that all pre-clinical water diffusion MRI work should be validated in some kind of viable tissue device before moving to animal models. This would prepare researchers for some of the problems that may be encountered in the transition from fixed to *in vivo* tissues.

6.0 Perturbation and Functional dMRI Study

The previous section described the application of the stable VIT chamber to investigate the dMRI detectable differences between viable and fixed white matter. With the success of that application, a more ambitious investigation into functional diffusion MRI in isolated tissue was conducted.

This section describes preliminary experiments aiming to detect a functional diffusion MRI effect in isolated white matter. In order to determine the feasibility of detecting small structural changes with dMRI, a series of chemical perturbation experiments using potassium ions to induce depolarisation and glial swelling in isolated optic nerves, was conducted (see section 2.8.2). After this initial testing proved successful, the VIT chamber was adapted to allow in MRI electrical stimulation and recording of action potentials from the nerves (creating an EP-MRI chamber). This system was used in preliminary experiments, to probe for a functional diffusion MRI response at physiological temperatures.

The primary motivation for this work was to determine if a dfMRI effect could be detected in the simplified system the chamber provides. Previous work has suggested that dMRI can be sensitive to functional activation in neural tissue [106,109,111]. Physical changes in water populations within the tissue during stimulation [96] may lead to water diffusion changes during activation (see sections 2.8.2 & 2.9). The chamber provides an ideal model system to probe for and investigate a true structural dfMRI effect as the confounding factors of blood-flow and animal movement are removed.

6.1 Methods

Rat optic nerves used in this work were extracted from Sprague Dawley rats (250-300 g) using the previously described methods (section 4.1.3) and maintained in the chambers at 37ºC for the duration of all the experiments described below. A total of 10 nerves from individual rats were used to produce the data show below. Four nerves were used for the potassium ion experiments, two for each of the fdMRI experiments and 1 each for the stimulus response experiment and the MRI EP artefact investigation experiment. The aCSF used was the same as that described in section 4.1.2 unless stated (e.g. in the potassium ion perturbation experiments). The aCSF delivery, heating and gassing set-up was as described in sections 4.1.1 and 3.2. All MR measurements were conducted with the 9.4 T MRI scanner described above (section 4.1.2) equipped with 1 T/m imaging gradients and a 33 mm diameter RF birdcage volume coil (RAPID Biomedical GmbH, Rimpar Germany).

6.1.1 Potassium Ion Experiments

In order to determine the feasibility of detecting small structural changes, such as those caused by electrical activation in the rat optic nerve, a series of potassium ion induced ECS size alteration experiments was conducted on optic nerves in the chamber. dMRI measurements were taken from optic nerves and used to calculate the ADC prior to and after the application of potassium ion doped aCSF mixture (1 nerve for each treatment: a total of 4).

6.1.1.1 Perturbation Solutions

The standard control aCSF mixture used in these experiments contained (in mM): NaCl (120); KCl (2); $CaCl_2$ (2); $NaHCO_3$ (26); $MgSO_4$ (1.19); KH_2PO_4 (1.18); D-glucose (11); as in [40] and in the above sections.

Three differing levels of excess potassium chloride (KCl) were added to this standard aCSF mixture, the appropriate amount of sodium chloride (NaCl) being removed to maintain the solutions osmolality. A high concentration as used in previous dMRI work on isolated rat optic nerves [67], a low concentration based on the detected potassium ion concentration increases during activity [99,101] and a mid-level concentration were prepared as follows:

- Low: 14 mM excess potassium ions: +1.05 g/L KCl | – 0.82 g/L NaCl
- Medium: 27 mM excess potassium ions: +2.01 g/L KCl | – 1.58 g/L NaCl
- High: 40 mM excess potassium ions: +2.98 g/L KCl | – 2.34 g/L NaCl

6.1.1.2 Preparation and Perturbation Protocol

For each step in experiment two, 1 litre of each aCSF mixture was prepared; a standard control solution and the doped solution. Both were gassed in the same manner with Carbogen (95% oxygen and 5% carbon dioxide) and heated on two identical hot plates (C-MAG HS-7, IKA, Staufen, Baden-Württemberg, Germany), see Figure 6.1.1.

Figure 6.1.1: Potassium Ion Doped and Control aCSF Set-up for Pumping to the Chamber.

Showing the equipment set-up used for the potassium ion perturbation experiments on the bench in the MRI preparation room.

The optic nerves were prepared as described in section 4.1.3 and placed into the chamber for dMRI measures in the control aCSF. The solutions were then switched using a pass-through syphon to prevent bubbles entering the system during switching. The time required to replace the bath solution was 2.5 minutes and test solutions were pumped into the chamber for 20 minutes before starting test dMRI measurements. Because of the time required to set-up the experiment and the long duration of each dMRI measurement set, separate nerves were used for dMRI measurements in the parallel and perpendicular directions. A further sham solution switch experiment was also conducted: the control aCSF was switched with a second batch of control aCSF.

6.1.1.3 dMRI Protocol and Analysis

In order to be consistent with the EP-MRI experiments described below (see 6.1.3.1); a 33 mm diameter RF birdcage volume coil was used for these MR experiments. The chamber loading mechanism was the same as that used for the EP-MRI experiments as described in section 6.1.3.1.

dMRI measures were taken with the diffusion gradients orientated parallel and perpendicular to the primary direction of the optic nerves. Diffusion gradient strengths were incremented from 0.032 to 0.32 T/m in nine steps of 0.032 T/m. Other diffusion parameters were Δ = 18 ms & δ = 5 ms, the b-values thus incremented from 0 to 2920 s/mm^2. One image without diffusion weighting was acquired for normalisation. A diffusion weighted fast spin echo sequence (dw-fSE) was used with an echo train length of 8; initial echo time was 27 ms with following echo spacing of 27 ms. Other imaging parameters were: TR: 1000 ms, matrix: 64 x 64, FOV: 6 x 6 x 2 mm, slice orientation was axial and 20 averages were taken at each measurement point. Total scan duration for each condition was 29 minutes, 30 seconds.

ROI selections were drawn for each nerve using the selections from images without diffusion weighting, which comprised ~20 voxels in each nerve. The ADCs for each condition in both the parallel and perpendicular directions were calculated using the open source Camino diffusion MRI tool kit [118]. ADC calculations were based on equation 2.3.5 shown above.

6.1.2 EP-MRI Chamber

The chamber design used in sections 3.0, 4.0 & 5.0 above was adapted to allow simultaneous stimulation and recording of action potentials in the nerve within a high field horizontal bore MRI scanner.

6.1.2.1 Electrophysiology Electrodes

Suction electrode stimulation and recording was chosen for the new design due to its inherent stability and resistance to agitation. Suction electrode recording is commonly used in peripheral nerve EP studies and has been investigated in great detail in the rat optic nerve [154]. Figure 6.1.2 shows a diagrammatic representation of suction electrodes connected to the nerve. The glass tubes of the electrodes were made from 1.5 mm outer diameter by 0.86 mm inner diameter borosilicate glass capillaries. The ends of the capillaries were heated using a Narishige PB-7 electrode puller (Narishige, Minami Karasuyama, Setagaya, Tokyo, Japan) to create slight constrictions just inside the end which contacts the nerve. A glass microelectrode holder (Axon instruments Inc. – now Molecular Devices Sunnyvale, California, U.S.A) was used for both suction electrode capillaries with the suction port connected to a length of 1 mm diameter tubing, a three way T-joint valve and a 1 ml syringe. In standard EP experiments, metal wires are used to deliver and record electrical signals. In the EP-MRI chamber, thin 0.28 mm carbon rods (Easy Composites Ltd, Longton, Staffordshire, U.K) were used in place of metal wires to prevent MRI artefacts arising from susceptibility effects [114]. A slightly thicker 0.5 mm rod was used for the reference electrode. Gold micro-banana connectors were connected to the ends of the electrodes using a conductive two-part silver epoxy resin (Chemtronics, Kennesaw, Georgia, U.S.A).

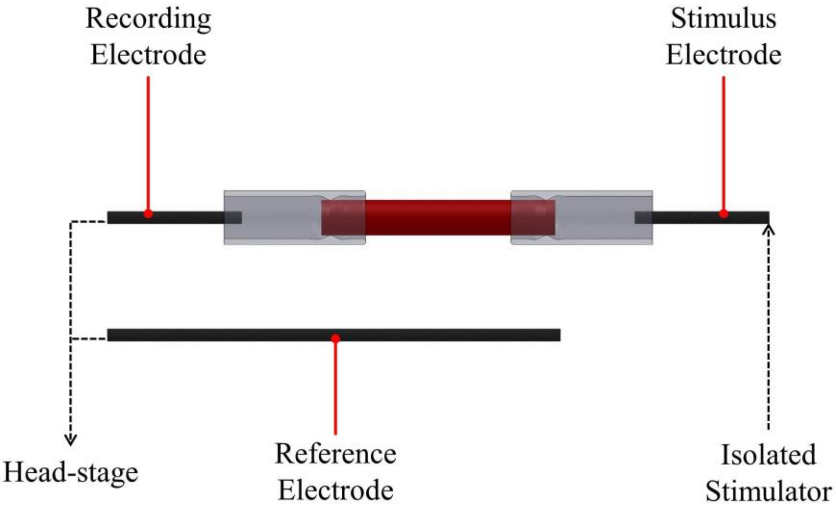

Figure 6.1.2: Suction Electrode and Optic Nerve.

Showing a diagram of the optic nerve (in red) with a glass suction electrode in place at either end. The head-stage is connected to the recording and reference carbon electrodes while the isolated stimulator is connected to the stimulus electrode.

6.1.2.2 EP-MRI Chamber Design Features

The EP-MRI chamber shown in Figure 6.1.3 was designed to allow the glass suction electrodes (Figure 6.1.2) to pierce the chambers' central bath and contact either end of the nerve. The temperature probe insert point was moved 4 mm to the right to allow space for the recording electrode, the outflow port was moved 4 mm to the left. The positioning/tubing support bar was adapted to include support for the recording electrode and an extra path was made in the chambers side to hold the wire leading to the stimulus electrode. Two extra holes were included to insert thin nylon screws which clamp the electrodes in place once they have been positioned on the ends of the optic nerve. An extra hole was built in to the rear of the chamber to support the plastic tubing providing negative pressure to the microelectrode holder; this prevented the tubing becoming tangled during MRI loading. In order to seal the central bath and prevent leaks, two silicon O-rings (Lynx Heli Innovations, Lake Como, Italy) were used for each suction electrode, one near the outer wall and a second near the inner bath wall. Sloping edges were added to the central bath to increase visibility during nerve loading. The bath depth was also decreased for ease of access. Other than these changes, the basic EP-MRI chamber layout remained identical to the chambers used in sections 3.0 - 5.0.

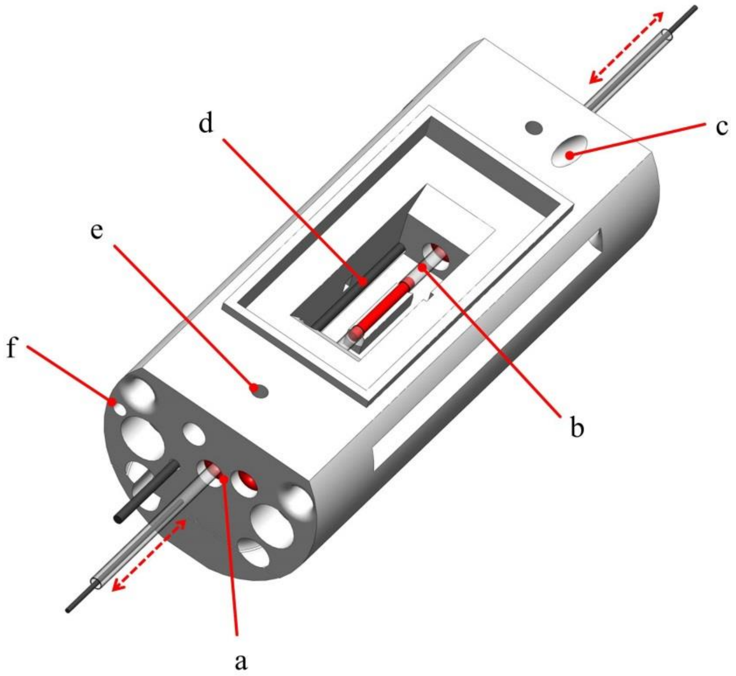

Figure 6.1.3: The EP-MRI Chamber.

Showing the EP-MRI chamber with the two glass suction electrodes piercing into the central bath and attached to the optic nerve (red cylinder). Various adaptations to the previous chamber designs are indicated. (a) Silicone O-ring, (b) suction electrode in central bath, (c) guide hole for suction tubing, (d) reference electrode, (e) threaded path for nylon screw to secure suction electrode and (f) path for stimulus electrode wire.

6.1.2.3 Initial Testing

Bench top experiments were initially conducted with the new suction electrodes using the same electrophysiology equipment described in section 4.1.5 with the stimulator replaced with a DS2 optically isolated stimulation box (Digitimer, Welwyn Garden City, Hertfordshire, U.K). During bench-top experiments the chamber was also tested for water tightness and to determine if the new adaptations had altered the flow characteristics or temperature maintenance ability of the previous design. A Stemi SV-11 microscope (Zeiss, Oberkochen, Baden-Württemberg, Germany) was used to position the nerve correctly in the suction electrodes. A stimulus response curve was measured from a single nerve;

stimulus pulses delivered from 5 V to 60 V at 50 Hz, stimulus pulses lasted 0.02ms each.

6.1.3 dfMRI Setup and Experiments

This section describes the setup and testing of the EP-MRI chamber for dfMRI experiments and the two preliminary dfMRI experiments conducted using the system.

6.1.3.1 EP-MRI Loading System and Adaptations

Due to the more delicate nature of the EP-MRI setup compared with previous chamber arrangements, a loading system was required. For previous work the nerve was clamped in place and the chamber was loaded by hand into the 26mm volume coil which was itself then slid into the magnet. Manual loading and coil sliding was attempted with the EP-MRI chamber and lead to various failures caused by human error. To prevent these problems a standard mouse cradle was used to load the EP-MRI chamber smoothly and accurately into the coil within the magnet. The size of the cradle prevented use of the 26mm volume coil and so a 35mm diameter RF birdcage volume was used for all EP-MRI experiments.

The EP MRI equipment used for the dfMRI experiments needed to be mobile so it could be moved from the EP lab to the scanner preparation area; a one metre wheeled rack cabinet was used to mount the equipment and the PC. Figure 6.1.4 shows the EP-MRI equipment setup in the MRI scanner prep room. The HS-2A head-stage used for recording action potentials from the optic nerve performs best when placed as close as possible to the preparation (to prevent signal attenuation in long wires). For the EP-MRI experiments the head-stage therefore had to be within the 5 Gauss line of the main magnetic field and so needed to be magnet compatible. The case of the head-stage is aluminium but contains six small ferromagnetic screws; these were replaced with nylon versions (Farnell UK Limited, Leeds, West Yorkshire, England). This greatly reduced the magnetic potential of the device and allowed safe positioning (with a Velcro strip to secure) within 70cm of the bore. The cable from the Axoclamp-2B microelectrode amplifier to the HS-2A head-stage needed to be extended by 1.5 metres to reach into the magnet room; shielded 8 core flex was spliced and soldered into place at the Axoclamp end of the cable. Preliminary EP recordings of action potentials stimulated in the scanner bore were made on a single nerve; a high duty cycle dMRI sequence was run during the recording to test for MRI induced EP artefacts.

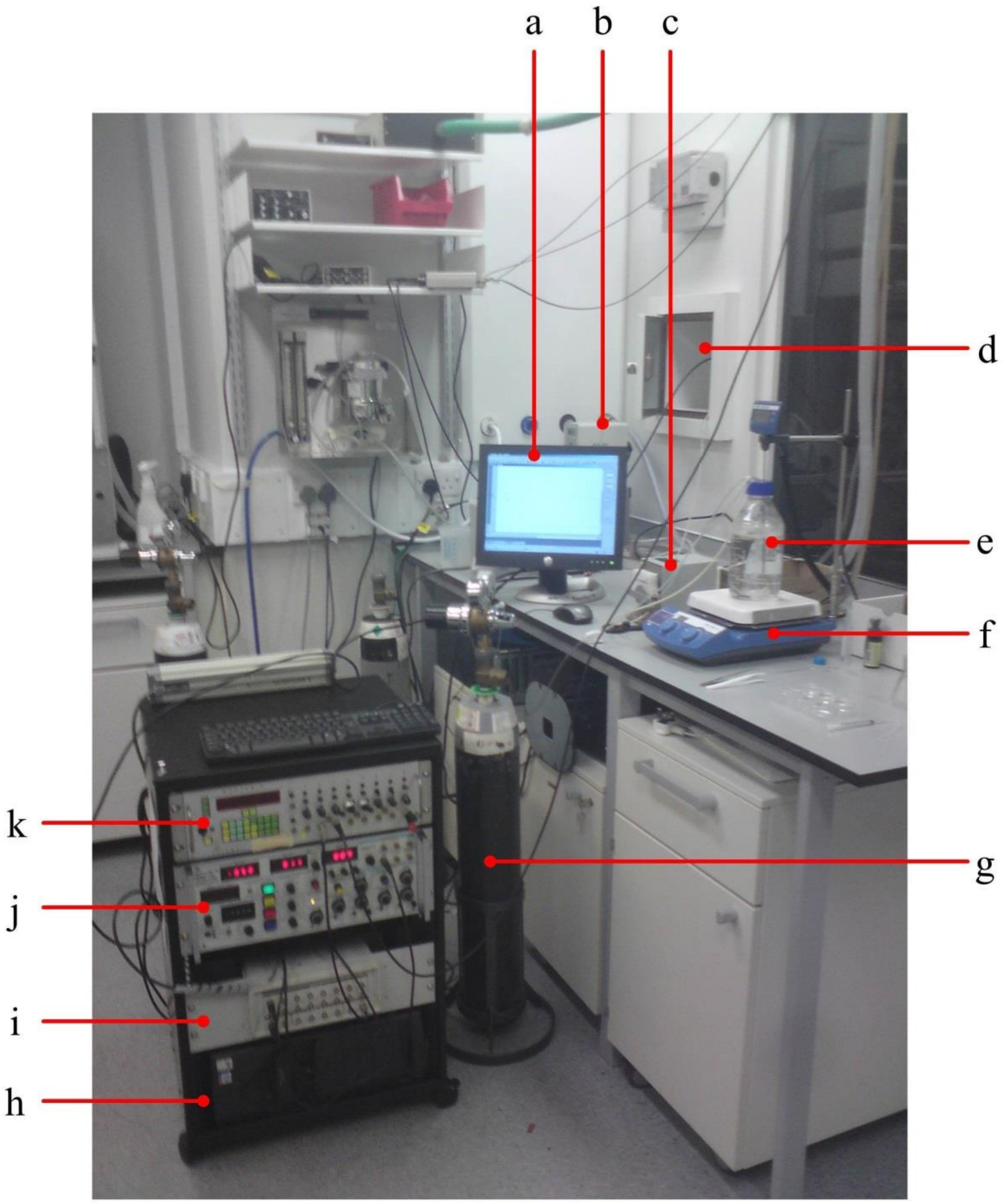

Figure 6.1.4: Setup of Equipment for the EP-MRI Chamber.

Showing the electrophysiology stimulus timing and recording equipment along with the chamber support equipment set-up in the MRI scanners prep area. (a) monitor displaying recorded compound action potentials from EP rig, (b) Hot water pump for chamber temperature maintenance, (c) peristaltic pump for aCSF delivery, (d) window into scanner room with EP recording cable and aCSF delivery and recovery tubes passing through , (e) aCSF on (f) temperature controlled stirrer being gassed with (g) carbogen gas (h) PC work station with pClamp software, (i) Digidata 1322A signal digitiser, (j) Axoclamp-2B microelectrode amplifier and (k) Master-8 pulse stimulator.

6.1.3.2 Data Analysis in dfMRI Experiments

In both dfMRI experiments described below, ROI selections were drawn for each nerve using the images without diffusion weighting, and the selections comprised ~20 voxels in each nerve. ADC for on and off conditions in both the parallel and perpendicular directions was calculated using the open source Camino diffusion MRI tool kit [118]. ADC calculations are based on equation 2.3.3 shown above.

6.1.3.3 dfMRI Experiment 1

dfMRI experiment 1 aimed to replicate, in the EP-MRI chamber, a dMRI experiment similar to that used in [111] where the authors suggested that a purely dfMRI effect can be detected *in vivo*.

dMRI measures were taken during on and off stimulus conditions with the diffusion gradients orientated parallel (a) and perpendicular (b) to the primary direction of the optic nerves. Different nerves were used for each diffusion gradient direction experiment; a total of two. Parallel direction (a) diffusion gradient strengths were 0.16 T/m for the low and 0.6 T/m for the high b-value measurements needed to calculate the ADC. Perpendicular direction (b) diffusion gradient strengths were 0.6 T/m for the low and 0.27 T/m for the high measurements. Other diffusion parameters were $\Delta = 18$ ms & $\delta = 5$ ms. The high and low b-values in the parallel experiment (a) were therefore 105 & 748 s/mm^2 and 105 and 2130 s/mm^2 in the perpendicular experiment (b). To improve SNR, a dw-fSE sequence was used with an echo train length of eight; the initial echo time was 27 ms with following echo spacing’s of 27 ms. Other imaging parameters were: TR: 1000 ms, matrix: 64 x 64, FOV: 6 x 6 x 2 mm, slice orientation was axial and two repeats of 24 averages were taken for each measurement. The scan duration for each measurement was 6 minutes, 34 seconds. To acquire a high and low b-value ADC image set (in either the ‘on’ or ‘off’ condition) therefore took 12 minutes and 8 seconds, comparable to the 12 minute, 48 second acquisition used in [111].

An ‘off/on/off’ paradigm was used in [111], but in this experiment the ‘off/on/off’ paradigm was extended to: ‘on/off/on/off’ to balance the weighting of noise to the results. Stimulus was delivered at 50 Hz for the duration of the on measurements; stimulus pulses were 40 V and lasted 0.02ms each. Total experiment time for each nerve was 48 minutes, 32 seconds (4 blocks of 12 minutes and 8 seconds).

Tetrodotoxin (TTX) is a marine neurotoxin which blocks action potentials in nerve cells by binding to their voltage-gated sodium channels [155]. After the activation experiment, TTX was added to the aCSF solution. The TTX-aCSF solution (4.61 nM TTX) was then pumped to the chamber for 10 minutes to block the sodium channels of the optic nerve. Action potentials tailed off and the nerve was fully electrically inactive after 10 minutes of TTX-aCSF application (data not shown). The dfMRI ADC measurement protocol was then repeated on the inactive nerves.

6.1.3.4 dfMRI Experiment 2 - Stimulation Gated Method

The peak change in ECS volume in the rat optic nerve upon electrical stimulation occurs approximately 8-10 seconds after the onset of stimulus and returns to baseline after around 50 seconds [96]. A reasonable hypothesis is that the greatest change in the dMRI signal would be measured if the signal was only acquired around this peak time. In order to examine the highest region of the curve, a stimulus gated dMRI experiment was conducted. The Master-8 pulse stimulator was used for MRI sequence timing and was set to initiate a sequence 5 seconds after the EP stimulus was delivered to the nerve.

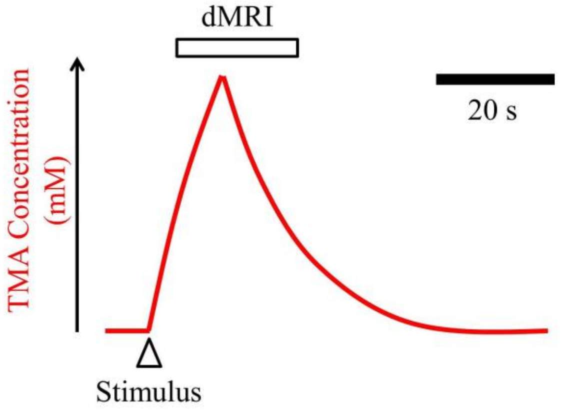

Figure 6.1.5: dfMRI Experiment 2 - Acquisition Timing Diagram.

Showing the ECS shrinkage curve (as an increase in TMA concentration) reproduced from Ransom *et al.* [96] with the dMRI acquisition window for dfMRI experiment 2 in this work overlaid (outline rectangle). Stimulus start time is indicated by the outline arrow. Time is on the x axis; 20 seconds is indicated by the filled block.

The dMRI sequence was designed to take less than 25 seconds in order to sample from the top half of the ECS volume curve (see Figure 6.1.5). dMRI measures were taken during on and off stimulus conditions with the diffusion gradients orientated parallel (a) and perpendicular (b) to the primary direction of the optic nerves. Different nerves were used for each diffusion gradient direction experiment; a total of two. Parallel direction (a) diffusion gradient strengths were 0.1 T/m for the low and 0.225 T/m for the high measurements needed to calculate the ADC. Perpendicular direction (b) diffusion gradient strengths were 0.1 T/m for the low and 0.35 T/m for the high measurements. Other diffusion parameters were Δ = 18 ms & δ = 3 ms. The high and low b-values in the parallel experiment (a) were therefore 109 & 554 s/mm^2 and 109 and 1341 s/mm^2 in the perpendicular experiment (b). A dw-fSE sequence was used with an echo train length of 8; the initial echo time was 27 ms with following echo spacing's of 6 ms. Other imaging parameters were: TR: 600 ms, matrix: 48 x 48, FOV: 6 x 6 x 2 mm, slice orientation was axial and 6 averages were taken for each measurement. The acquisition time for each measurement was 21.6 seconds.

An on/off/on/off paradigm was used with 5 low and high b-value measurements in each block. Electrical stimulus was delivered at 40 V and 50 Hz for

10 seconds. Stimulations were separated by 60 seconds to allow the ECS volume to recover to baseline, individual stimulus duration was 0.02ms. The total scan time for each diffusion gradient direction was therefore 10 minutes for each block and 40 minutes for the entire on/off/on/off experiment.

After the activation experiment, as in dfMRI experiment 1, TTX was added to the aCSF solution. The dfMRI ADC measurement protocol was then repeated on the inactive nerves.

6.2 Results

6.2.1 Potassium Ion Experiments

A single optic nerve was used for each applied concentration of potassium ions and for the sham experiment. Perturbation of optic nerves in the chamber with potassium ion doped aCSF solutions produced the clearest changes in measured ADC, in the parallel direction. ADC changes in the perpendicular direction were also apparent but were less pronounced. Figure 6.2.1 shows the normalized ADC changes for each treatment ± 1 SE for both parallel and perpendicular measurements. A normalized display method was used to highlight the differences induced by the potassium ion treatments as opposed to inter animal variations of the baseline ADC. SNR’s of dMRI images without diffusion weighting with diffusion gradients in the parallel and perpendicular directions were 33.6:1 and 29.2:1 respectively. SNR’s of the highest dMRI images were 5.3:1 and 26.1:1 with diffusion gradients in the parallel and perpendicular directions respectively.

Expt	Excess K^+ (mM)	ADC in $\mu m^2/s$			
		Parallel		Perpendicular	
		aCSF	Excess K^+	aCSF	Excess K^+
Sham	0	901.1 ± 28.87	888.9 ± 37.57	250.7 ± 10.33	259.0 ± 13.47
Low	14	1020 ± 25.20	933.8 ± 51.86	215.0 ± 6.62	201.5 ± 8.21
Med	27	922.9 ± 31.93	790.4 ± 44.49	275.4 ± 17.50	241.9 ± 15.34
High	40	1007 ± 49.42	792.0 ± 44.45	294.6 ± 22.98	258.0 ± 11.86

Table 6.2.1: Potassium Ion Induced ADC Changes.

Showing parallel and perpendicular average ADC (± 1 SE) in separate optic nerves over 20 voxels in each nerve (1 nerve was used for each treatment). ADC values are shown before and after treatment with three different concentrations of excess potassium ions and in the sham control. Statistical differences between each experimental group cannot be calculated due to a single nerve being used for each treatment.

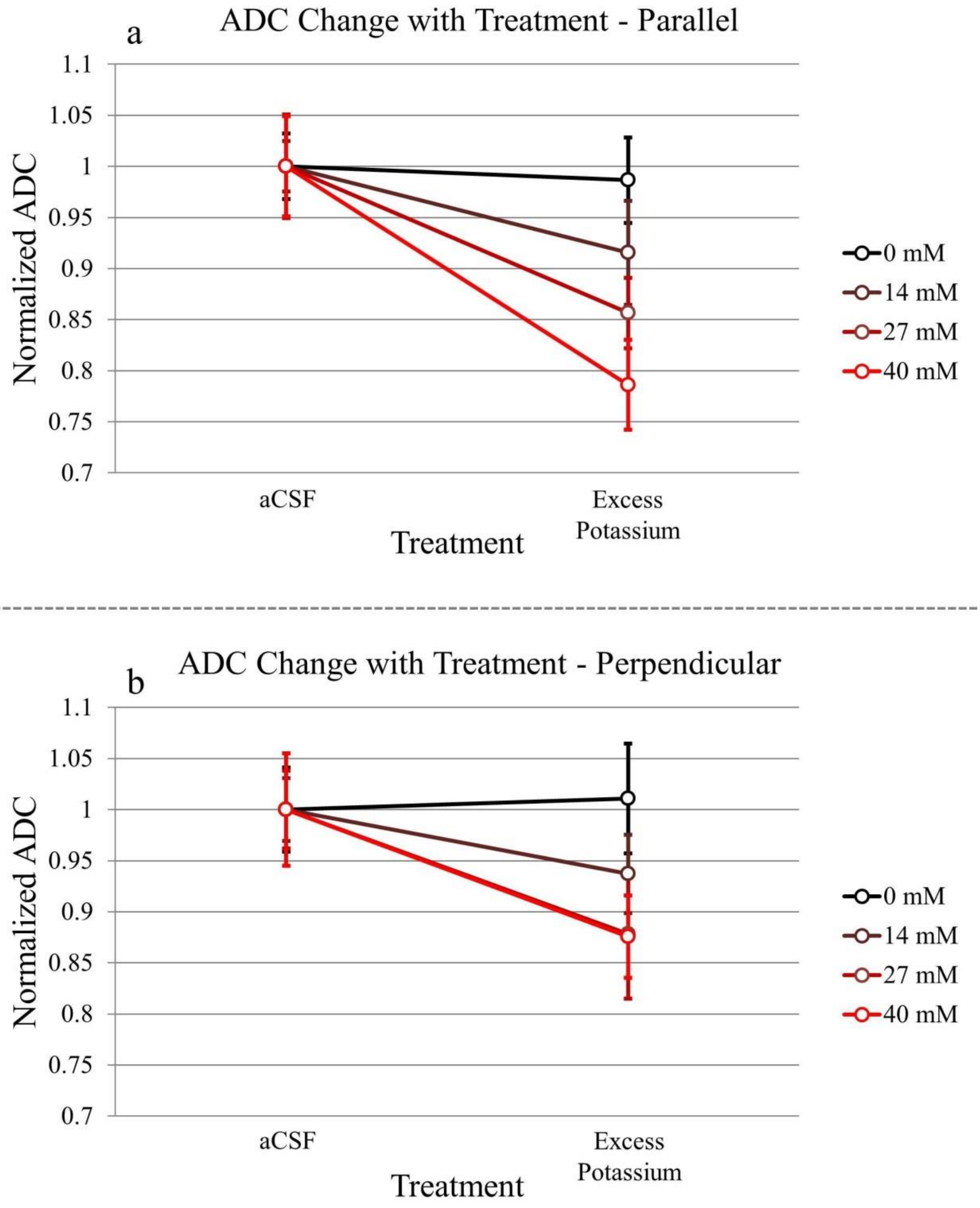

Figure 6.2.1: Potassium Ion Induced ADC Changes.

Showing measured ADC in aCSF and excess potassium ion treatments for the four test solutions; 0, 14, 27 and 40 mM excess potassium ions. (a) Normalized parallel ADC measures and (b) normalized perpendicular ADC measures. Errors bars represent ± 1 SE measured over 20 voxels in each nerve.

6.2.2 EP-MRI Chamber

The adaptations made to the chamber design in section 3.0 to create the EP-MRI chamber did not affect the temperature maintenance behaviour; during all experiments the EP-MRI chamber maintained the bath temperature at 37.0 ± 0.2°C. The double O-ring system prevented leaks around the suction electrode apparatus. The mouse cradle loading rig improved the loading process; the stability was such that once the nerve was set-up in the chamber and clean action potentials were recorded on the prep-bench, the system would remain steady after loading into the scanner bore. The adaptations made to produce the EP-MRI chamber did not noticeably affect the MR image quality (see Figure 6.2.2).

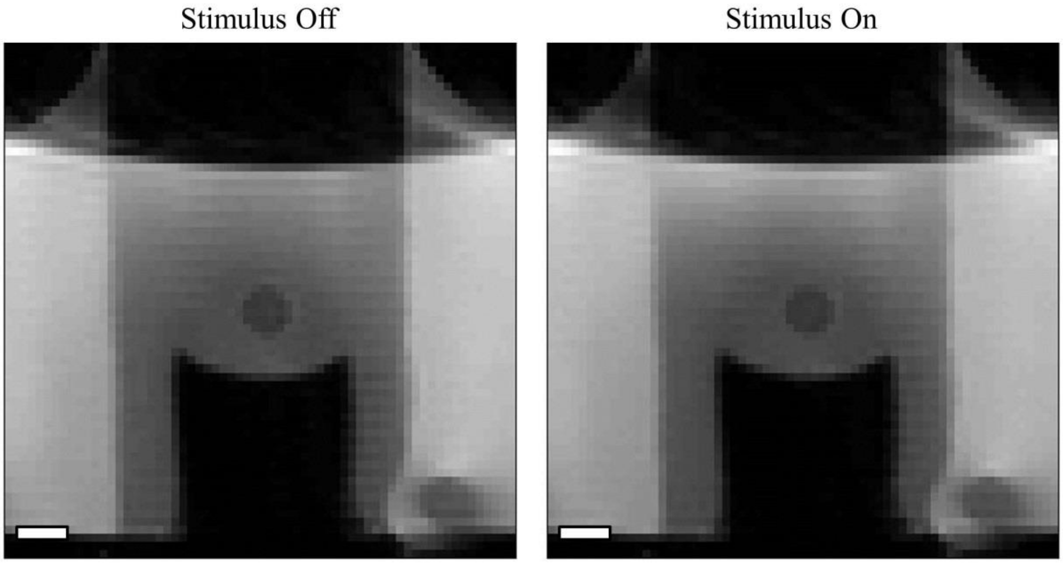

Figure 6.2.2: Low b-value Images Before and During Stimulus.

Showing low b-value diffusion weighted fast spin echo images taken from the EP-MRI chamber with electrical stimulus off and on. The wraparound artefact caused by the small FOV can be seen as can the meniscus at the top of the bath, the carbon reference electrode, the central bench and the nerve itself. Scale bars represent 1 mm.

6.2.3 Bench EP Experiments

A feature of suction electrode recording (in contrast to the grease-gap method) is that recorded signals from the nerve chamber are contaminated with an artefact from the simulation current. The artefact can be removed from the recorded signal by recording a pure stimulus artefact (by removing one end of the nerve from the electrode) and subtracting the two traces [154].

Figure 6.2.3a shows the raw recordings from a nerve in the EP-MRI chamber as the voltage of the stimulus pulse was stepped up. Figure 6.2.3b shows the same process repeated with the nerve removed from the recording electrode. Figure 6.2.4 shows the result of subtracting the stimulus artefact from the raw trace.

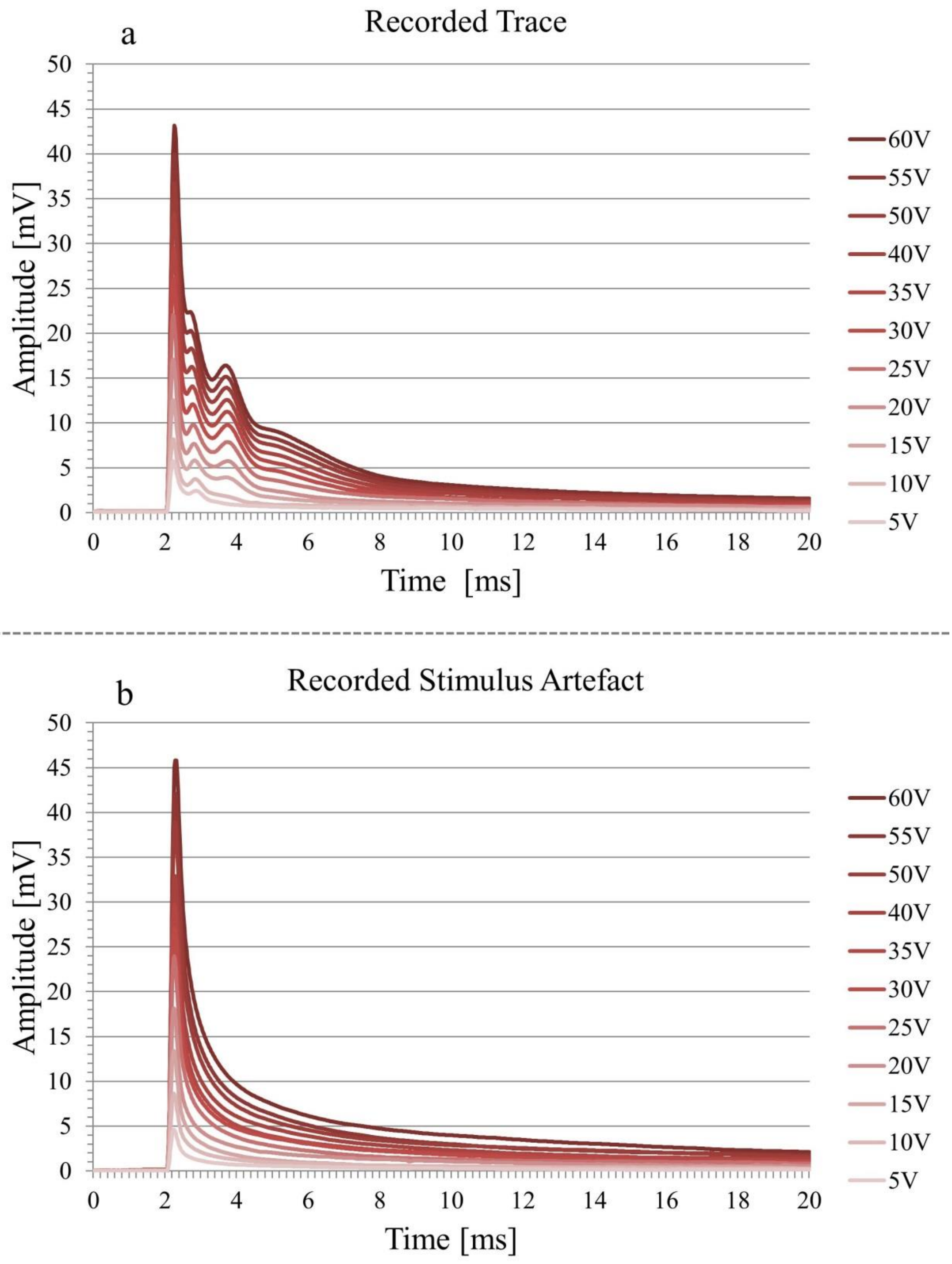

Figure 6.2.3: Recorded Electrophysiology Trace and Stimulus Artefact at Various Stimulus Voltages.

Showing recorded traces from optic nerves in the EP-MRI chamber at a range of stimulus voltages, (a) the combined stimulus artefact and CAP from the optic nerve and (b) the recorded stimulus artefact only, after removal of the nerve from the suction electrodes.

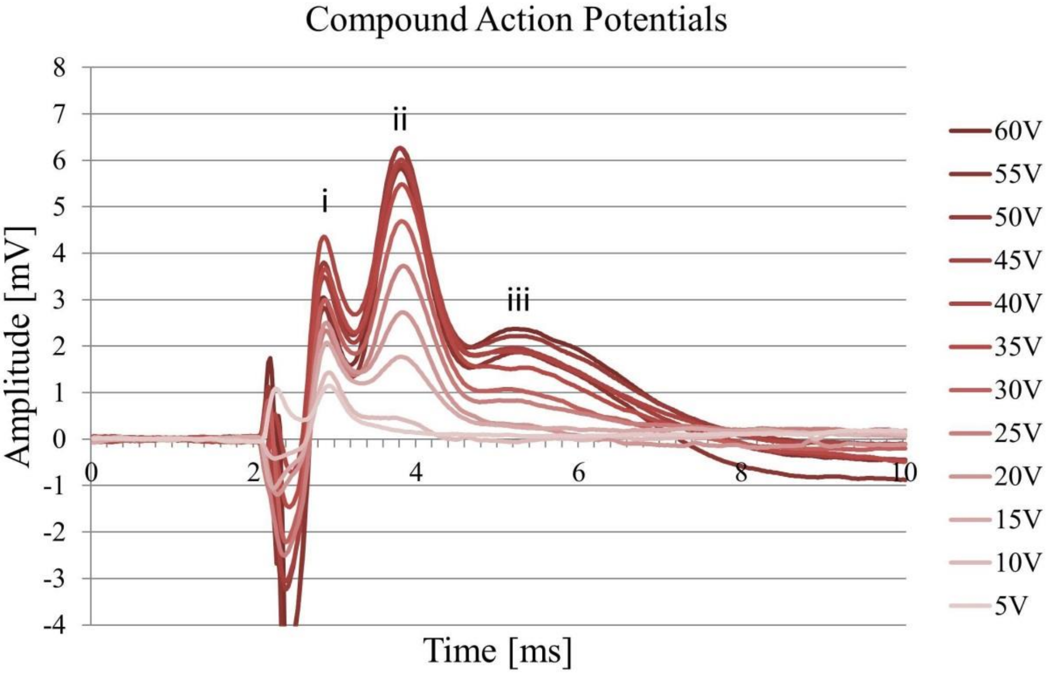

Figure 6.2.4: Compound Action Potentials from Suction Electrode Recordings.

Showing the changing amplitude of the CAP as the stimulus voltage is stepped up. The three peaks of the CAP, the primary, secondary and tertiary, are indicated by ‘i’, ‘ii’ & ‘iii’ respectively.

Once the stimulus artefacts are subtracted from the recorded signal a stimulus response curve can be plotted by measuring the remaining positive voltage of the CAP peaks (i, ii and iii in Figure 6.2.4). Figure 6.2.5 shows the calculated stimulus response curve in the range 0 – 60 V for the primary, secondary and tertiary CAP peaks. A stimulus of 40 V produced the maximum amplitude; this voltage was selected for the EP-MRI experiments.

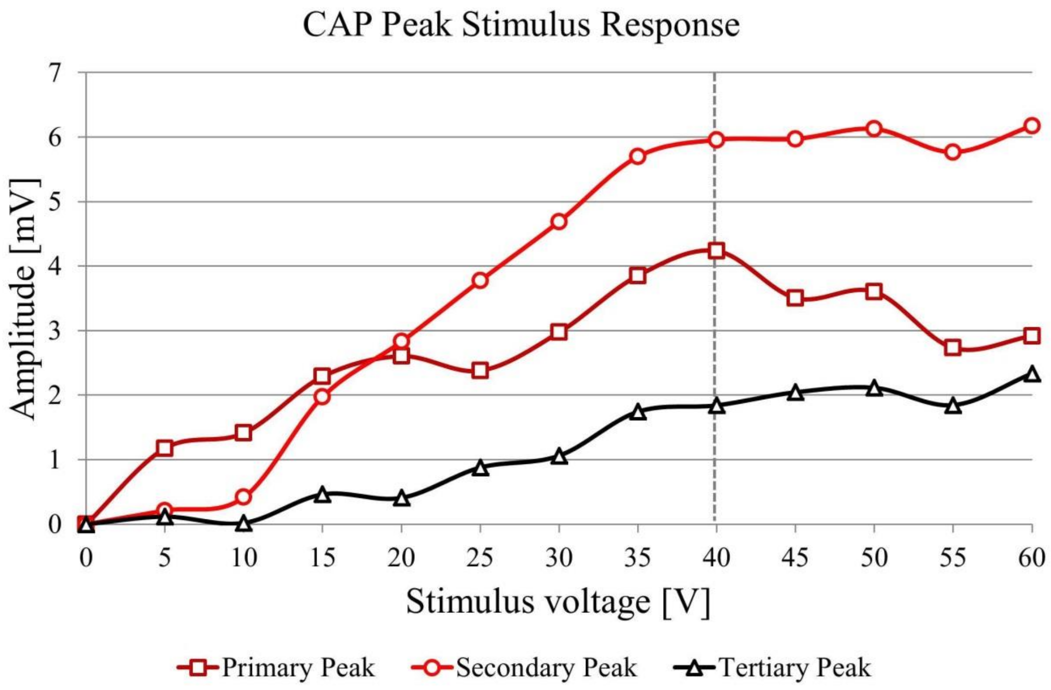

Figure 6.2.5: Compound Action Potential Peak Stimulus Response Curves.

Showing the maximum amplitudes of the three peaks (i, ii and iii in Figure 6.2.4) of the CAP as the stimulus voltage is increased. The dotted line represents the maximum amplitude achieved for all three peaks (40 V stimulation).

6.2.4 MRI EP Experiment

Figure 6.2.6 shows an example EP trace recorded from a single optic nerve in the EP-MRI chamber within the scanner. Figure 6.2.6 also demonstrates the effect of MRI induced artefacts on the trace during a dMRI sequence. There is a consistent repeated pattern of artefacts on the trace every 3ms which are the result of currents induced in the EP recording apparatus by the pulse sequence, in this case most likely the leading and trailing ends of a gradient pulse.

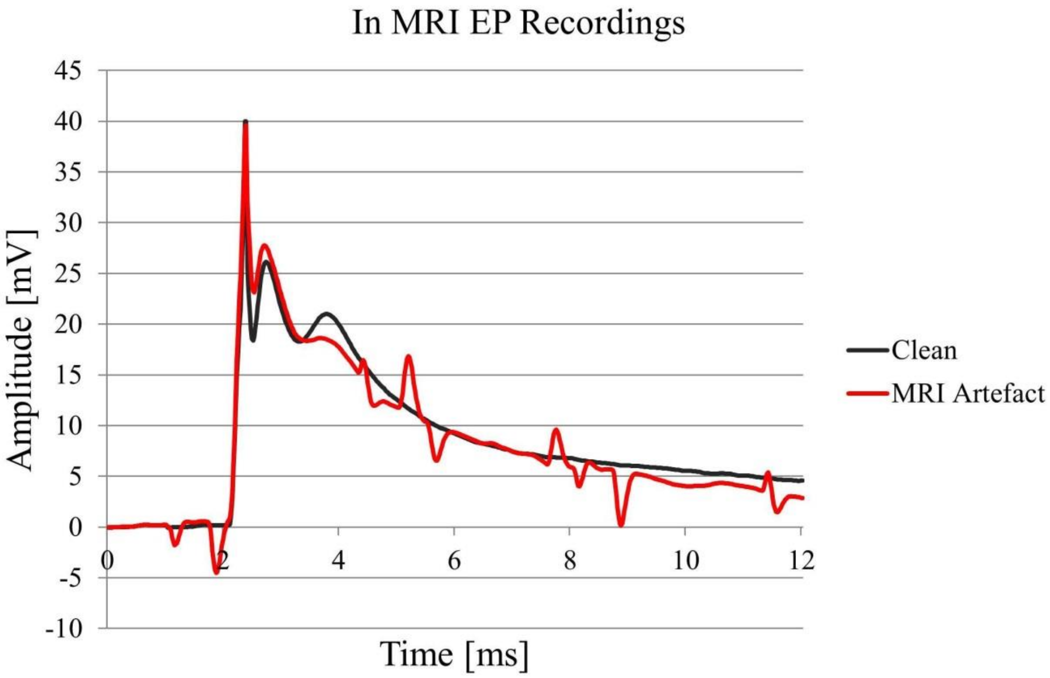

Figure 6.2.6: Clean and MRI Artefact Action Potential Recordings from Optic Nerves.

Showing example action potentials recorded with no sequence running (clean) and with a standard dw-fSE sequence running. The MRI induced artefacts can clearly be seen at regular intervals along the trace.

6.2.5 dfMRI Experiments

During all dfMRI experiments, aCSF temperature in the central bath was stable at 37 ± 0.2ºC. Stimulus pulses produced action potentials with consistent amplitudes for the duration of the stimulus sections of the experiments.

6.2.5.1 dfMRI Experiment 1

Figure 6.2.7 shows the normalized average measured ADC from three nerves in both the on and off conditions. The SNR of the averaged high b-value measurements was 42.2:1 in the perpendicular experiments and 27.8:1 in parallel measurements. Individual high b-value image SNR was 15.2:1 in the perpendicular experiments and 20.1:1 in parallel measurements. A slight difference in ADC is detectable in this experiment. ROI selections were hand drawn on the nerves and covered 24 and 21 voxels in the parallel and perpendicular experiments respectively. Figure 6.2.8 shows the measured ADC at each on/off step over the course of each experiment. Table 6.2.2 shows the calculated ADC's for on and off conditions in the perpendicular and parallel measures in dfMRI experiment 1. Table 6.2.3 shows the calculated ADC's for on and off conditions in the perpendicular and parallel measures in dfMRI experiment 1 after application of TTX to the aCSF.

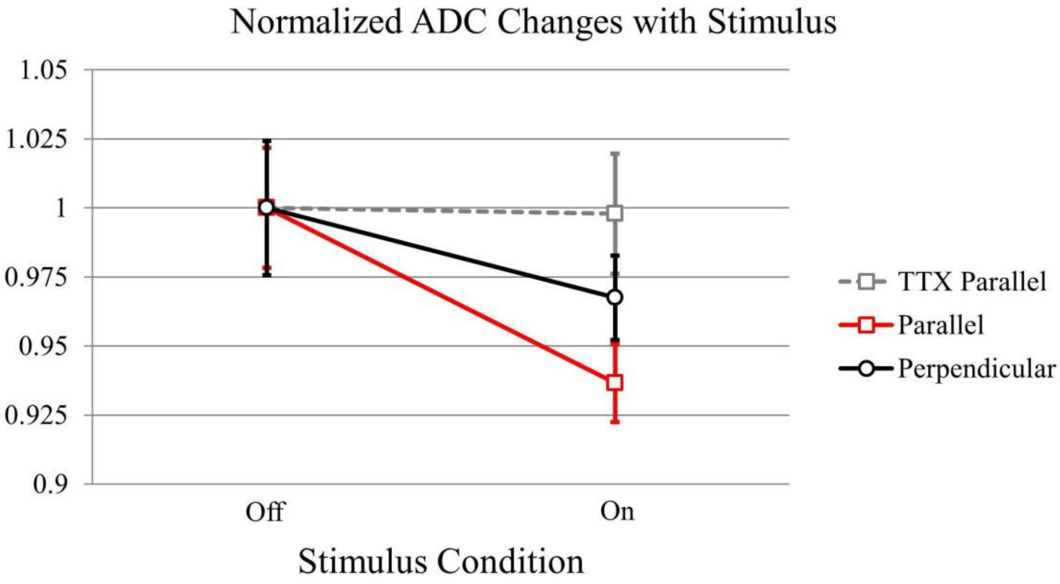

Figure 6.2.7: Normalized Average ADC Changes in dfMRI Experiment 1.

Showing the ADC changes with activation in healthy and TTX disabled optic nerves in dfMRI experiment 1. One nerve each for the parallel, perpendicular experiments, the nerve from the parallel experiment was used again for the TTX experiment. For clarity, only the parallel ADC measures from the TTX treated nerve is shown. Error bars represent ±1 SE of the mean ADC measured over 20 voxels in each nerve.

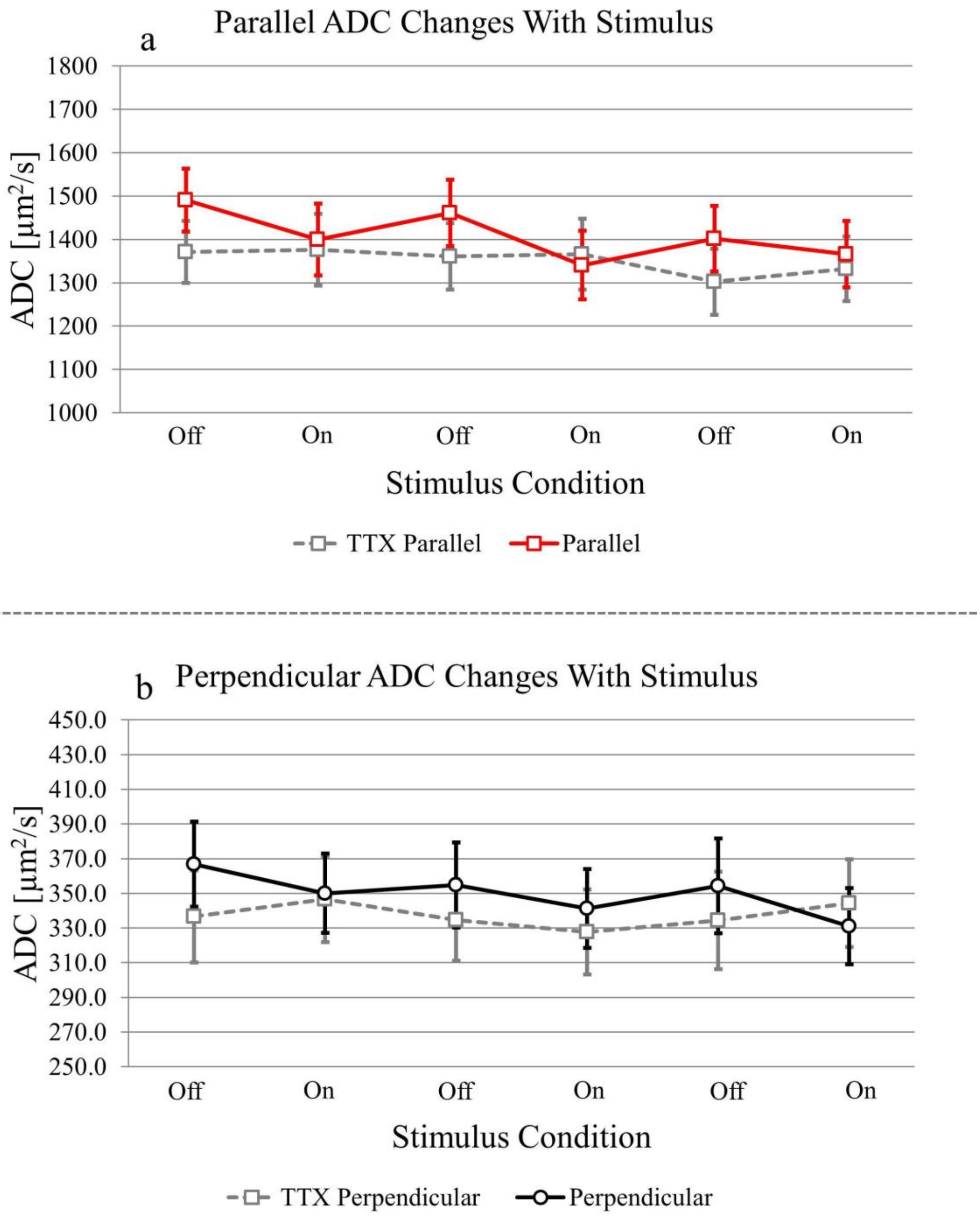

Figure 6.2.8: ADC Changes with Activation During dfMRI Experiment 1.

Showing the variation of measured ADC with activation state over the course of dfMRI experiment 1. (a) ADC measured parallel to the optic nerve before and after TTX application and (b) ADC measured perpendicular before and after TTX application. Error bars represent ± 1 SE of the mean ADC measured over 20 voxels in each nerve.

Stimulus	ADC in µm^2/s					
	Parallel			Perpendicular		
Off	1491	±	72.63	366.7	±	24.53
On	1400	±	82.73	350.0	±	22.87
Off	1461	±	76.64	354.7	±	24.53
On	1341	±	78.73	341.3	±	22.73
Off	1402	±	75.73	354.3	±	27.25
On	1366	±	76.64	331.0	±	22.01

Table 6.2.2: ADC Under Stimulus Conditions in dfMRI Experiment 1.

Showing the average measured ADC ± 1 SE measured over 20 voxels in each nerve in µm^2/s. ADC's were measured during the consecutive on/off conditions in dfMRI experiment 1.

Stimulus	ADC in µm^2/s					
	Parallel			Perpendicular		
Off	1371	±	71.43	336.7	±	26.65
On	1376	±	82.53	346.7	±	24.83
Off	1361	±	76.24	334.6	±	23.55
On	1366	±	81.73	327.7	±	24.43
Off	1302	±	75.93	334.3	±	28.19
On	1332	±	74.64	344.3	±	25.21

Table 6.2.3: TTX-aCSF, ADC Under Stimulus Conditions in dfMRI Experiment 1.

Showing the average measured ADC ± 1 SE measured over 20 voxels in each nerve in µm^2/s. ADC's were measured during the consecutive on/off conditions in dfMRI experiment 1, after application of TTX to the aCSF mixture.

6.2.5.2 dfMRI Experiment 2

Figure 6.2.9 shows the normalized average measured ADC from the nerve in both the on and off stimulus condition. The SNR of the averaged high b-value measurements was 37.5:1 in the perpendicular experiments and 26.2:1 in parallel measurements. Each individual high b-value image SNR was ~9.7:1 in the perpendicular experiments and ~8.4:1 in parallel measurements. No clear difference in ADC can be seen in Figure 6.2.9. Figure 6.2.10 shows the measured ADC at each on/off step over the course of each experiment. Table 6.2.4 shows the calculated ADC's for on and off conditions in the perpendicular and parallel measures in dfMRI experiment 2.

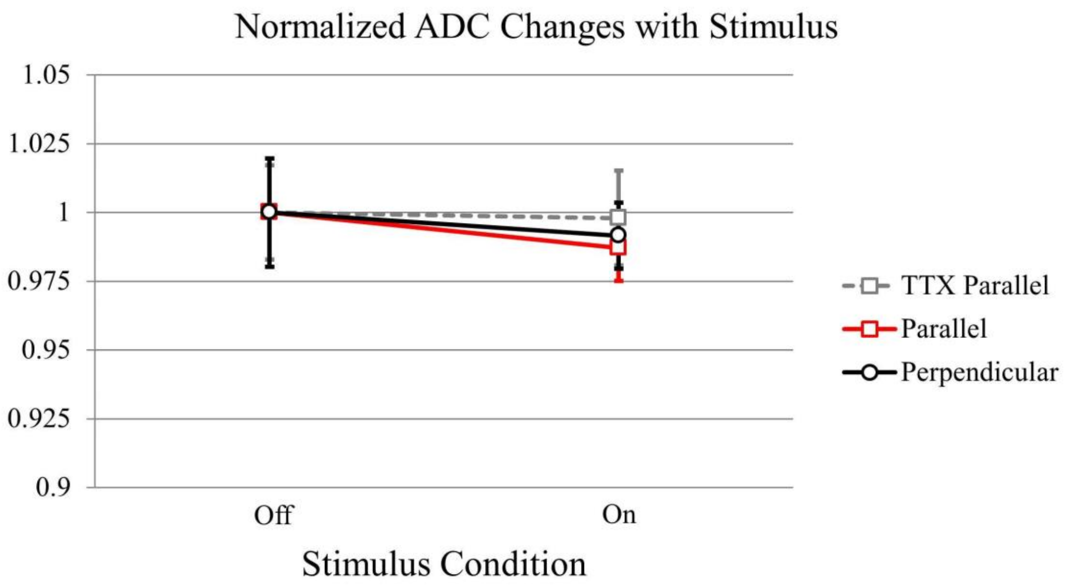

Figure 6.2.9: Normalized Average ADC Changes in dfMRI Experiment 2.

Showing the changes with Activation in healthy and TTX disabled optic nerves in dfMRI experiment 2. One nerve each for the parallel, perpendicular experiments, the nerve from the parallel experiment was used again for the TTX experiment. For clarity, only the parallel ADC measures from the TTX treated nerve is shown. Error bars represent ± 1 SE of the mean ADC measured over 20 voxels in each nerve.

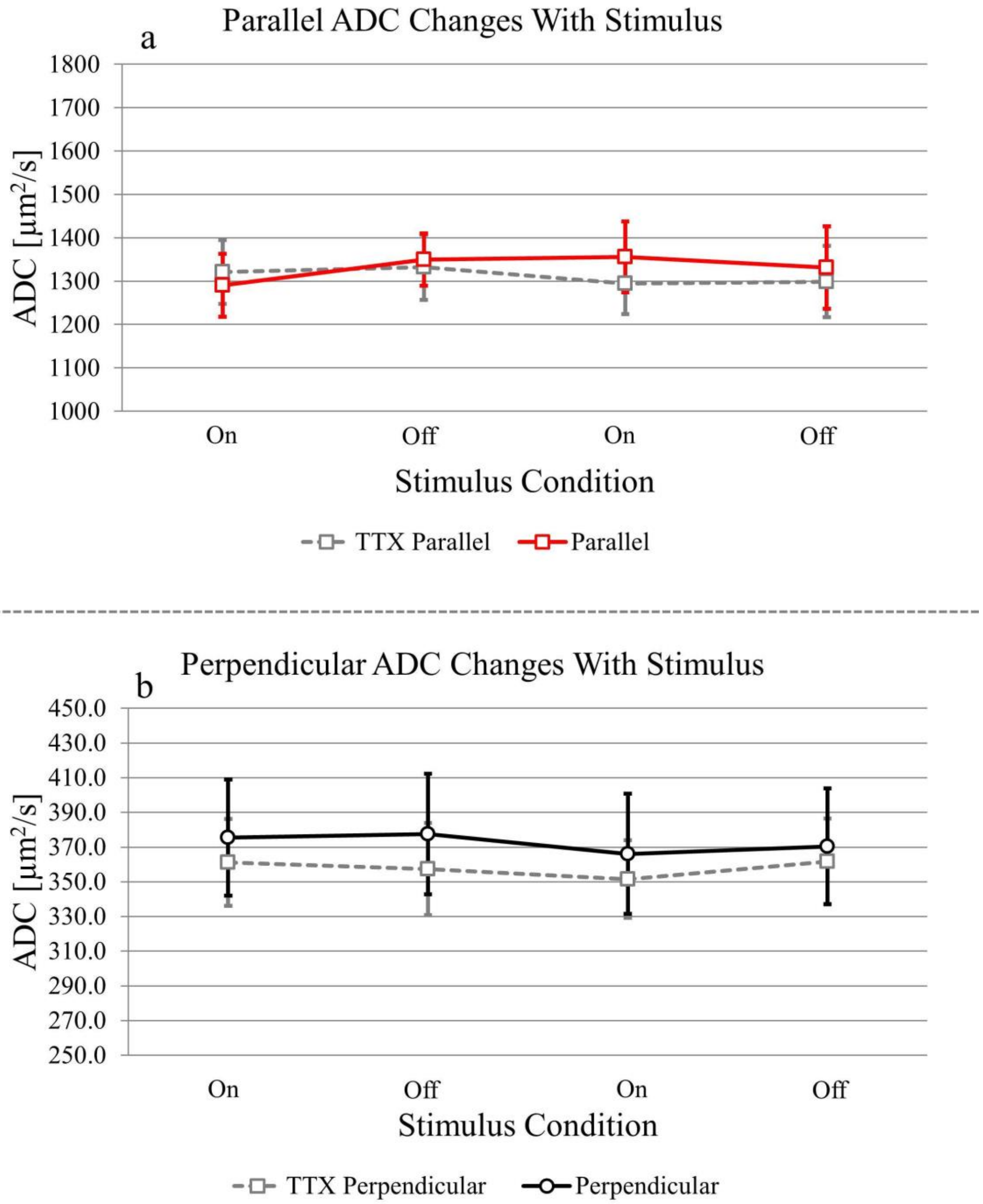

Figure 6.2.10: ADC Changes With Activation During dfMRI Experiment 2.

Showing the variation of measured ADC with activation state over the course of dfMRI experiment 2. (a) ADC measured parallel to the optic nerve before and after TTX application and (b) ADC measured perpendicular before and after TTX application. Error bars represent ± 1 SE of the mean ADC measured over 20 voxels in each nerve.

Stimulus	ADC in μm²/s					
	Parallel			Perpendicular		
On	1291	±	72.88	375.5	±	33.38
Off	1350	±	60.11	377.5	±	34.78
On	1356	±	82.15	366.2	±	34.59
Off	1331	±	95.38	370.5	±	33.23

Table 6.2.4: ADC Under Stimulus Conditions in dfMRI Experiment 2.

Showing the average measured ADC ± 1 SE measured over 20 voxels in each nerve in $\mu m^2/s$. ADC's were measured during the consecutive on/off conditions in dfMRI experiment 2.

Stimulus	ADC in μm²/s					
	Parallel			Perpendicular		
On	1259	±	73.36	320.0	±	25.11
Off	1332	±	75.22	345.6	±	26.56
On	1324	±	71.05	329.7	±	22.36
Off	1299	±	82.01	341.5	±	24.69

Table 6.2.5: TTX-aCSF, ADC Under Stimulus Conditions in dfMRI Experiment 2.

Showing the average measured ADC ± 1 SE measured over 20 voxels in each nerve in $\mu m^2/s$. ADC's were measured during the consecutive on/off conditions in dfMRI experiment 2, after application of TTX to the aCSF mixture.

6.3 Discussion

6.3.1 Potassium Ion Experiments

Potassium ion perturbation experiments were performed as a preliminary component of this work in order to gauge the sensitivity of dMRI measures to structural change in optic nerves in the chamber.

During activation, the potassium ion level in the ECS rises as neurons release it along its concentration gradient [101]. During their refractory period, neurons re-uptake local potassium ions with the sodium-potassium pump. During heavy activation the glial cell population assists in removing excess potassium ions from the local area allowing the neurons to re-establish their local membrane potentials for the next action potential [102]. Exposure of isolated nerves to excess potassium ions leads to swelling of glial cells as they uptake potassium ions [156] and associated chloride ions in order to preserve electroneutrality. This uptake leads to osmotic swelling of the glial cells.

Exposure to excess potassium ions under isosmotic conditions is a useful method to create controlled perturbations in the ECS [67]. The excess potassium ion levels selected for these experiments were, as mentioned above, based on the concentrations used in a previous dMRI experiment on optic nerves [67]. These were the levels seen during activation [99,101] and a mid-point between the two.

Changes were seen in ADC measured parallel and perpendicular to the nerve at all concentrations. However, a difference in the degree of ADC change induced by excess potassium ions was seen between the parallel and perpendicular ADC measurements. This suggests that the microstructural changes induced by potassium ion perturbation have a greater effect on the parallel ADC than the perpendicular ADC. This result does not agree with previous work by Anderson *et al.* [67] using 40 mM excess potassium ions in the optic nerve where ADC changes were most pronounced in the perpendicular direction. This previous work was conducted at 21ºC, it is not clear how the temperature difference between this experiment and that of Anderson *et al.* might cause this difference. One possibility is that cooler temperatures restrict the motility of the cell membranes and lead to swelling patterns unlike those seen at *in vivo* temperatures. This question could be investigated in greater detail by altering the temperature of measurements conducted in the chamber and correlating the ratio of parallel and perpendicular ADC changes to temperature, but this was not the aim of this experiment.

These preliminary potassium ion perturbation experiments suggested that small structural changes could be detected with dMRI measures of ADC in the optic nerve and so the decision was made to continue with the development of the EP-MRI chamber.

6.3.2 EP-MRI Chamber

The EP grease gap recording method, while a practical solution for the goals of section 4.0, is not feasible for recording in the narrow confines of the scanner bore (20 cm bore diameter and a 33 mm coil internal diameter). Due to the lack of space, setup of the nerve in the chamber and of any recording devices must be done outside the scanner prior to inserting the rig into the bore. In the grease gap setup, the stimulus electrode must be carefully positioned in contact with the surface of the optic nerve. Once in position the electrode is highly sensitive to agitation. In addition, the electrical seal created by the dividers (see Figure 3.2.3a) and the silicone grease applied to them can easily be disrupted by movement. For this reason a different EP method, suction electrodes, was used for the EP-MRI chamber.

Extensive adaptations were required to alter the chamber described in section 3.0 for suction electrode recordings. Several iterations of the design were required to work out various flow and leaking problems until the design shown above was chosen. The delicate nature of the glass suction electrodes causes several problems during development as the slightest knock during loading or positioning snapped them off, usually leaving shards of glass in difficult to reach places within the chamber. The loading rig and support bar mostly mitigated this issue but great care was still required.

6.3.3 Bench EP Experiments

Electrophysiology recordings from optic nerves were conducted in the new EP-MRI chamber in order to assess its performance and calibrate the stimulus voltage to produce the greatest effect for later dfMRI experiments.

The suction electrode set-up proved simple to use and stable, and the nerve can be dropped into place using a pipette with a rubber pipette filler attached. The electrodes are then slotted into place over each end and a small amount of suction is applied to secure the ends against the constriction in the end of each glass capillary. When the nerve is cut out the axons are cut. During accommodation in the aCSF bath the axons close up, sealing in the cytosol. If too much suction is applied the seal can break and the nerve ceases to be electrically functional so a delicate hand is therefore needed.

Bench EP experiments demonstrated the functionality of the system and that suitably large CAPs could be discerned from the stimulus artefact during recording. This feature was essential for setting up the chamber for dfMRI experiments as pausing to calculate the artefact-removed trace during the set-up is not practical.

6.3.4 MRI EP Experiment

MRI EP experiments demonstrated the functionality of the EP-MRI chamber in the MRI scanner. MRI sequences did introduce significant artefacts into the EP trace. MRI induced artefacts were regular and of smaller amplitude than the recorded CAPs and so could be easily subtracted if simultaneous EP and MRI measurements were required. Care had to be taken once the nerve was positioned not to agitate the rig during loading. If either end of the nerve slipped from its electrode the EP signal was lost, which usually happened just as the rig was loaded.

The EP-MRI chamber then is the first demonstrated example of a bi-modal isolated viable nerve imaging device capable of making simultaneous electrophysiology and MRI measurements. Various other adaptations could be made to the chamber in order to apply it to a range of basic science MRI experiments.

6.3.5 Functional Diffusion MRI Experiments

dfMRI experiment 1 suggests that there is as expected, a slight negative change in ADC during electrical stimulus in this isolated model system. The effect is most pronounced in the parallel ADC measurements (- 6.75%) and less so in the perpendicular measurement (- 3.36%), correlating with the behaviour seen in the potassium ion perturbation experiments. In addition the TTX control method prevented ADC changes. This suggests that the dfMRI response detected was due to a change in tissue microstructure resultant from ion flux and not an artefact of the current delivered to the electrodes.

The detected effect demonstrated in dfMRI experiment 1 is subtle and not comparable to that seen in the *in vivo* mouse optic nerve experiments conducted by Spees *et al.* [111]; In [111] the average change in the perpendicular ADC measurements was a statistically significant, -27% varying between -9 and -35% in five animals, and the average change in parallel ADC reported was +1.8% (no data on the range was given). No SNR data are reported in [111], but the sequence parameters given and their use of a lower field system suggest that it was likely lower than the level achieved in this work.

In this preliminary experiment a single nerve was used in contrast to the 5 used in [111] and so these data cannot conclusively contest the results of [111].

However, the much lesser response seen in these data and the lack of response in previous work [110] suggest that the greater and differing ADC changes seen in [111] may be driven by a different process which outweighs the effects of ECS shrinkage. Blood vessels in neuronal tissue enlarge their diameter in response to increasing metabolic demands and synaptic transmission, this process being known as functional hyperemia [157,158]. In [111] the authors suggest that they have controlled for the effects of activation induced changes in blood flow by using hypercapnia-induced brain blood flow enhancement in the animals. While long term hypertension impairs functional hyperemia in rats, recent work has shown that short term hypertension (up to ten weeks) has no significant effect on the coupling of regional cerebral blood flow and neural activation [159]. It is therefore unlikely that a short term global increase in blood pressure would reduce the vascular response to neuronal activation in the optic nerve. The changes caused by blood vessel dilation due to neuronal activation and the resultant blood movement are therefore likely to have a significant influence on the local MR and diffusion weighted MR signal, even during temporarily induced hypertension. A practical method to control fully for the effects of blood movement on the MRI signal is to remove the blood entirely, as in the experiments described here.

Previous dfMRI work with isolated spinal cords and sciatic nerves of American bullfrogs (known as *Rana catesbiena* at the time, now changed to *Lithobates catesbeianus*) at 22°C, showed no significant response to electrical activation [110]. However, temperature has significant effects on water diffusion measurements [74] and mammalian tissue may differ in behaviour to amphibian tissue. In addition no recording was carried out in [110], so the level of stimulation could not be determined once the rig was in the MRI scanner.

The stimulation method used in this work may not be as efficient as the retinal illumination method used in the *in vivo* mouse optic nerve experiments. If stimulation efficiency is low, a lesser degree of ECS shrinkage and a correlated lesser ADC response would be expected. Quantification of the number of neurons stimulated by suction electrode EP experiments in not possible, but the high stimulation voltages used and the large amplitudes and multi peak patterns of the recorded CAPs suggest that a significant fraction of neurons in the nerve were active.

dfMRI experiment 2 was conducted in an effort to detect a greater effect on the dMRI signal during activation, after the results from dfMRI experiment 1 had been analysed. The preliminary results shown here demonstrate that this method in fact produced a lesser effect on ADC. The lesser changes measured in dfMRI experiment 2 compared with dfMRI experiment 1 indicate that a large sustained period of activity is required to produce detectable ADC reductions upon activation in this set-up.

More recent work, in isolated neonatal rat spinal cord using chemical stimulation, detected an ADC decrease in the grey matter [160]. This experiment, like the bullfrog work [110], was conducted at room temperature. However, the magnitude of the ADC changes (19.5%) is a promising result and suggests that a true dfMRI effect can be observed in grey matter. Interestingly, no clear effect was observed in the white matter regions of the cords. Neonatal neuronal tissue is not fully developed compared to mature tissue (e.g. myelination is not complete and cells are sparser). Therefore it is not known how these results would translate to mature white or grey matter. The drug induced activation and the resultant ADC changes in [160], may not be representative of any *in vivo* effects induced by electrical activation.

6.3.6 Conclusion

The potassium ion perturbation experiments described here demonstrate that subtle structural changes can be detected with dMRI ADC measures in rat optic nerves in the VIT chamber.

The EP-MRI VIT chamber developed in this work has all the functionality of the VIT chamber discussed in previous sections and allows bi-modal measurements from viable isolated rat optic nerves.

Preliminary dfMRI experiments in blood-flow free optic nerves, particularly in dfMRI experiment 1, suggest that activation induced structural changes lead to subtle dMRI measurable effects. This result is expected as the ECS has been shown to reduce in volume upon activation in isolated rat optic nerves. Previous dfMRI work has been conducted *in vivo* where the confounding effects of blood flow cannot adequately be separated from the structural changes in the ECS. The effect on water diffusion appears to be subtle, so further work characterising the changes in this model system may enable isolation the dfMRI response from the vascular effects *in vivo*.

7.0 Summary and Conclusions

Magnetic resonance imaging has become a valuable tool for medical imaging as it allows the clinician or researcher to probe within the living body non-invasively and with non-ionising radiation. Diffusion weighted MRI is a powerful tool for MRI, producing new information from MR images, effectively probing for features of the microstructure on a sub-voxel level. Development of dMRI methods requires extended scan times and stable samples; for this reason chemically fixed ex vivo tissues and more rarely, viable isolated tissue have been used as model systems.

A viable tissue maintenance device able to preserve tissue at physiological temperatures for extended MR scan periods has not previously been demonstrated or validated. This work aimed to produce such a device; the VIT chamber.

The VIT chamber was then applied to two main projects:

1. To study dMRI properties of VIT and fixed tissue in controlled physiologically relevant conditions.
2. To investigate the dMRI detectability of structural and functional perturbation of the rat optic nerve in controlled physiologically relevant conditions.

This section consists of a brief summary of conclusions from each section of the above work followed by possible future directions for this work, an itemized list of work and a list of publications produced.

7.1 VIT Chamber: Design and Development

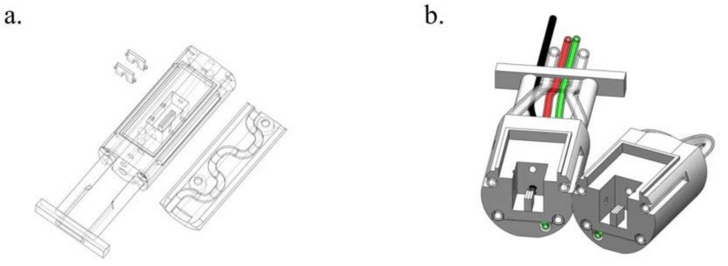

Figure 7.1.1: Summary Figure for VIT Chamber Design and Development.

Showing in (a), a wireframe schematic of the final chamber and in (b), a sliced folded image of the imaging area of the chamber, with perfusion tubes and temperature probe shown.

An MRI compatible viable isolated tissue imaging chamber was designed and produced. The chamber was designed to maintain a section of rat optic nerve at physiological temperatures during long term scanning in a 26mm diameter RF coil of a high field MRI system. The chamber was also designed to allow grease-gap electrophysiological recordings from a rat optic nerve installed within, this feature was based on designs for a brain slice grease gap chamber produced by Batchelor *et al.* [113]. The Chamber was able to maintain stable temperatures for ten hours.

7.2 MRI Compatible VIT Chamber Validation

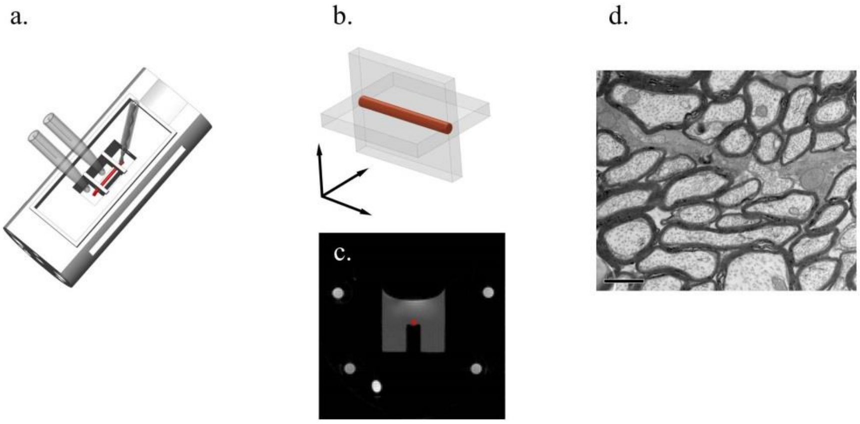

Figure 7.2.1: Summary Figure for the Validation of the VIT Chamber.

Showing in (a) the VIT chamber with grease-gap inserts in place and the stimulation and recording electrode. The gradient layout for the 1D dMRI stability measures is shown in (b). An example MRI of the central slice of the chamber is shown in (c). A section of an electron-micrograph showing a 10 hour maintained nerve is shown in (d).

The VIT chamber was thoroughly tested. The chamber's ability to maintain a section of isolated rat optic nerve at physiological temperatures for ten hours was demonstrated with electrophysiology, electron microscopy and diffusion weighted MR methods. The VIT chamber was shown to be unique in its capability for stable MRI measurements from VIT. These experiments were published in the peer-reviewed journal *Magnetic Resonance in Medicine* [9].

7.3 VIT and Fixed Tissue Comparison

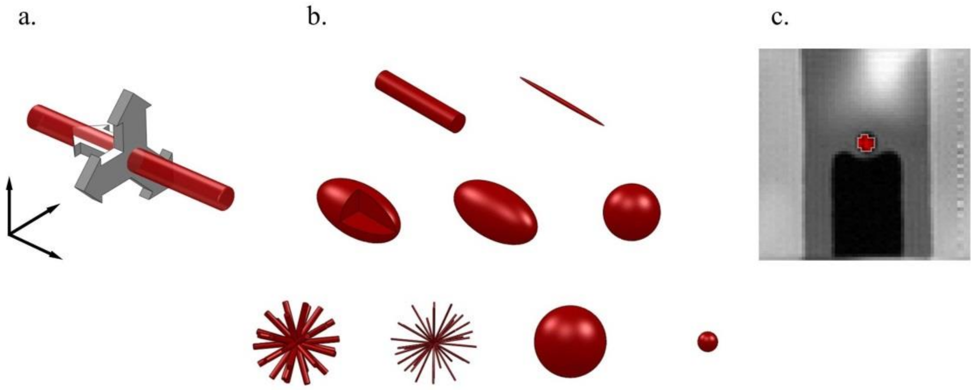

Figure 7.3.1: Summary Figure for VIT and Fixed Tissue Comparison Experiment.

Showing, in (a) the gradient directions applied to the optic nerve for the multi-direction-multi-b-value dMRI experiment. In (b), graphical representations of the fitted model compartments and in (c), example MRI with the ROI used on the optic nerve.

The validated VIT chamber was used to investigate the dMRI detectable differences between viable and fixed isolated rat optic nerve in order to inform the range of dMRI studies using fixed tissue as an analogue for *in vivo* tissue. A range of DTI experiments and application of a taxonomy of complex multi-compartment models demonstrated measurable differences but common patterns of water compartments between fixed and viable tissue. These data suggested that while fixed tissue can be a useful tool for development of dMRI methods, results from such work may not directly translate to VIT or *in vivo* work. These experiments were published in the peer-reviewed journal *Magnetic Resonance in Medicine* [10].

7.4 Perturbation and Functional dMRI Study

Figure 7.4.1: Summary Figure for the Perturbation and Functional dMRI Study.

Showing, in (a): the EP-MRI chamber, in (b) a photograph of the EP-MRI support equipment and in (c) the normalized ADC changes seen upon addition of increasing concentrations of potassium ions to the aCSF mixture.

The VIT chamber was used to probe for dMRI detectable structural changes induced by application of excess potassium ions to viable optic nerves. The chamber was then adapted to enable in MRI electrophysiological stimulation and recording from viable optic nerves. This new EP-MRI chamber was tested and applied to preliminary experiments to probe for a truly structural functional diffusion MRI effect.

Preliminary experiments demonstrated that small structural changes can be detected with dMRI in potassium ion perturbation experiments. dfMRI experiments suggested that a small dMRI change induced by electrical stimulation may be detectable.

This work described the first in MRI viable electrophysiology stimulation and recording device for isolated tissue at physiological temperatures. This tool has a range of applications in future work.

7.5 Future Directions

7.5.1 General Chamber Adaptations/Improvements

While the temperature of the chamber can be maintained at 37ºC for ten hours (see section 3.0) a feedback temperature control system would be of value for making dMRI measures at a range of temperatures. A simple adaptation to the hot water pumping system could be made to allow such control by linking its temperature response to the recorded bath temperature.

The VIT chamber fits into a 26mm volume coil but greater SNR improvements could be made by addition of a small RF coil into the chamber body itself [161]. This adaptation could be made relatively easily as the path for the coil and its capacitors/cables could be directly printed into the body of the chamber.

The EP-MRI chamber could be made easier to use by development of an automatic loading rig on smooth bearings. This would prevent agitation of the electrodes or jogging of the sample by human error.

7.5.2 Testing of Multi-Compartment Models

The VIT chamber provides a valuable tool for testing and development of complex multi-compartment models as demonstrated in section 5.0. More complex models including exchange and further compartments could be tested and developed with this system.

More complex models could also be applied in future to further investigate fixed and viable tissue differences. Models including permeability of compartments may help to shed light on possible membrane permeability changes caused by fixation.

7.5.3 Functional dMRI in the Optic Nerve

Further work with the EP-MRI chamber using the methods described in section 6.0 will strengthen the conclusion of preliminary experiments that a true dfMRI effect can be measured in isolated systems. If the effect can be demonstrated strongly, further work with multi-compartment modelling would enable the extraction of compartment specific effects. For dfMRI to become a useful clinical tool the effect must be fully characterised in a blood free isolated system. The effects of blood flow could then be modelled and extracted from the *in vivo* signal to reveal the dfMRI effect.

Other activation methods could be tested with adaptations to the EP-MRI chamber. For example, optogenetic methods [162] could be used for selective activation of astrocyte or neuronal populations in the nerve to disentangle their contribution to the dfMRI signal.

7.5.4 Axonal Transport

The VIT chamber provides an ideal model system for the testing and development of axonal transported contrast agents such as Manganese e.g. [59] and superparamagnetic nano-particles e.g. [163]. The transport and uptake rates of such agents could be measured and characterised in great detail with only minor adaptations to the chamber (sealed compartments created with greased barriers).

7.5.5 Adaptation for Brain Slice

A VIT brain slice tissue model system including section of grey and white matter would be of great value as a development tool. Previous work with a brain slice maintenance device has been demonstrated [65], but this work was not conducted at physiological temperatures and the device was designed for a vertical bore MR system. The VIT chamber could be adapted to maintain for example a rat or mouse brain slice section of up to 400 μm in thickness. The slice could be kept at physiological temperatures and used in most pre-clinical horizontal bore MRI systems.

7.5.6 Curving and Crossing Model System for Tractography Testing.

The VIT chamber could be adapted to force the rat optic nerve into a curving shape which would provide a valuable tool for testing of diffusion MRI tractography [164] methods. Sections of the successful dMRI tractography phantom in the ‘fibre cup’ [165] could be replicated in real tissue. For example, the optic chiasm, where the two optic nerves cross, could also be used in the chamber as a fibre crossing phantom. A controlled and *in vivo* realistic viable tissue phantom may provide more valuable assessment of new tractography methods than artificial phantoms.

7.6 Itemized List of Work

The following is a summary of all relevant work completed during the course of this PhD.

7.1.0 Chamber Development

- 3D design and manufacture of prototype VIT chamber
- Compatibility testing of prototype chamber, MR measurements, safety etc.
- Temperature maintenance testing of prototype chamber
- Further prototyping to improve temperature stability
- Adaptation of chamber for electrophysiology compatibility

7.6.1 Tissue Stability Testing

- Rat optic nerve rapid extraction procedure setup
- Maintenance of optic nerves in chamber for electron microscopy
- Electron microscopy of osmium stained samples
- Electrophysiology of viable optic nerves in chamber
- Development and application of dMRI methods for 1D stability imaging of optic nerve
- DTI stability testing

7.6.2 VIT and Fixed Tissue Comparison

- Development of multi-b-value dMRI sequence, testing and calibration
- Acquisition of multi-b-value dMRI data, fixed and VIT
- Acquisition of DTI parameter dependence data, fixed and VIT total n=6
- Analysis of data with CAMINO software package

7.6.3 Perturbation Experiments

- Preliminary feasibility testing the dMRI detectability of structural changes caused by excess potassium ion perturbation in the optic nerve.

7.6.4 Development and Applications of an EP-MRI Chamber Variant

- Development and testing of an electrophysiology and MRI capable version of the chamber; the EP-MRI chamber.
- Preliminary dfMRI experiments using the simplified system achieved with the EP-MRI chamber.

7.6.5 Collaborative Work

- Design and production of gradient calibration phantom for Agilent 9.4T MRI scanner
- Design and production of various *in vivo* imaging equipment e.g. tumour ridden mouse MR cradle, secure rat head clamp for stable fMRI, multi mouse and rat brain imaging holder and a tumour ridden mouse cradle for photo-acoustic imaging.

7.7 Publications

7.7.1 First Author Journal Publications

Richardson, S., Siow, B., Batchelor, A. M., Lythgoe, M. F. & Alexander, D. C. A viable isolated tissue system: A tool for detailed MR measurements and controlled perturbation in physiologically stable tissue. Magn. Reson. Med. 69, 1603–1610 (2013).

Richardson, S., Siow, B., Panagiotaki, E., Schneider, T., Lythgoe, M. F. & Alexander, D. C. Viable and fixed white matter: Diffusion magnetic resonance comparisons and contrasts at physiological temperature. *Magn. Reson. Med.* n/a–n/a (2013).doi:10.1002/mrm.25012

7.7.2 Mid Author Journal Publications

Walker-Samuel, S., Ramasawmy, R., Torrealdea, F., Rega, M., Rajkumar, V., Johnson, S. P., **Richardson, S.**, Goncalves, M., Parkes, H. G., Arstad, E., Thomas, D. L., Pedley, R. B., Lythgoe, M. F. & Golay, X. In vivo imaging of glucose uptake and metabolism in tumors. *Nat Med* **19**, 1067–1072 (2013).

Wells, J.A., O'Callaghan, J.M., Holmes, H.E., Powell, N.M., Johnson, R.A., Siow, B., Torrealdea, F., Ismail, O., Walker-Samuel, S., Golay, X., Rega, M., **Richardson, S.,** Modat, M., Cardoso, M.J., Ourselin, S., Schwarz, A.J., Zeshan Ahmed, Murray, T.K., O'Neill, M.J., Collins, E.C., Colgan, N., Lythgoe, M.F. In-vivo Imaging of Tau Pathology using Multi-Parametric Quantitative MRI, Brain, in press.

O'Callaghan, J.M., Wells, J., **Richardson, S.,** Holmes, H., Yu, Y., Siow, B., Walker-Samuel, S. & Lythgoe, M.F. Is your system calibrated? MRI gradient system calibration for pre-clinical imaging, *Submitted.*

7.7.3 First Author Conference Publications

Richardson S., Siow B, Batchelor A. M., Lythgoe M. F., Alexander D. C. Development and rapid manufacture of an MRI compatible incubation/perfusion chamber for high-resolution diffusion MRI imaging of live excised tissue – a methodology and proof of viability. Oral presentation at BCISMRM PDS Cambridge 2011.

Richardson S., Siow B., Batchelor A. M., Lythgoe M. F., Alexander D. C. Design, Development, Manufacture and Validation of an MRI Compatible Tissue Maintenance Chamber. Poster presentation BCISMRM Manchester 2011.

Richardson S., Siow B., Batchelor A. M., Lythgoe M. F., Alexander D. C. Development and Stability Testing of an MRI Compatible Isolated Tissue System. Poster presentation ISMRM Melbourne 2012.

Richardson S., Siow B., Batchelor A. M., Lythgoe M. F., Alexander D. C. Viable and Fixed White Matter: DTI and Microstructural Comparisons at Physiological Temperature. Oral presentation at ISMRM Salt lake City 2013.

7.8 List of Abbreviations and Definitions

This section comprises an alphabetically ordered list of abbreviations and definitions from the body of text above. Page numbers of their first occurrence in the main text are included.

Additive layer manufacturing (ALM)	49
Apparent diffusion coefficient (ADC)	34
Artificial cerebrospinal fluid (aCSF)	61

7.9 Appendix 1

This appendix shows the electron-micrographs used for structural stability analysis in section 4.0. Figure legends describe the positioning and relative sampling area for each nerve sample.

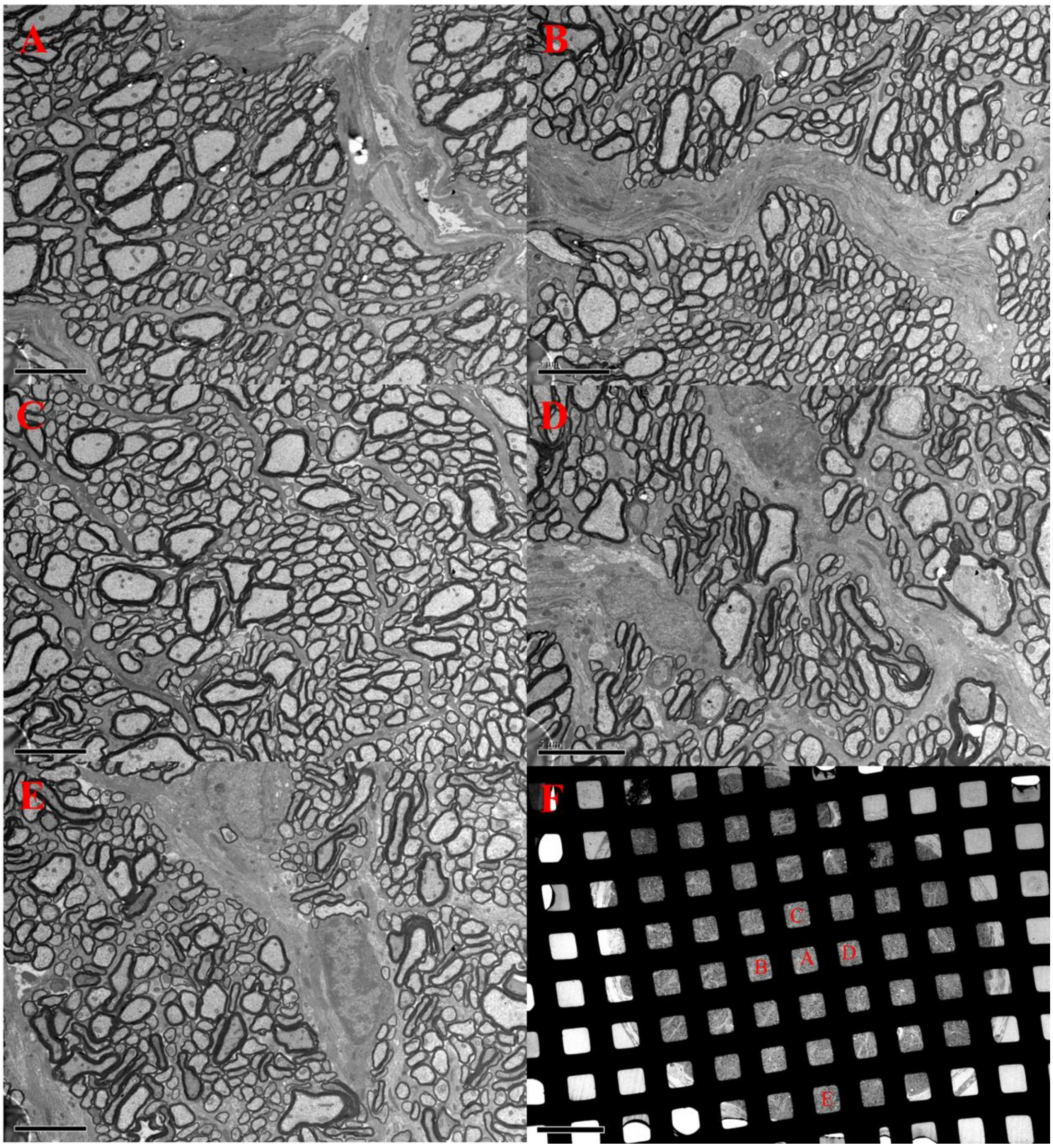

Figure 7.9.1: Appendix 1, Zero Hour (Control) Maintained Nerve.

Showing transmission electron micrographs A-E, from the zero hour maintained (control) nerve. Micrographs A-D were used for sampling in section 4.0. Grid image (F) shows the position of the sample areas in relation to the whole nerve (grid is the sample support tray). Scale bars on images A-E represent 5 µm. Scale bar in panel F is 100 µm. Each grid square covers 1320 µm^2, and each sample image covers 975 µm^2 (in order to prevent overlap with curved grid edges). The total nerve area in this sample is ~222670 µm^2. The total visible area of the nerve not obscured by the grid is 65995 µm^2 and the total area analysed in the four samples is 3900µm^2, which is 5.9% of the visible nerve area. For analysis every visible neuron (black rings) was selected and measured.

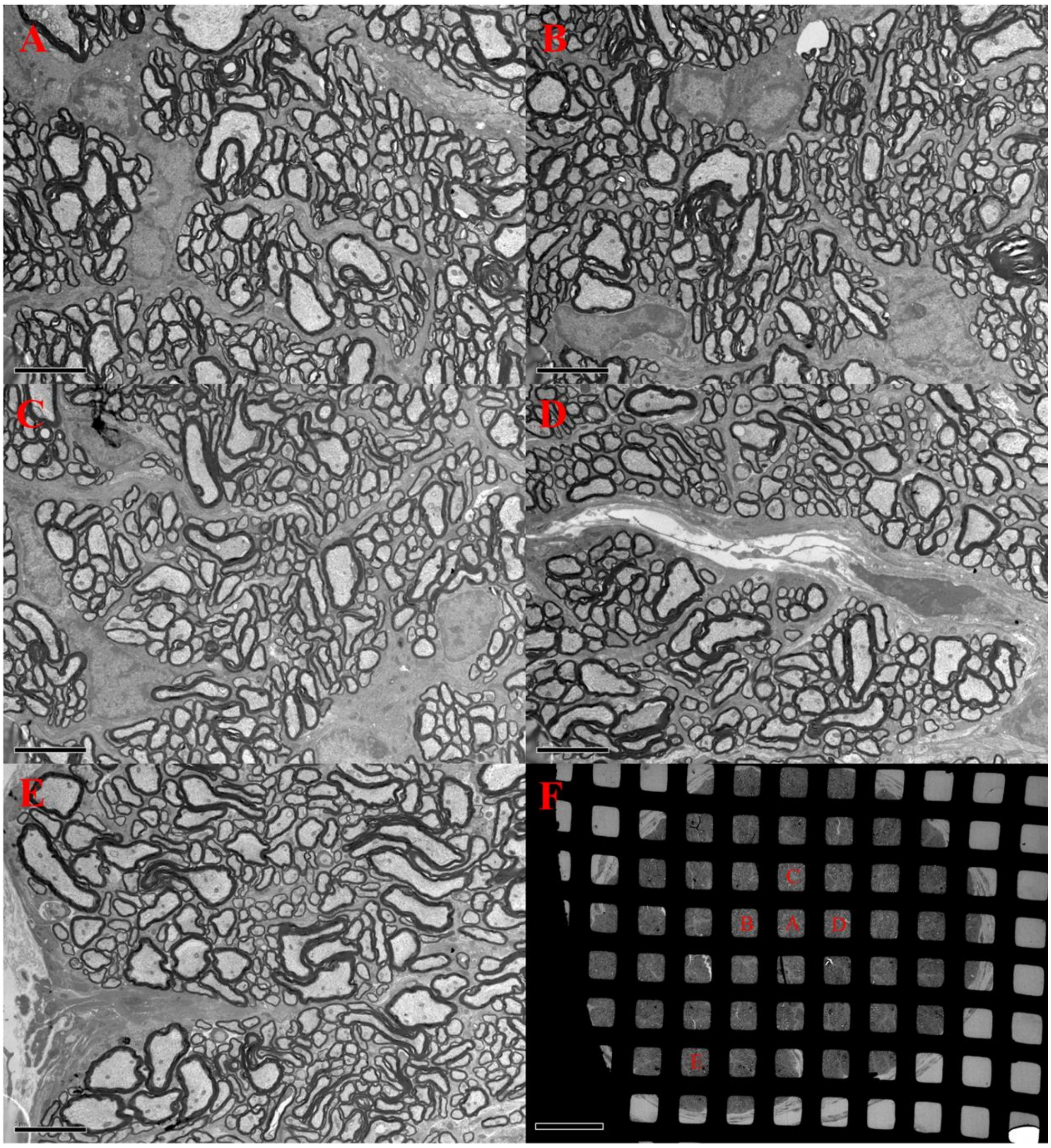

Figure 7.9.2: Appendix 1, Five Hour Maintained Nerve.

Showing transmission electron micrographs A-E, from the five hour maintained nerve. Micrographs A-D were used for sampling in section 4.0. Grid image (F) shows the position of the sample areas in relation to the whole nerve (grid is the sample support tray). Scale bars on images A-E represent 5 µm. Scale bar in panel F is 100 µm. Each grid square covers 1320 µm^2, and and each sample image covers 975 µm^2 (in order to prevent overlap with curved grid edges). The total nerve area in this sample is ~234700 µm^2. The total visible area of the nerve not obscured by the grid is 86381 µm^2 and the total area analysed in the four samples is 3900µm^2, which is 4.5% of the visible nerve area. For analysis every visible neuron (black rings) was selected and measured.

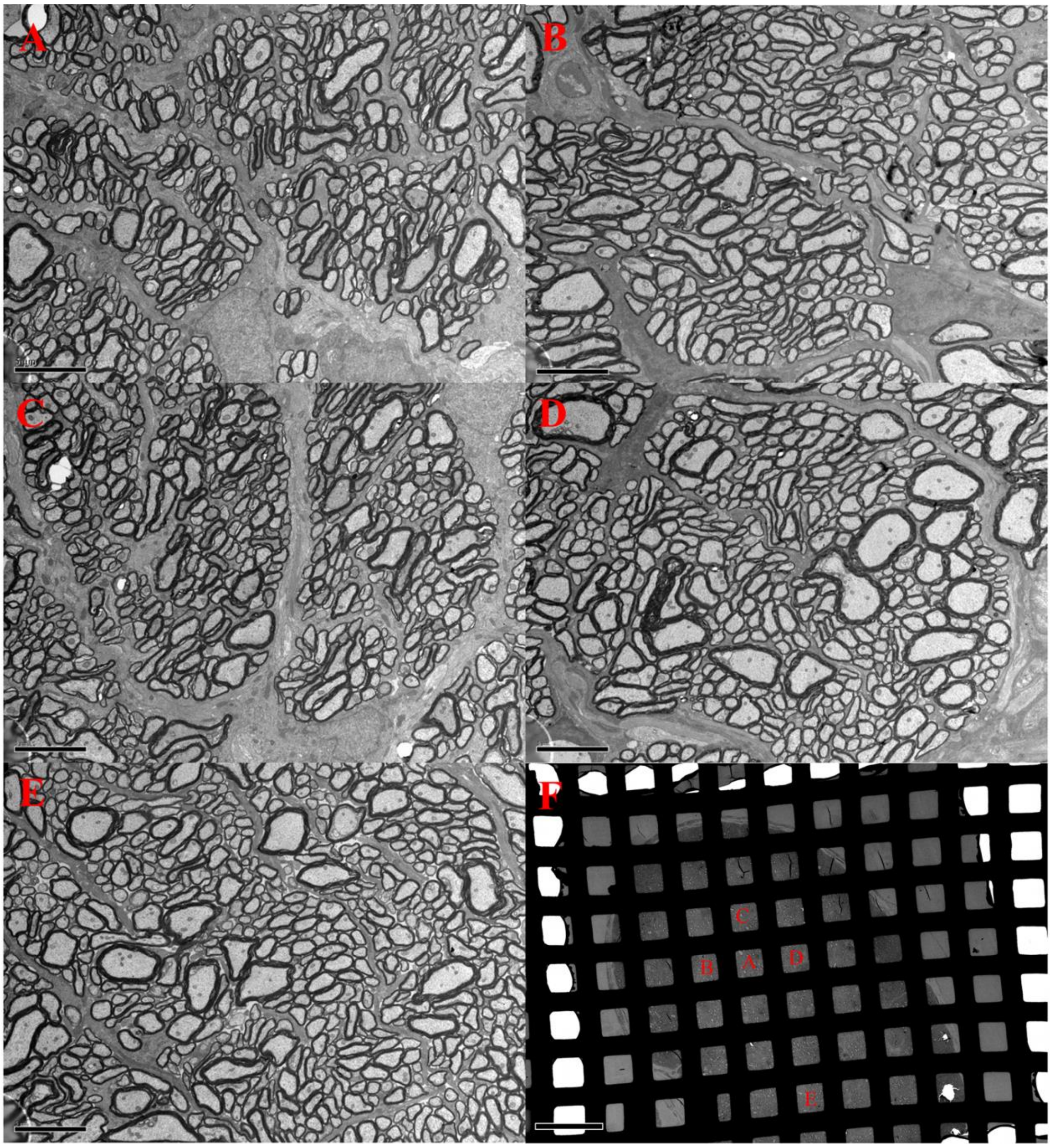

Figure 7.9.3: Appendix 1, Ten Hour Maintained Nerve.

Showing transmission electron micrographs A-E, from the ten hour maintained nerve. Micrographs A-D were used for sampling in section 4.0. Grid image (F) shows the position of the sample areas in relation to the whole nerve (grid is the sample support tray). Scale bars on images A-E represent 5 µm. Scale bar in panel F is 100 µm. Each grid square covers 1320 µm^2, and each sample image covers 975 µm^2 (in order to prevent overlap with curved grid edges). The total nerve area in this sample is ~213900 µm^2. The total visible area of the nerve not obscured by the grid is 66819 µm^2 and the total area analysed in the four samples is 3900µm^2, which is 5.8% of the visible nerve area. For analysis every visible neuron (black rings) was selected and measured.

7.10 Appendix 2

This appendix shows the full list of scan parameters from the four direction multi-compartment model fitting experiment in section 5.0 is shown below in Table 7.10.1.

Gradient Unit Directions			Parameters				
x	y	z	b-value (s/mm^2)	δ (ms)	Δ (ms)	G (T /m)	TE (ms)
0.000	0.000	0.000	0	3	35	0.00	43
0.000	1.000	0.000	2242	3	35	0.32	43
1.000	0.000	0.000	2242	3	35	0.32	43
0.707	0.707	0.000	2241	3	35	0.32	43
0.000	1.000	0.000	2838	3	35	0.36	43
1.000	0.000	0.000	2838	3	35	0.36	43
0.707	0.707	0.000	2837	3	35	0.36	43
0.000	1.000	0.000	3503	3	35	0.40	43
1.000	0.000	0.000	3503	3	35	0.40	43
0.707	0.707	0.000	3502	3	35	0.40	43
0.000	0.000	0.000	0	3	50	0.00	58
0.000	1.000	0.000	2474	3	50	0.28	58
1.000	0.000	0.000	2474	3	50	0.28	58
0.707	0.707	0.000	2473	3	50	0.28	58
0.000	1.000	0.000	3231	3	50	0.32	58
1.000	0.000	0.000	3231	3	50	0.32	58
0.707	0.707	0.000	3230	3	50	0.32	58
0.000	1.000	0.000	4090	3	50	0.36	58
1.000	0.000	0.000	4090	3	50	0.36	58
0.707	0.707	0.000	4089	3	50	0.36	58
0.000	1.000	0.000	5049	3	50	0.40	58
1.000	0.000	0.000	5049	3	50	0.40	58
0.707	0.707	0.000	5047	3	50	0.40	58
0.000	0.000	0.000	0	15	30	0.00	50
0.000	1.000	0.000	9056	15	30	0.15	50
1.000	0.000	0.000	9056	15	30	0.15	50
0.707	0.707	0.000	9054	15	30	0.15	50
0.000	0.000	0.000	0	15	40	0.00	60
0.000	1.000	0.000	8456	15	40	0.12	60
1.000	0.000	0.000	8456	15	40	0.12	60
0.707	0.707	0.000	8455	15	40	0.12	60
0.000	1.000	0.000	12679	15	40	0.15	60
1.000	0.000	0.000	12679	15	40	0.15	60
0.707	0.707	0.000	12675	15	40	0.15	60
0.000	0.000	0.000	0	3	10	0.00	18
0.000	0.000	1.000	9	3	10	0.04	18

0.000	1.000	0.000	9	3	10	0.04	18
1.000	0.000	0.000	9	3	10	0.04	18
0.707	0.707	0.000	9	3	10	0.04	18
0.000	0.000	1.000	37	3	10	0.08	18
0.000	1.000	0.000	37	3	10	0.08	18
1.000	0.000	0.000	37	3	10	0.08	18
0.707	0.707	0.000	37	3	10	0.08	18
0.000	0.000	1.000	83	3	10	0.12	18
0.000	1.000	0.000	83	3	10	0.12	18
1.000	0.000	0.000	83	3	10	0.12	18
0.707	0.707	0.000	83	3	10	0.12	18
0.000	0.000	1.000	148	3	10	0.16	18
0.000	1.000	0.000	148	3	10	0.16	18
1.000	0.000	0.000	148	3	10	0.16	18
0.707	0.707	0.000	148	3	10	0.16	18
0.000	0.000	1.000	232	3	10	0.20	18
0.000	1.000	0.000	232	3	10	0.20	18
1.000	0.000	0.000	232	3	10	0.20	18
0.707	0.707	0.000	232	3	10	0.20	18
0.000	0.000	1.000	334	3	10	0.24	18
0.000	1.000	0.000	334	3	10	0.24	18
1.000	0.000	0.000	334	3	10	0.24	18
0.707	0.707	0.000	334	3	10	0.24	18
0.000	0.000	1.000	454	3	10	0.28	18
0.000	1.000	0.000	454	3	10	0.28	18
1.000	0.000	0.000	454	3	10	0.28	18
0.707	0.707	0.000	454	3	10	0.28	18
0.000	0.000	1.000	594	3	10	0.32	18
0.000	1.000	0.000	594	3	10	0.32	18
1.000	0.000	0.000	594	3	10	0.32	18
0.707	0.707	0.000	593	3	10	0.32	18
0.000	0.000	1.000	751	3	10	0.36	18
0.000	1.000	0.000	751	3	10	0.36	18
1.000	0.000	0.000	751	3	10	0.36	18
0.707	0.707	0.000	751	3	10	0.36	18
0.000	0.000	1.000	927	3	10	0.40	18
0.000	1.000	0.000	927	3	10	0.40	18
1.000	0.000	0.000	927	3	10	0.40	18
0.707	0.707	0.000	927	3	10	0.40	18
0.000	0.000	0.000	0	3	20	0.00	28
0.000	0.000	1.000	20	3	20	0.04	28
0.000	1.000	0.000	20	3	20	0.04	28
1.000	0.000	0.000	20	3	20	0.04	28
0.707	0.707	0.000	20	3	20	0.04	28
0.000	0.000	1.000	78	3	20	0.08	28
0.000	1.000	0.000	78	3	20	0.08	28

1.000	0.000	0.000	78	3	20	0.08	28
0.707	0.707	0.000	78	3	20	0.08	28
0.000	0.000	1.000	176	3	20	0.12	28
0.000	1.000	0.000	176	3	20	0.12	28
1.000	0.000	0.000	176	3	20	0.12	28
0.707	0.707	0.000	176	3	20	0.12	28
0.000	1.000	0.000	313	3	20	0.16	28
1.000	0.000	0.000	313	3	20	0.16	28
0.707	0.707	0.000	313	3	20	0.16	28
0.000	0.000	1.000	489	3	20	0.20	28
0.000	1.000	0.000	489	3	20	0.20	28
1.000	0.000	0.000	489	3	20	0.20	28
0.707	0.707	0.000	489	3	20	0.20	28
0.000	0.000	1.000	705	3	20	0.24	28
0.000	1.000	0.000	705	3	20	0.24	28
1.000	0.000	0.000	705	3	20	0.24	28
0.707	0.707	0.000	705	3	20	0.24	28
0.000	0.000	1.000	959	3	20	0.28	28
0.000	1.000	0.000	959	3	20	0.28	28
1.000	0.000	0.000	959	3	20	0.28	28
0.707	0.707	0.000	959	3	20	0.28	28
0.000	0.000	1.000	1253	3	20	0.32	28
0.000	1.000	0.000	1253	3	20	0.32	28
1.000	0.000	0.000	1253	3	20	0.32	28
0.707	0.707	0.000	1253	3	20	0.32	28
0.000	0.000	1.000	1586	3	20	0.36	28
0.000	1.000	0.000	1586	3	20	0.36	28
1.000	0.000	0.000	1586	3	20	0.36	28
0.707	0.707	0.000	1585	3	20	0.36	28
0.000	0.000	1.000	1958	3	20	0.40	28
0.000	1.000	0.000	1958	3	20	0.40	28
1.000	0.000	0.000	1958	3	20	0.40	28
0.707	0.707	0.000	1957	3	20	0.40	28
0.000	0.000	0.000	0	3	35	0.00	43
0.000	0.000	1.000	35	3	35	0.04	43
0.000	1.000	0.000	35	3	35	0.04	43
0.707	0.707	0.000	35	3	35	0.04	43
0.000	1.000	0.000	140	3	35	0.08	43
1.000	0.000	0.000	140	3	35	0.08	43
0.707	0.707	0.000	140	3	35	0.08	43
0.000	0.000	1.000	315	3	35	0.12	43
0.000	1.000	0.000	315	3	35	0.12	43
1.000	0.000	0.000	315	3	35	0.12	43
0.707	0.707	0.000	315	3	35	0.12	43
0.000	0.000	1.000	561	3	35	0.16	43
0.000	1.000	0.000	561	3	35	0.16	43

1.000	0.000	0.000	561	3	35	0.16	43
0.707	0.707	0.000	560	3	35	0.16	43
0.000	0.000	1.000	876	3	35	0.20	43
0.000	1.000	0.000	876	3	35	0.20	43
1.000	0.000	0.000	876	3	35	0.20	43
0.707	0.707	0.000	876	3	35	0.20	43
0.000	0.000	1.000	1261	3	35	0.24	43
0.000	1.000	0.000	1261	3	35	0.24	43
1.000	0.000	0.000	1261	3	35	0.24	43
0.707	0.707	0.000	1261	3	35	0.24	43
0.000	0.000	1.000	1717	3	35	0.28	43
0.000	1.000	0.000	1717	3	35	0.28	43
1.000	0.000	0.000	1717	3	35	0.28	43
0.707	0.707	0.000	1716	3	35	0.28	43
0.000	0.000	0.000	0	3	50	0.00	58
0.000	0.000	1.000	50	3	50	0.04	58
0.000	1.000	0.000	50	3	50	0.04	58
0.707	0.707	0.000	50	3	50	0.04	58
0.000	0.000	1.000	202	3	50	0.08	58
0.000	1.000	0.000	202	3	50	0.08	58
0.707	0.707	0.000	202	3	50	0.08	58
0.000	0.000	1.000	454	3	50	0.12	58
0.000	1.000	0.000	454	3	50	0.12	58
1.000	0.000	0.000	454	3	50	0.12	58
0.707	0.707	0.000	454	3	50	0.12	58
0.000	0.000	1.000	808	3	50	0.16	58
0.000	1.000	0.000	808	3	50	0.16	58
1.000	0.000	0.000	808	3	50	0.16	58
0.707	0.707	0.000	808	3	50	0.16	58
0.000	0.000	1.000	1262	3	50	0.20	58
0.000	1.000	0.000	1262	3	50	0.20	58
1.000	0.000	0.000	1262	3	50	0.20	58
0.707	0.707	0.000	1262	3	50	0.20	58
0.000	0.000	1.000	1818	3	50	0.24	58
0.000	1.000	0.000	1818	3	50	0.24	58
1.000	0.000	0.000	1818	3	50	0.24	58
0.707	0.707	0.000	1817	3	50	0.24	58
0.000	0.000	0.000	0	15	30	0.00	50
0.000	0.000	1.000	644	15	30	0.04	50
0.000	1.000	0.000	644	15	30	0.04	50
1.000	0.000	0.000	644	15	30	0.04	50
0.707	0.707	0.000	644	15	30	0.04	50
0.000	0.000	1.000	1834	15	30	0.07	50
0.000	1.000	0.000	1834	15	30	0.07	50
1.000	0.000	0.000	1834	15	30	0.07	50
0.707	0.707	0.000	1833	15	30	0.07	50

0.000	0.000	1.000	3633	15	30	0.10	50
0.000	1.000	0.000	3633	15	30	0.10	50
1.000	0.000	0.000	3633	15	30	0.10	50
0.707	0.707	0.000	3632	15	30	0.09	50
0.000	0.000	1.000	6040	15	30	0.12	50
0.000	1.000	0.000	6040	15	30	0.12	50
1.000	0.000	0.000	6040	15	30	0.12	50
0.707	0.707	0.000	6039	15	30	0.12	50
0.000	0.000	0.000	0	15	40	0.00	60
0.000	0.000	1.000	902	15	40	0.04	60
0.000	1.000	0.000	902	15	40	0.04	60
1.000	0.000	0.000	902	15	40	0.04	60
0.707	0.707	0.000	901	15	40	0.04	60
0.000	0.000	1.000	2567	15	40	0.07	60
0.000	1.000	0.000	2567	15	40	0.07	60
1.000	0.000	0.000	2567	15	40	0.07	60
0.707	0.707	0.000	2567	15	40	0.07	60
0.000	0.000	1.000	5086	15	40	0.10	60
0.000	1.000	0.000	5086	15	40	0.10	60
1.000	0.000	0.000	5086	15	40	0.10	60
0.707	0.707	0.000	5085	15	40	0.09	60

Table 7.10.1: Appendix 2: Scan Parameters from Experiment B.

Showing a full list of scan parameters used in the multi-direction-multi-b-value experiment B described in section 5.0.

Bibliography

1. Aisen, A. M., Martel, W., Braunstein, E. M., McMillin, K. I., Phillips, W. A. & Kling, T. F. MRI and CT evaluation of primary bone and soft-tissue tumors. *Am. J. Roentgenol.* **146**, 749–756 (1986).
2. Hahn, E. L. Spin Echoes. *Phys. Rev.* **80**, 580 (1950).
3. Carr, H. & Purcell, E. Effects of Diffusion on Free Precession in Nuclear Magnetic Resonance Experiments. *Phys. Rev.* **94**, 630–638 (1954).
4. Stejskal, E. & Tanner, J. Spin Diffusion Measurements: Spin Echoes in the Presence of a Time-Dependent Field Gradient. *J. Chem. Phys.* **42**, 288–292 (1965).
5. Beaulieu, C. The basis of anisotropic water diffusion in the nervous system – a technical review. *NMR Biomed.* **15**, 435–455 (2002).
6. Basser, P. J., Mattiello, J. & LeBihan, D. MR diffusion tensor spectroscopy and imaging. *Biophys. J.* **66**, 259–267 (1994).
7. Blackband, S. J., Bui, J. D., Buckley, D. L., Zelles, T., Plant, H. D., Inglis, B. A. & Phillips, M. I. MR microscopy of perfused brain slices. *Magn. Reson. Med.* **38**, 1012–1015 (1997).
8. Smith, T. B. & Nayak, K. S. MRI artifacts and correction strategies. *Imaging Med.* **2**, 445–457 (2010).
9. Richardson, S., Siow, B., Batchelor, A. M., Lythgoe, M. F. & Alexander, D. C. A viable isolated tissue system: A tool for detailed MR measurements and controlled perturbation in physiologically stable tissue. *Magn. Reson. Med.* **69**, 1603–1610 (2013).
10. Richardson, S., Siow, B., Panagiotaki, E., Schneider, T., Lythgoe, M. F. & Alexander, D. C. Viable and fixed white matter: Diffusion magnetic resonance comparisons and contrasts at physiological temperature. *Magn. Reson. Med.* n/a–n/a (2013).doi:10.1002/mrm.25012
11. Alberts, B. *Molecular biology of the cell*. (Garland Science, 2000).
12. Bear, M. F. *Neuroscience: exploring the brain*. (Lippincott Williams & Wilkins, 2007).
13. Edgar, J. M. & Griffiths, R. I.in *Diffus. MRI Quant. Meas. -Vivo Neuroanat.* (Academic Press, 2009).
14. Johansen-Berg, H. & Timothy E.J. Behrens *Diffusion MRI from quantitative measurement to in-vivo neuroanatomy*. (Academic Press, 2009).
15. Peters, A., Palay, S. L. & Webster, H. deF *The fine structure of the nervous system: neurons and supporting cells*. (Oxford University Press, 1991).
16. Sofroniew, M. V. & Vinters, H. V. Astrocytes: biology and pathology. *Acta Neuropathol. (Berl.)* **119**, 7–35 (2010).
17. Gourine, A. V. & Kasparov, S. Astrocytes as brain interoceptors. *Exp. Physiol.* **96**, 411–416 (2011).
18. Raivich, G. Like cops on the beat: the active role of resting microglia. *Trends Neurosci.* **28**, 571–573 (2005).
19. Roguin, A. Nikola Tesla: The man behind the magnetic field unit. *J. Magn. Reson. Imaging* **19**, 369–374 (2004).
20. Rabi, I. I., Millman, S., Kusch, P. & Zacharias, J. R. The Molecular Beam Resonance Method for Measuring Nuclear Magnetic Moments. The Magnetic Moments of 3 Li^6,3 Li^7 and 9 F^{19}. *Phys. Rev.* **55**, 526 (1939).

21. Bloch, F. Nuclear induction. *Phys. Rev.* **70**, 460 (1946).
22. Purcell, E. M., Torrey, H. C. & Pound, R. V. Resonance absorption by nuclear magnetic moments in a solid. *Phys. Rev.* **69**, 37 (1946).
23. Damadian, R. Tumor detection by nuclear magnetic resonance. *Science* **171**, 1151–1153 (1971).
24. Lauterbur, P. C. Image formation by induced local interactions: examples employing nuclear magnetic resonance. *Nature* **242**, 190–191 (1973).
25. Mansfield, P. & Grannell, P. K. NMR'diffraction'in solids? *J. Phys. C Solid State Phys.* **6**, L422 (1973).
26. Hounsfield, G. N. Computerized transverse axial scanning (tomography): Part I. Description of system. 1973. *Br. J. Radiol.* **68**, H166 (1995).
27. Ambrose, J. Computerized transverse axial scanning (tomography): Part 2, clinical application. (1973).
28. Kumar, A., Welti, D. & Ernst, R. R. NMR Fourier zeugmatography. *J. Magn. Reson. 1969* **18**, 69–83 (1975).
29. Mansfield, P. & Maudsley, A. A. Medical imaging by NMR. *Br. J. Radiol.* **50**, 188–194 (1977).
30. Edelstein, W. A., Hutchison, J. M. S., Johnson, G. & Redpath, T. W. Spin warp NMR imaging and applications to human whole-body imaging. *Phys. Med. Biol.* **25**, 751 (1980).
31. Mansfield, P. Multi-planar image formation using NMR spin echoes. *J. Phys. C Solid State Phys.* **10**, L55 (1977).
32. Mansfield, P. & Pykett, I. L. Biological and medical imaging by NMR. *J. Magn. Reson. 1969* **29**, 355–373 (1978).
33. McRobbie, D. W. *MRI from picture to proton*. (Cambridge University Press, 2007).
34. Gallagher, T. A., Nemeth, A. J. & Hacein-Bey, L. An introduction to the Fourier Transform: relationship to MRI. *Am. J. Roentgenol.* **190**, 1396–1405 (2008).
35. Hodgkin, A. *The conduction of the nervous impulse*. (Liverpool University Press, 1971).
36. Einstein, A. Über die von der molekularkinetischen Theorie der Wärme geforderte Bewegung von in ruhenden Flüssigkeiten suspendierten Teilchen. *Ann. Phys.* **322**, 549–560 (1905).
37. Assaf, Y. & Cohen, Y.in *Diffus. MRI Quant. Meas. -Vivo Neuroanat.* (Academic Press, 2009).
38. Song, S.-K., Sun, S.-W., Ju, W.-K., Lin, S.-J., Cross, A. H. & Neufeld, A. H. Diffusion tensor imaging detects and differentiates axon and myelin degeneration in mouse optic nerve after retinal ischemia. *NeuroImage* **20**, 1714–1722 (2003).
39. Raine, C. S.in *Myelin* 1–50 (Springer, 1984).
40. Garthwaite, G., Brown, G., Batchelor, A. M., Goodwin, D. A. & Garthwaite, J. Mechanisms of ischaemic damage to central white matter axons: a quantitative histological analysis using rat optic nerve. *Neuroscience* **94**, 1219–1230 (1999).
41. Luby-Phelps, K. Cytoarchitecture and physical properties of cytoplasm: volume, viscosity, diffusion, intracellular surface area. *Int. Rev. Cytol.* **192**, 189–221 (1999).
42. Verkman, A. S. Solute and macromolecule diffusion in cellular aqueous compartments. *Trends Biochem. Sci.* **27**, 27–33 (2002).
43. Alberts, B., Johnson, A., Lewis, J., Raff, M., Roberts, K. & Walter, P.in *Mol. Biol. Cell* (Garland Science, 2002).

44. Syková, E. & Nicholson, C. Diffusion in Brain Extracellular Space. *Physiol. Rev.* **88**, 1277–1340 (2008).
45. Niendorf, T., Dijkhuizen, R. M., Norris, D. G., van Lookeren Campagne, M. & Nicolay, K. Biexponential diffusion attenuation in various states of brain tissue: Implications for diffusion-weighted imaging. *Magn. Reson. Med.* **36**, 847–857 (1996).
46. Assaf, Y. & Cohen, Y. Non-Mono-Exponential Attenuation of Water andN-Acetyl Aspartate Signals Due to Diffusion in Brain Tissue. *J. Magn. Reson.* **131**, 69–85 (1998).
47. Assaf, Y. & Cohen, Y. Assignment of the water slow-diffusing component in the central nervous system using q-space diffusion MRS: Implications for fiber tract imaging. *Magn. Reson. Med.* **43**, 191–199 (2000).
48. Beaulieu, C. & Allen, P. S. Determinants of anisotropic water diffusion in nerves. *Magn. Reson. Med.* **31**, 394–400 (2005).
49. Sehy, J. V., Zhao, L., Xu, J., Rayala, H. J., Ackerman, J. J. H. & Neil, J. J. Effects of physiologic challenge on the ADC of intracellular water in the Xenopus oocyte. *Magn. Reson. Med.* **52**, 239–247 (2004).
50. Woodhams, R., Matsunaga, K., Iwabuchi, K., Kan, S., Hata, H., Kuranami, M., Watanabe, M. & Hayakawa, K. Diffusion-Weighted Imaging of Malignant Breast Tumors: The Usefulness of Apparent Diffusion Coefficient (ADC) Value and ADC Map for the Detection of Malignant Breast Tumors and Evaluation of Cancer Extension. *J. Comput. Assist. Tomogr.* **29**, (2005).
51. Valsasina, P., Rocca, M., Agosta, F., Benedetti, B., Horsfield, M., Gallo, A., Rovaris, M., Comi, G. & Filippi, M. Mean diffusivity and fractional anisotropy histogram analysis of the cervical cord in MS patients. *NeuroImage* **26**, 822–828 (2005).
52. Basser, P. J. Inferring microstructural features and the physiological state of tissues from diffusion-weighted images. *NMR Biomed.* **8**, 333–344 (1995).
53. Panagiotaki, E., Schneider, T., Siow, B., Hall, M. G., Lythgoe, M. F. & Alexander, D. C. Compartment models of the diffusion MR signal in brain white matter: A taxonomy and comparison. *NeuroImage* **59**, 2241–2254 (2012).
54. Behrens, T. E. J., Woolrich, M. W., Jenkinson, M., Johansen-Berg, H., Nunes, R. G., Clare, S., Matthews, P. M., Brady, J. M. & Smith, S. M. Characterization and propagation of uncertainty in diffusion-weighted MR imaging. *Magn. Reson. Med.* **50**, 1077–1088 (2003).
55. Barazany, D., Basser, P. J. & Assaf, Y. In vivo measurement of axon diameter distribution in the corpus callosum of rat brain. *Brain* **132**, 1210–1220 (2009).
56. Stanisz, G. J., Wright, G. A., Henkelman, R. M. & Szafer, A. An analytical model of restricted diffusion in bovine optic nerve. *Magn. Reson. Med.* **37**, 103–111 (1997).
57. Alexander, D. C. A general framework for experiment design in diffusion MRI and its application in measuring direct tissue-microstructure features. *Magn. Reson. Med.* **60**, 439–448 (2008).
58. Perrin, M., Poupon, C., Rieul, B., Leroux, P., Constantinesco, A., Mangin, J.-F. & LeBihan, D. Validation of q-ball imaging with a diffusion fibre-crossing phantom on a clinical scanner. *Philos. Trans. R. Soc. B Biol. Sci.* **360**, 881–891 (2005).
59. Lin, C.-P., Wedeen, V. J., Chen, J.-H., Yao, C. & Tseng, W.-Y. I. Validation of diffusion spectrum magnetic resonance imaging with manganese-enhanced rat optic tracts and ex vivo phantoms. *NeuroImage* **19**, 482–495 (2003).

60. Avram, L., Assaf, Y. & Cohen, Y. The effect of rotational angle and experimental parameters on the diffraction patterns and micro-structural information obtained from q-space diffusion NMR: implication for diffusion in white matter fibers. *J. Magn. Reson.* **169**, 30–38 (2004).
61. Siow, B., Drobnjak, I., Chatterjee, A., Lythgoe, M. F. & Alexander, D. C. Estimation of pore size in a microstructure phantom using the optimised gradient waveform diffusion weighted NMR sequence. *J. Magn. Reson.* **214**, 51–60 (2012).
62. Dyrby, T. B., Baaré, W. F. C., Alexander, D. C., Jelsing, J., Garde, E. & Søgaard, L. V. An ex vivo imaging pipeline for producing high-quality and high-resolution diffusion-weighted imaging datasets. *Hum. Brain Mapp.* 544–563 (2011).doi:10.1002/hbm.21043
63. Shepherd, T. M., Thelwall, P. E., Stanisz, G. J. & Blackband, S. J. Aldehyde fixative solutions alter the water relaxation and diffusion properties of nervous tissue. *Magn. Reson. Med.* **62**, 26–34 (2009).
64. Alexander, D. C., Hubbard, P. L., Hall, M. G., Moore, E. A., Ptito, M., Parker, G. J. M. & Dyrby, T. B. Orientationally invariant indices of axon diameter and density from diffusion MRI. *NeuroImage* **52**, 1374–1389 (2010).
65. Shepherd, T. M., Scheffler, B., King, M. A., Stanisz, G. J., Steindler, D. A. & Blackband, S. J. MR microscopy of rat hippocampal slice cultures: A novel model for studying cellular processes and chronic perturbations to tissue microstructure. *NeuroImage* **30**, 780–786 (2006).
66. Stys, P. K., Ransom, B. R., Waxman, S. G. & Davis, P. K. Role of extracellular calcium in anoxic injury of mammalian central white matter. *Proc. Natl. Acad. Sci.* **87**, 4212–4216 (1990).
67. Anderson, A. W., Zhong, J., Petroff, O. A., Szafer, A., Ransom, B. R., Prichard, J. W. & Gore, J. C. Effects of osmotically driven cell volume changes on diffusion-weighted imaging of the rat optic nerve. *Magn. Reson. Med.* **35**, 162–167 (1996).
68. Biton, I. E., Mayk, A., Assaf, Y. & Cohen, Y. Structural changes in glutamate cell swelling followed by multiparametric q-space diffusion MR of excised rat spinal cord. *Magn. Reson. Imaging* **22**, 661–672 (2004).
69. Hsu, E. W., Buckley, D. L., Bui, J. D., Blackband, S. J. & Forder, J. R. Two-component diffusion tensor MRI of isolated perfused hearts. *Magn. Reson. Med.* **45**, 1039–1045 (2001).
70. Assaf, Y., Blumenfeld-Katzir, T., Yovel, Y. & Basser, P. J. Axcaliber: A method for measuring axon diameter distribution from diffusion MRI. *Magn. Reson. Med.* **59**, 1347–1354 (2008).
71. Shepherd, T. M., Flint, J. J., Thelwall, P. E., Stanisz, G. J., Mareci, T. H., Yachnis, A. T. & Blackband, S. J. Postmortem interval alters the water relaxation and diffusion properties of rat nervous tissue - Implications for MRI studies of human autopsy samples. *NeuroImage* **44**, 820–826 (2009).
72. Madi, S., Hasan, K. M. & Narayana, P. A. Diffusion tensor imaging of in vivo and excised rat spinal cord at 7 T with an icosahedral encoding scheme. *Magn. Reson. Med.* **53**, 118–125 (2005).
73. Pattany, P. M., Puckett, W. R., Klose, K. J., Quencer, R. M., Bunge, R. P., Kasuboski, L. & Weaver, R. G. High-resolution diffusion-weighted MR of fresh and fixed cat spinal cords: evaluation of diffusion coefficients and anisotropy. *Am. J. Neuroradiol.* **18**, 1049–56 (1997).

74. Harris, K. R. & Woolf, L. A. Pressure and temperature dependence of the self diffusion coefficient of water and oxygen-18 water. *J Chem Soc Faraday Trans 1* **76**, 377–385 (1980).
75. Thelwall, P. E., Shepherd, T. M., Stanisz, G. J. & Blackband, S. J. Effects of temperature and aldehyde fixation on tissue water diffusion properties, studied in an erythrocyte ghost tissue model. *Magn. Reson. Med.* **56**, 282–289 (2006).
76. Alberts, B.in *Mol. Biol. Cell* (Garland Science, 2002).
77. Hodgkin, A. L. The Croonian Lecture: Ionic movements and electrical activity in giant nerve fibres. *Proc. R. Soc. Lond. B Biol. Sci.* **148**, 1–37 (1958).
78. Humphrey, D. & Schmidt, E.in *Neurophysiol. Tech.* (Boulton, A., Baker, G. & Vanderwolf, C.) **15**, 1–64 (Humana Press, 1991).
79. Erlanger, J. & Gasser, H. S. *Electrical signs of nervous activity*. (University Press, 1937).
80. Ogawa, S., Lee, T.-M., Nayak, A. S. & Glynn, P. Oxygenation-sensitive contrast in magnetic resonance image of rodent brain at high magnetic fields. *Magn. Reson. Med.* **14**, 68–78 (1990).
81. Biswal, B., Zerrin Yetkin, F., Haughton, V. M. & Hyde, J. S. Functional connectivity in the motor cortex of resting human brain using echo-planar mri. *Magn. Reson. Med.* **34**, 537–541 (1995).
82. Logothetis, N. K. & Pfeuffer, J. On the nature of the BOLD fMRI contrast mechanism. *Proc. Int. Sch. Magn. Reson. Brain Funct. Front. Brain Funct. MRI Electrophysiol. Methods Proc. Int. Sch. Magn. Reson. Brain Funct.* **22**, 1517–1531 (2004).
83. Arthurs, O. J. & Boniface, S. How well do we understand the neural origins of the fMRI BOLD signal? *TRENDS Neurosci.* **25**, 27–31 (2002).
84. Ogawa, S., Tank, D. W., Menon, R., Ellermann, J. M., Kim, S.-G., Merkle, H. & Ugurbil, K. Intrinsic signal changes accompanying sensory stimulation: functional brain mapping with magnetic resonance imaging. *Proc. Natl. Acad. Sci.* **89**, 5951–5955 (1992).
85. Tettamanti, M., Paulesu, E., Scifo, P., Maravita, A., Fazio, F., Perani, D. & Marzi, C. A. Interhemispheric transmission of visuomotor information in humans: fMRI evidence. *J. Neurophysiol.* **88**, 1051–1058 (2002).
86. Mazerolle, E. L., D'Arcy, R. C. & Beyea, S. D. Detecting functional magnetic resonance imaging activation in white matter: Interhemispheric transfer across the corpus callosum. *BMC Neurosci.* **9**, 84 (2008).
87. Mazerolle, E. L., Beyea, S. D., Gawryluk, J. R., Brewer, K. D., Bowen, C. V. & D'Arcy, R. C. N. Confirming white matter fMRI activation in the corpus callosum: Co-localization with DTI tractography. *NeuroImage* **50**, 616–621 (2010).
88. Logothetis, N. K. & Wandell, B. A. Interpreting the BOLD signal. *Annu Rev Physiol* **66**, 735–769 (2004).
89. Kim, S.-G., Richter, W. & Uğurbil, K. Limitations of temporal resolution in functional MRI. *Magn. Reson. Med.* **37**, 631–636 (1997).
90. Aguirre, G. K., Zarahn, E. & D'Esposito, M. The Variability of Human, BOLD Hemodynamic Responses. *NeuroImage* **8**, 360–369 (1998).
91. Aguirre, G. K., Detre, J. A., Zarahn, E. & Alsop, D. C. Experimental Design and the Relative Sensitivity of BOLD and Perfusion fMRI. *NeuroImage* **15**, 488–500 (2002).

92. Gawryluk, J. R., Brewer, K. D., Beyea, S. D. & D'Arcy, R. C. N. Optimizing the detection of white matter fMRI using asymmetric spin echo spiral. *NeuroImage* **45**, 83–88 (2009).
93. Logothetis, N. K., Pauls, J., Augath, M., Trinath, T. & Oeltermann, A. Neurophysiological investigation of the basis of the fMRI signal. *Nature* **412**, 150–157 (2001).
94. Lipton, P. Effects of membrane depolarization on light scattering by cerebral cortical slices. *J. Physiol.* **231**, 365–383 (1973).
95. Andrew, R. D. & Macvicar, B. A. Imaging cell volume changes and neuronal excitation in the hippocampal slice. *Neuroscience* **62**, 371–383 (1994).
96. Ransom, B. R., Yamate, C. L. & Connors, B. W. Activity-dependent shrinkage of extracellular space in rat optic nerve: a developmental study. *J. Neurosci.* **5**, 532–535 (1985).
97. Van Harreveld, A. The extracellular space in the vertebrate central nervous system. *Struct. Funct. Nerv. Tissue* **4**, 447–511 (1972).
98. Lang, F. Mechanisms and significance of cell volume regulation. *J. Am. Coll. Nutr.* **26**, 613S–623S (2007).
99. Heinemann, U. & Dieter Lux, H. Ceiling of stimulus induced rises in extracellular potassium concentration in the cerebral cortex of cat. *Brain Res.* **120**, 231–249 (1977).
100. Barnett, M. W. & Larkman, P. M. The action potential. *Pract. Neurol.* **7**, 192–197 (2007).
101. Connors, B. W., Ransom, B. R., Kunis, D. M. & Gutnick, M. J. Activity-dependent K+ accumulation in the developing rat optic nerve. *Science* **216**, 1341–1343 (1982).
102. Kofuji, P. & Newman, E. A. Potassium buffering in the central nervous system. *Brain Water Homeost.* **129**, 1043–1054 (2004).
103. Bourke, R. S., Daze, M. A. & Kimelberg, H. K. Chloride transport in mammalian astroglia. *Dyn. Prop. Glial Cells Pergamon Press Ltd* 337–346 (1978).
104. Kraig, R. P., Ferreira-Filho, C. R. & Nicholson, C. Alkaline and acid transients in cerebellar microenvironment. *J. Neurophysiol.* **49**, 831–850 (1983).
105. Kimelberg, H. K. Glial enzymes and ion transport in brain swelling. *Neural Trauma* 137–153 (1979).
106. Le Bihan, D., Urayama, S., Aso, T., Hanakawa, T. & Fukuyama, H. Direct and fast detection of neuronal activation in the human brain with diffusion MRI. *Proc. Natl. Acad. Sci.* **103**, 8263 –8268 (2006).
107. Miller, K. L., Bulte, D. P., Devlin, H., Robson, M. D., Wise, R. G., Woolrich, M. W., Jezzard, P. & Behrens, T. E. J. Evidence for a vascular contribution to diffusion FMRI at high b value. *Proc. Natl. Acad. Sci.* **104**, 20967–20972 (2007).
108. Rudrapatna, U. S., van der Toorn, A., van Meer, M. P. A. & Dijkhuizen, R. M. Impact of hemodynamic effects on diffusion-weighted fMRI signals. *NeuroImage* **61**, 106–114 (2012).
109. Mandl, R., Schnack, H., Zwiers, M., van der Schaaf, A., Kahn, R. & Hulshoff Functional Diffusion Tensor Imaging: Measuring Task-Related Fractional Anisotropy Changes in the Human Brain along White Matter Tracts. *PLoS ONE* **3**, e3631 (2008).

110. Gulani, V., Iwamoto, G. A. & Lauterbur, P. C. Apparent water diffusion measurements in electrically stimulated neural tissue. *Magn. Reson. Med.* **41**, 241–246 (1999).
111. Spees, W. M., Lin, T.-H. & Song, S.-K. White-matter diffusion fMRI of mouse optic nerve. *NeuroImage* **65**, 209–215 (2013).
112. Hull, C. W. Apparatus for production of three-dimensional objects by stereolithography. (1986).
113. Garthwaite, J. & Batchelor, A. M. A biplanar slice preparation for studying cerebellar synaptic transmission. *J. Neurosci. Methods* **64**, 189–197 (1996).
114. Schenck, J. F. The role of magnetic susceptibility in magnetic resonance imaging: MRI magnetic compatibility of the first and second kinds. *Med. Phys.* **23**, 815–850 (1996).
115. Fern, R., Davis, P., Waxman, S. G. & Ransom, B. R. Axon Conduction and Survival in CNS White Matter During Energy Deprivation: A Developmental Study. *J. Neurophysiol.* **79**, 95–105 (1998).
116. De Juan, J., Iñiguez, C. & Carreres, J. Number, diameter and distribution of the rat optic nerve fibers. *Cells Tissues Organs* **102**, 294–299 (1978).
117. Feinberg, D. A., Hoenninger, J. C., Crooks, L. E., Kaufman, L., Watts, J. C. & Arakawa, M. Inner volume MR imaging: technical concepts and their application. *Radiology* **156**, 743–747 (1985).
118. Cook, P., Bai, Y., Gilani, N., Seunarine, K., Hall, M., Parker, G. & Alexander, D. Camino: Open-Source Diffusion-MRI Reconstruction and Processing. in *Proc. 14th Annu. Meet. ISMRM* 2759 (2006).
119. Alexander, D. C. & Barker, G. J. Optimal imaging parameters for fiber-orientation estimation in diffusion MRI. *NeuroImage* **27**, 357–367 (2005).
120. Stys, P. K. & Lesiuk, H. Correlation between electrophysiological effects of mexiletine and ischemic protection in central nervous system white matter. *Neuroscience* **71**, 27–36 (1996).
121. Field, J., Fuhrman, F. A. & Martin, A. W. Effect of Temperature on the Oxygen Consumption of Brain Tissue. *J. Neurophysiol.* **7**, 117 –126 (1944).
122. Garthwaite, G., Goodwin, D. A., Batchelor, A. M., Leeming, K. & Garthwaite, J. Nitric oxide toxicity in CNS white matter: an in vitro study using rat optic nerve. *Neuroscience* **109**, 145–155 (2002).
123. Portnoy, S. & Stanisz, G. J. Modeling pulsed magnetization transfer. *Magn. Reson. Med.* **58**, 144–155 (2007).
124. Jones, D. K. & Basser, P. J. 'Squashing peanuts and smashing pumpkins': How noise distorts diffusion-weighted MR data. *Magn. Reson. Med.* **52**, 979–993 (2004).
125. Student The Probable Error of a Mean. *Biometrika* **6**, 1–25 (1908).
126. Marquardt, D. W. An algorithm for least-squares estimation of nonlinear parameters. *J. Soc. Ind. Appl. Math.* **11**, 431–441 (1963).
127. Alexander, D. C.in *Vis. Process. Tensor Fields* (Laidlaw, D. & Weickert, J.) 3–20 (Springer Berlin Heidelberg, 2009).
128. Schwarz, G. Estimating the Dimension of a Model. *Ann. Stat.* **6**, 461–464 (1978).
129. Clark, C. A. & Le Bihan, D. Water diffusion compartmentation and anisotropy at high b values in the human brain. *Magn. Reson. Med.* **44**, 852–859 (2000).
130. Hui, E. S., Cheung, M. M., Chan, K. C. & Wu, E. X. B-value dependence of DTI quantitation and sensitivity in detecting neural tissue changes. *Neuroimage* **49**, 2366 (2010).

131. Le Bihan, D., Turner, R. & Douek, P. Is water diffusion restricted in human brain white matter? An echo-planar NMR imaging study. *Neuroreport* **4**, 887–890 (1993).
132. Clark, C. A., Hedehus, M. & Moseley, M. E. Diffusion time dependence of the apparent diffusion tensor in healthy human brain and white matter disease. *Magn. Reson. Med.* **45**, 1126–1129 (2001).
133. Holz, M., Heil, S. R. & Sacco, A. Temperature-dependent self-diffusion coefficients of water and six selected molecular liquids for calibration in accurate 1H NMR PFG measurements. *Phys. Chem. Chem. Phys.* **2**, 4740–4742 (2000).
134. Le Bihan, D. Looking into the functional architecture of the brain with diffusion MRI. *Nat Rev Neurosci* **4**, 469–480 (2003).
135. Einstein, A. Über die von der molekularkinetischen Theorie der Wärme geforderte Bewegung von in ruhenden Flüssigkeiten suspendierten Teilchen. *Ann. Phys.* **322**, 549–560 (1905).
136. Schachter, M., Does, M. D., Anderson, A. W. & Gore, J. C. Measurements of Restricted Diffusion Using an Oscillating Gradient Spin-Echo Sequence. *J. Magn. Reson.* **147**, 232–237 (2000).
137. Merboldt, K.-D., Hänicke, W. & Frahm, J. Diffusion imaging using stimulated echoes. *Magn. Reson. Med.* **19**, 233–239 (1991).
138. Zhou, F.-L., Hubbard, P. L., Eichhorn, S. J. & Parker, G. J. M. Coaxially Electrospun Axon-Mimicking Fibers for Diffusion Magnetic Resonance Imaging. *ACS Appl. Mater. Interfaces* **4**, 6311–6316 (2012).
139. Farrell, J. A. D., Landman, B. A., Jones, C. K., Smith, S. A., Prince, J. L., van Zijl, P. C. M. & Mori, S. Effects of signal-to-noise ratio on the accuracy and reproducibility of diffusion tensor imaging–derived fractional anisotropy, mean diffusivity, and principal eigenvector measurements at 1.5T. *J. Magn. Reson. Imaging* **26**, 756–767 (2007).
140. Jones, D. K. & Cercignani, M. Twenty-five pitfalls in the analysis of diffusion MRI data. *NMR Biomed.* **23**, 803–820 (2010).
141. Stanisz, G. J. & Henkelman, R. M. Diffusional anisotropy of T2 components in bovine optic nerve. *Magn. Reson. Med.* **40**, 405–410 (1998).
142. Dula, A. N., Gochberg, D. F., Valentine, H. L., Valentine, W. M. & Does, M. D. Multiexponential T2, magnetization transfer, and quantitative histology in white matter tracts of rat spinal cord. *Magn. Reson. Med.* **63**, 902–909 (2010).
143. Panagiotaki, E. Geometric models of brain white matter for microstructure imaging with diffusion MRI. (2011).
144. Emeis, D., Anker, W. & Wittern, K.-P. Quantitative 13C NMR spectroscopic studies on the equilibrium of formaldehyde with its releasing cosmetic preservatives. *Anal. Chem.* **79**, 2096–2100 (2007).
145. SCCS (Scientific Committee on Consumer Safety) Opinion on methylene glycol. (2012).
146. Kiernan, J. A. *Histological and histochemical methods : theory and practice*. (Scion, 2008).
147. Jones, D. Reactions of aldehydes with unsaturated fatty acids during histological fixation. *Histochem. J.* **4**, 421–465 (1972).
148. Van Harreveld, A. & Khattab, F. I. Chloride movements during perfusion fixation with glutaraldehyde. *Anat. Rec.* **162**, 467–477 (1968).
149. Heyderman, E. Histotechnology. A self-instructional text. *Histopathology* **20**, 91–91 (1992).

150. Denk, W. & Horstmann, H. Serial block-face scanning electron microscopy to reconstruct three-dimensional tissue nanostructure. *PLoS Biol.* **2**, e329 (2004).
151. Hildebrand, C. & Hahn, R. Relation between myelin sheath thickness and axon size in spinal cord white matter of some vertebrate species. *J. Neurol. Sci.* **38**, 421–434 (1978).
152. Gur, R. C., Turetsky, B. I., Matsui, M., Yan, M., Bilker, W., Hughett, P. & Gur, R. E. Sex Differences in Brain Gray and White Matter in Healthy Young Adults: Correlations with Cognitive Performance. *J. Neurosci.* **19**, 4065–4072 (1999).
153. Paus, T., Collins, D. ., Evans, A. ., Leonard, G., Pike, B. & Zijdenbos, A. Maturation of white matter in the human brain: a review of magnetic resonance studies. *Brain Res. Bull.* **54**, 255–266 (2001).
154. Stys, P. K., Ransom, B. R. & Waxman, S. G. Compound action potential of nerve recorded by suction electrode: a theoretical and experimental analysis. *Brain Res.* **546**, 18–32 (1991).
155. Dettbarn, W.-D.in *Neuropoisons* (Simpson, L.) 169–186 (Springer US, 1995).at <http://dx.doi.org/10.1007/978-1-4684-2940-4_8>
156. Walz, W. & Mukerji, S. KCl movements during potassium-induced cytotoxic swelling of cultured astrocytes. *Exp. Neurol.* **99**, 17–29 (1988).
157. Filosa, J. A. & Blanco, V. M. Neurovascular coupling in the mammalian brain. *Exp. Physiol.* **92**, 641–646 (2007).
158. Cauli, B. & Hamel, E. Revisiting the role of neurons in neurovascular coupling. *Front. Neuroenergetics* **2**, (2010).
159. Calcinaghi, N., Wyss, M. T., Jolivet, R., Singh, A., Keller, A. L., Winnik, S., Fritschy, J.-M., Buck, A., Matter, C. M. & Weber, B. Multimodal Imaging in Rats Reveals Impaired Neurovascular Coupling in Sustained Hypertension. *Stroke* **44**, 1957–1964 (2013).
160. Tirosh, N. & Nevo, U. Neuronal activity significantly reduces water displacement: DWI of a vital rat spinal cord with no hemodynamic effect. *Neuroimage* **76**, 98–107 (2013).
161. Hoult, D. . & Richards, R. . The signal-to-noise ratio of the nuclear magnetic resonance experiment. *J. Magn. Reson. 1969* **24**, 71–85 (1976).
162. Fenno, L., Yizhar, O. & Deisseroth, K. The development and application of optogenetics. *Annu. Rev. Neurosci.* **34**, 389–412 (2011).
163. Petropoulos, A. E., Schaffer, B. K., Cheney, M. L., Enochs, S., Zimmer, C. & Weissleder, R. MR imaging of neuronal transport in the guinea pig facial nerve: initial findings. *Acta Otolaryngol. (Stockh.)* **115**, 512–516 (1995).
164. Johansen-Berg, H. & Behrens, T. E. Just pretty pictures? What diffusion tractography can add in clinical neuroscience. *Curr. Opin. Neurol.* **19**, 379 (2006).
165. Fillard, P., Descoteaux, M., Goh, A., Gouttard, S., Jeurissen, B., Malcolm, J., Ramirez-Manzanares, A., Reisert, M., Sakaie, K. & Tensaouti, F. Quantitative evaluation of 10 tractography algorithms on a realistic diffusion MR phantom. *Neuroimage* **56**, 220–234 (2011).